5-2014

An analytical and experimental biosensor for human MIG using AlGaN/GaN based HEMT devices

Hector Trevino II
University of Texas-Pan American

AN ANALYTICAL AND EXPERIMENTAL BIOSENSOR

FOR HUMAN MIG USING ALGAN/GAN BASED

HEMT DEVICES

A Thesis

by

HECTOR TREVINO II

Submitted to the Graduate School of
The University of Texas-Pan American
In partial fulfillment of the requirements for the degree of

MASTER OF SCIENCE

May 2014

Major Subject: Electrical Engineering

AN ANALYTICAL AND EXPERIMENTAL BIOSENSOR

FOR HUMAN MIG USING ALGAN/GAN BASED

HEMT DEVICES

A Thesis
by
Hector Trevino II

COMMITTEE MEMBERS

Dr. Hasina Huq
Chair of Committee

Dr. Heinrich Foltz
Committee Member

Dr. Karen Lozano
Committee Member

Dr. Yuanbing Mao
Committee Member

May 2014

ABSTRACT

Trevino II, Hector, <u>An Analytical and Experimental Biosensor for Human MIG Using AlGaN/GaN Based HEMT Devices.</u> Master of Science (MS), May, 2014, 150pp., 14 tables, 64 figures, 126 references, 60 titles.

An amperometric biosensor using AlGaN/GaN based HEMT devices is constructed experimentally and validated through analytical and numerical techniques for detection of a key protein in allograft rejection (Human MIG/CXCL9). The prototype developed provides a reliable sensing platform that will allow label-free and marker-free detection. By exploiting characteristics unique to AlGaN/GaN based HEMT devices, a floating gate configuration is employed to allow reliable sensing without the need for any reference electrode. Self-assembled monolayers (SAM) are formed at the gate surface by using a crosslinker (DSP) to allow for appropriate immobilization of target antibodies. A theoretical analytical and numerical model is developed to explain the mechanism of action of the proposed biosensor. Furthermore, other issues such as repeatability, influence of the substrate, threshold shifting, and device packaging are addressed. Finally, an experimental circuit is constructed with the previously prepared biosensor to validate the claims made in this thesis.

DEDICATION

The completion of my graduate studies, along with the topic of this thesis is dedicated to

my mother, my father, and my sister whose love and support were very impactful on my goals.

ACKNOWLEDGEMENTS

TABLE OF CONTENTS

LIST OF FIGURES

CHAPTER I

INTRODUCTION

For the past 30 years, silicon based MOSFETs have been widely used and trusted choices for power devices. However, as technology continues to advance and materials become more understood, silicon based FET technologies are approaching a performance plateau [1]. Furthermore, with the advancement of technology comes the need for devices to meet new requirements and challenges. Thus, plenty of time and research has been put into the development of new FET technologies based on wide bandgap semiconductors such as silicon-carbide (SiC) and gallium nitride (GaN) whose functions overcome the physical limitations of silicon alone [1]. As the future approaches, federal funding, and independent research has grown increasingly confident in the necessity for development of wide band gap technologies.

A wide band gap semiconductor is a semiconductor that has a band gap significantly greater than silicon. While the exact definition of where a regular band gap material ends and wide band gap material begins varies among context, it is generally accepted that a wide band gap semiconductor's band gap will be much higher than that of silicon or gallium arsenide (traditional semiconductors). A wide band gap gives the semiconductor properties that allow higher performance while consuming less power than traditional silicon based devices while operating at a much smaller scale [2]. Also, they can operate in much harsher environments compared to silicon [2]. Some examples of wideband gap semiconductors are silicon carbide,

boron nitride, gallium nitride, aluminum nitride, zinc oxide, and diamond. For field effect transistors based on wide band gap materials, the III-V nitride groups are the main groups of interest with much emphasis placed on GaN [1]. This is due to many of the intrinsic properties of the material, along with the behavior of such materials when constructed in a heterostructure. As these materials and their interactions become better understood, newer and more innovative uses for such devices have become more investigated. One such discovery is in the field of GaN based chemical sensors.

1.1 The transition to wide band gap semiconductor based technologies

GaN and other alloys of the nitride type (aluminum nitride [AlN], indium nitride [InN]) have recently become prime research interests for device engineers and physicists. Unlike other III-V alloys, GaN, AlN, and InN are hard, partially ionic compounds that exhibit thermal and chemical stability. They exhibit ionic potential that resembles II-VI compounds, and hardness and chemical inertness that is similar to that of diamond or Boron Nitride (BN) [3]. Of the III-V nitrides, GaN has been extremely attractive and considered to be the next modern semiconductor to replace silicon [1]. The unique properties of GaN allow the material (through its direct band gap properties) to emit bright light as an LED, or function as high power / high current RF devices.

Despite knowledge of GaN's superior qualities and the fact that it was first synthesized in the early 1930s, it wasn't popularized until around 1989 due to difficulties in single-crystalline crystal growth. The melting temperature for GaN is very high (2500°C) and is coupled with high equilibrium nitrogen pressure of about 45,000 bar [3]. A table showing some properties of GaN compared to other semiconductor materials can be seen in Table 1.1.

2

Table 1.1 – Properties of several wide band gap semiconductors relevant to silicon [3] [4]

Property	Silicon	GaAs	4H-SiC	GaN	Diamond
Bandgap, Eg (eV)	1.1	1.43	3.3	3.4	5.45
Gap Type	indirect	direct	indirect	direct	indirect
Intrinsic carrier concentration n_i cm^{-3}	1.5×10^{10}	1.5×10^{6}	8.2×10^{-9}	1.9×10^{-10}	1.6×10^{-27}
Dielectric constant, e_r	11.9	13.1	10.1	9.5	5.5
Breakdown field, E_c (kV/cm)	300	455	2200	2000	10000
Electron mobility, μ_n (cm^2/V -s)	1500	8500	1000	1250	2200-4500
Hole mobility, μ_p (cm^2/V -s)	600	400	115	250	1600-3000
Vsat (10^7 cm/s)	1.0	1.0	2.0	2.7	2.7
Thermal Conductivity, l (W/cm-K)	1.5	0.46	4.9	1.3	22
Maximum Operating Temperature	300	300	600	700	1000
Melting temperature, $°C$	1400	1250	----	2500	1600
Pressure in which melting temperature can be realized , $p^m (atm)$	<1	15	----	45,000	60,000

Diamond as seen above, is considered the ultimate semiconductor. However, with a Mohs scale

rating of 10, diamond is the hardest known bulk material substance on earth. This, along with a

very high demand for diamond makes manufacturing of such a device very difficult and

expensive. It is for this reason that research seeks a more cost-effective alternative, and this is

where GaN based technologies have been greatly pursued.

Currently, the obstacle of using GaN as a bulk substrate is still under development and

currently existing technologies typically use SiC, Sapphire, or diamond substrates to grow GaN

crystal layers. While these substrates are viable solutions, they are still relatively expensive and

have limited bulk manufacturing potential due to the small size of the wafers (6 inches for

sapphire, and 4 inches for silicon carbide) [1]. Furthermore, SiC, while having small lattice

mismatch and great thermal conductivity is almost 100 times more expensive than silicon alone. Sapphire is faced with poor thermal conductivity which is not ideal for the market of power devices. It is for these reasons that researchers have started attempting to achieve GaN-on-silicon solutions. However, there are significant mismatches in lattice constant, and thermal expansion coefficients between GaN and silicon that make this alternative very difficult for researchers [1].

1.2 Gallium Nitride

Gallium nitride (GaN) is a III-V Wide-Bandgap binary semiconductor that naturally has wide band gap at room temperature [5]. Typically, GaN is found in a Wurtzite Crystal Structure at room temperature, but it may also have a zinc blende crystal structure for thin films. Zinc blende structures are also known as face-centered cubic (fcc) structures and are characterized by cubic closet packing (ccp). Crystals of the zinc blende are meta-stable and are grown heteroepitaxially on certain substrates such as Si, GaAs, or MgO (Figure 1.1). Wurtzite crystal structures are characterized by a hexagonal closet packing structure (hcp). Most applications of GaN in practice usually employ crystals of the Wurtzite blend (Figure 1.2). It is mechanically stable with high heat capacity and thermal conductivity. This makes them excellent candidates for high temperature and high power microelectronic devices. Furthermore, GaN bonds are significantly stronger than Ga-Ga interactions, and form tetrahedral bonds [6]. Some basic properties of GaN can be seen in Table 1.2.
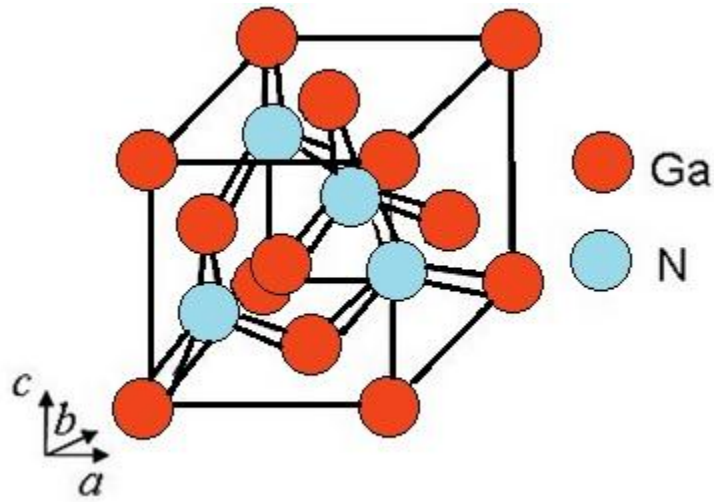
Figure 1.1 – Zinc blende structure of GaN [6]
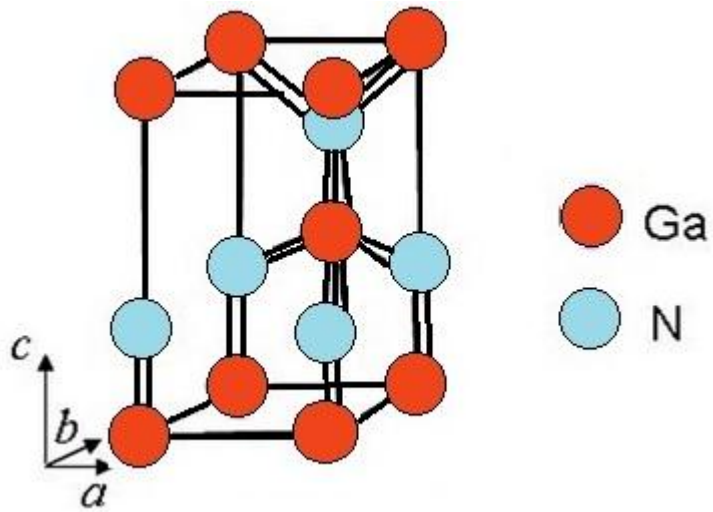
Figure 1.2 –Wurtzite crystal structure of GaN [6]

5

Table 1.2 – Some basic properties for the Wurtzite crystal structure of GaN [7]

Property	GaN
Dielectric constant e_r at 300K (static)	9.5
Electron affinity at 300K (eV)	4.1
Lattice Constant a (Å)	3.186
Lattice Constant c (Å)	5.186
Coordination Geometry	Tetrahedral
Electron mobility, μ_n (cm^2/V-s)	1250
Hole mobility, μ_p (cm^2/V-s)	250
Refractive index, n_D	2.429
Thermal conductivity, l (W/cm-K)	1.5
Saturation velocity, cm/s	$2.5 * 10^7$
Effective mass, m_e^*	$0.2*m_0$
Optical Phonon Energy,meV	91.8
Mass density (kg/m^3)	6150
Piezoelectric constant $e_{14}, (C/m^2)$	0.375
Optical phonon energy (eV)	0.0912

1.3 Competitive advantage of GaN based electronics

GaN has been used commonly in bright LEDs since the 1990s. It is arguably the most important semiconductor after silicon, and with a bandgap of 3.4 eV it carries a lot of interest in optoelectronic and high-power / high-frequency devices. Some competitive advantages of GaN and their realizations can be seen in Table 1.3.

Table 1.3 – Competitive advantages of GaN in electronic devices [8].

Customer Need	GaN Enabling Feature	Advantage
High Power / High Temp Operation	Wide Band Gap	Compact
High Voltage Operation	High Breakdown Field	Reduce Step Down
Low Noise	High Gain, High Velocity	Dynamic Range Receivers
Thermal Management	GaN on SiC Substrate	High Power / Less cooling
High Linearity	HEMT	Band Allocation optimization
High Frequency	High Electron Velocity	Bandwidth, millimeter wave

With an electron mass of $.20m_0$, a quantity three times larger than AlGaAs, an electron mobility is seen that is actually smaller than AlGaAs at room temperature. However, it is seen at

high electric fields that the performance of GaN in heterostructure devices is governed by electron velocity rather than mobility [9]. Furthermore, GaN along with the other nitrides (AlN, InN) exhibit spontaneous and piezoelectric polarizations when applied in heterostructures due to lack of reverse symmetry along the c-axis [9]. Also, GaN has a large Johnson figure of merit compared to silicon (215.1), and the large breakdown field of GaN implies that large electric fields can be passed through the device without damage or compromise to the material.

1.4 The High Electron Mobility Transistor

The High-electron-mobility-transistor (HEMT) is a field-effect transistor also known as a MODFET (Modulation-doped field effect transistor), TEGFET (Two-dimensional electron gas field effect transistor), or HFET (Hetero-junction field effect transistor) [10]. They have become increasingly popular in military and aerospace applications where low noise figures, and high gains are particularly sought after. The HEMT was successfully invented and demonstrated in 1980 by Dr. Takashi Mimura of Fujitsu Laboratories [11]. The idea behind the High-electron-mobility-transistor stems from basic semiconductor physics in which certain layers need to be doped with n-type impurities to introduce additional free electrons in that particular layer. This procedure, however, actually results in slowing down of electrons due to collisions with the other impurities that were originally introduced into that layer [11]. The HEMT was designed to resolve this issue by using an n-type, highly doped AlGaAs layer built over an undoped GaAs layer. Due to higher affinity of the GaAs, the electrons from the doped AlGaAs drop into the next layer of GaAs to form a depleted AlGaAs layer due to the presence of a steep canyon

formed in the GaAs layer where the electrons have the freedom to move quickly without any external collisions with impurities [11].

While the first HEMT devices were GaAs based devices, there has been recent interest in AlGaN/GaN based HEMT devices due to the higher bandgap of GaN, increased power density(more power per square millimeter in die), and potential to handle extreme thermal conditions. GaN based HEMTs can also operate at higher voltages, frequencies and at higher efficiency [12][13]. This makes GaN based HEMTs extremely attractive for military and mobile communication systems. Detailed discussion of epitaxial layers, varieties, and overview of device operation is discussed in Chapter 2.

1.5 GaN based HEMT biosensors

Over the past several years, there has been much research into developing newer and less invasive ways to monitor and detect several different biological cells and molecules [14-19]. Such biological elements include but are not limited to: proteins, enzymes, antibodies, and tissue cells. The need for such development arises from the current way in which patient data is obtained [20-21]. Invasive methods such as biopsies and invasive monitoring require making incisions and taking samples or inserting devices into the organ/tissue in need of monitoring. With advances in medicine and technology, a growth in understanding in key biomolecules that play certain roles and functions in the development of disease are becoming more useful in the developing of devices to help detect such molecules [14-19].

As investigations into wide band gap based electronics have been developed and understood, AlGaN/GaN based wide band gap devices have become very attractive in the world of biological modified field effect transistors (BioFETS / biosensing) due to their thermal stability, high-sensitivity, and label-free / real time detection. They also exhibit a chemical

inertness to extreme sensing environments [14-19]. Also, the unique ability for GaN material to exhibit spontaneous and piezoelectric polarization in heterojunctions without any need for material doping results in the formation of a conducting channel consisting of a two dimensional electron gas (2DEG) that exhibits very high mobility ($\sim 1200 - 1500$ cm^2/V-S) in two dimensions with very tight confinement in the third [22-23]. Furthermore, the close proximity of this layer to the surface (< 35 nm) is extremely sensitive to ambient changes in surface charge and results in greater detection sensitivity [15][17][24]. One particularly useful application for GaN based HEMT biosensor technologies exist in early monitoring of allograft rejection. Taking advantage of the depletion mode HEMT (normally on), and by using a floating gate (gateless) configuration, the need for an external bias voltage can be neglected and amperometric detection can be realized solely by varying surface charges induced by the biomolecule through capacitive coupling [14][17]. It has been previously reported that HEMT devices have the potential to exhibit strong amperometric results in detection of certain key biomolecules [14-19][24]. Detection of pH levels, DNA, certain types of bacteria, and gas have all been reported. Preparation for using such devices can be rigorous, and due to the fragile nature and small scale of the HEMT plus the minute quantities of analytic solutions, careful preparation must be exercised to create a customized biosensor that is chemically inert and thermally stable. A more detailed overview of the theory behind GaN HEMT based biosensors is explored in greater detail in Chapter 2.

1.6 Research objectives and outline

The purpose of this study is to provide work for three main objectives: The proposition of a biosensor based on previous research and understandings, the theoretical development of an analytical and numerical model with aide of SILVACO™ two-dimensional modeling software,

and the experimental findings and phenomenon conducted to test the former. Many papers have been published by many prestigious universities and research centers that exhibit the potential usage for GaN based biosensors for detection of various analytes. However, detailed description of quantum mechanical function of these proposed biosensors has been theorized, but not provided. One goal of this study is to provide two-dimensional simulation to support these claims.

This aim of this chapter was to provide some insight into the up-and-coming popularity of wide band gap materials and their applications. It introduced the history and applications of gallium nitride and their contribution to the high electron mobility transistor. The chapter concludes with a brief introduction into GaN based HEMT biosensors and their mark on the modern world.

Chapter 2 discusses, in detail, the theory behind the quantum mechanical operations of the High Electron Mobility Transistor, as well as an introduction to the target analyte (MIG), its nascency, and the significance of this protein to the human immune system.

Chapter 3 elaborates on the methodology for realization of a GaN HEMT based biosensor, while focusing on several important aspects of the procedure such as crosslinking and development of a self-assembled monolayer.

Chapter 4 provides some background on fundamental phenomenon as a prerequisite to the analytical modelling that will be developed in the later part of this chapter. It gives background in some phenomena such as the theory of surface states, and the double-layer interface. This chapter is crucial to the understanding of the mechanism of action of the proposed biosensor.

Chapter 5 provides numerical modelling for the proposed biosensor using the Charge-control model for sheet carrier concentration at the heterojunction, chemistry techniques, Albrecht's low field mobility equations, and the net neutrality model. It builds on the phenomena discussed in chapter 4, and SILVACO™ simulations are conducted to ease calculation and serve as a visual aid to help understand the quantum mechanical characteristics of the device structure. This model aims to simulate the results seen experimentally which will be discussed in detail in Chapter 6.

Chapter 5 provides experimental results, and validation of these results with literature, theory, and previously developed theory in preceding chapters.

CHAPTER II

LITERATURE REVIEW

As the theory behind realization of a GaN based HEMT Biosensor is developed, first an understanding of the quantum mechanical function of the device must be developed, for it is these effects that are widely accepted to be responsible for sensor based realizations. It is also required to discern the significance of Human MIG and its impact on the human body.

This chapter presents the theory of operation of gallium nitride based high electron mobility transistors, and is explored to cover the history of the GaN based HEMT device and its general operations. Then, an introduction to human MIG, and why this is the analyte of choice for the proposed biosensor.

2.1 HEMT Ideology

The high-electron-mobility-transistor operates as a field-effect transistor with basic operating principles having close similarities with the MESFET (Metal-semiconductor field effect transistor). However, the epitaxial layer (Figure 2.1) is significantly different than the MESFET. The first HEMT devices typically employed gallium arsenide and indium arsenide (InAs). For basic HEMT devices with hetero-junctions consisting of $Al_xGa_{1-x}As$ and GaAs, where the mole fraction of Al_xAs is typically $0.2 < x < 0.3$ [12]. The different layers each possess a different band gap but are grown with the same lattice constants. HEMTs that are

grown with different lattice constants for the two hetero-layers are called pseudomorphic

HEMTs (pHEMTs) [13]. The most important feature in HEMT devices is the presence of a two-

dimensional electron gas (2DEG) formed by the combination of the two different bandgaps of

$Al_xGa_{1-x}As$ and GaAs. With sufficient doping, the electrons of the higher band gap material

($Al_xGa_{1-x}As$) are allowed to diffuse to the lower band gap material (GaAs). The potential barrier

at the interface confines electrons to a thin sheet referred to as 2DEG resulting in very high

mobility in two dimensions with tight confinement in the third [12]. The electrons trapped in this

region are restricted to motion in the x and z directions. The y direction is tightly confined due to

the energy barriers on either side of the potential well. These barriers have a shorter distance than

the Broglie wavelength (260 Å) and have quantized momentums that cannot exist in a direction

perpendicular to the interface [13]. More detailed explanations leading up to the formation of

2DEG are seen later in this chapter.
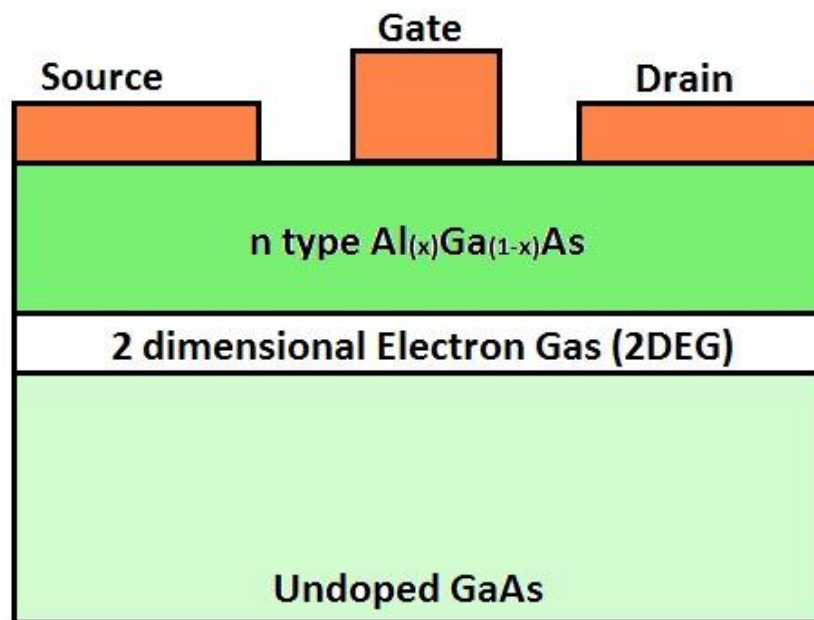
Figure 2.1 – Basic Structure of AlGaAs/GaAs HEMT (not to scale).

2.2 Gallium Nitride based HEMT devices

Nowadays, gallium nitride based technologies have demonstrated the capability to address current technological demands in today's electronics markets. In the last decade we have begun to see GaN based HEMT devices replacing the traditional GaAs based devices. High thermal conductivity, high breakdown electric field, high peak velocity, high sheet charge density, and high saturation velocity are all superior features of GaN based HEMTs that make these devices very attractive in different fields of engineering [22]. The use of GaN-based HEMTs hold many advantages over their GaAs counterparts. For one, fabrication is possible at a fraction of the size of a GaAs counterpart due to the high output power density. This ultimately allows the same output power capability as a GaAs device, but on a much smaller scale [24]. Smaller size also contributes to higher impedance, which facilitates loss matching when used as an amplifier. Also, GaN based HEMT devices exhibit strong spontaneous and piezoelectric polarizations that allow for a 2DEG to be formed with intrinsic materials (unlike GaAs based devices that require modulation doping) [22][24].

2.3 Gallium Nitride HEMT device ideology

While functionality of field-effect transistors (FETs) usually are similar between devices regardless of internal materials, gallium nitride based FETS and their epitaxial layers are unique (Figure 2.2). Field effect transistors made from the AlGaN/GaN hetero-structure configuration conquer the trade-offs between high current/high frequency operations for metal oxide semiconductor field-effect transistors (MOSFETs) and metal oxide semiconductor field-effect transistors (MESFETs) [24][5]. Selective doping, also called modulation doping, is utilized to control certain behaviors and characteristics of the HEMT, such as sheet charge density. However, this is not necessary and the absence of impurities (dopants) in the channel region

eliminates ionized impurity scattering, ultimately leading to an increase in electron mobility without the need for modulation doping [5]. Furthermore, even at high temperatures, electron velocity and electron mobility remain high, and the breakdown field rests at about 3 orders of magnitude higher than that of silicon or gallium arsenide. This can be directly attributed to the wide band gap structure of GaN [5]. Tables 2.1 and 2.2 shown exhibit some important properties of the AlGaN/GaN HEMT device and some fabrication considerations needed to ensure the device exhibits its full potential.

Table 2.1 – Some important properties of AlGaN / GaN Heterojunction HEMTs [5]

Material	Breakdown Field	Band Gap	Saturation velocity	Sheet Carrier Density	Mobility in heterostructure of AlGaN/GaN	Heat Conductivity
GaN HEMT	~3.0MV/cm	3.4eV	$2.5 * 10^7$ cm/s	$\sim10^3 cm^{-2}$	$1500 - 2000$ cm^2/(Vs)	~1.5 W/cm/K

Table 2.2 – Modes of action for characteristic quantities in AlGaN/GaN HEMT devices [25]

Desired quantity	Mode of Action
High Sheet Charge density	Maximization of spontaneous and piezoelectric polarizations. Dependent on modulation doping or polarization doping.
Breakdown Voltage	High quality materials / proper design
Electron velocity	Reduced effective gate length
Electron Mobility	Minimizing ionized scattering due to roughness of interface, and disordering of the alloy between the two materials.
Thermal Conductivity	Thick GaN on sapphire or SiC
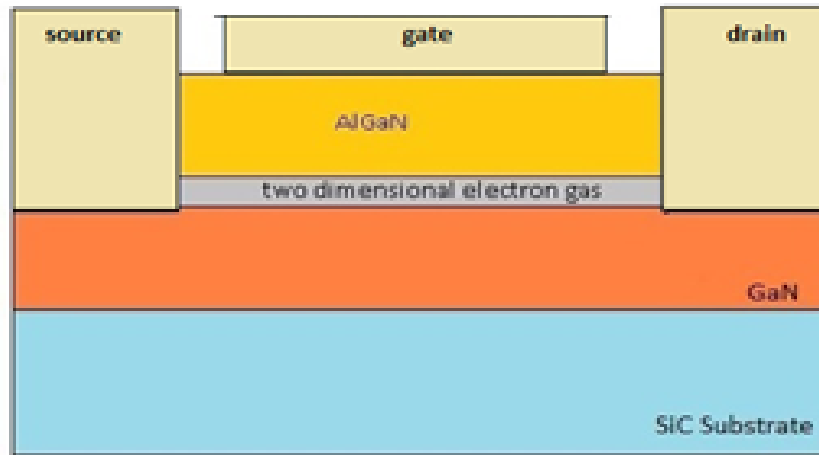
Figure 2.2 – Typical Structure of AlGaN/GaN HEMT (not to scale)

Sometimes, an aluminum nitride (AlN) spacer layer is introduced between the heterostructure to increase the 2DEG density, mobility, and conductivity (Figure 2.3). The insertion of the thin AlN spacer layer increases conductivity because of the high piezoelectric field in the AlN layer generates a dipole. The production of this dipole increases the effective band offset in the conduction band and helps increase the quantum well depth [25] [26]. Thickness of AlN layer is a very important parameter in enhancing 2DEG properties, and careful engineering of this layer must be exercised, as AlN is highly insulating. Also, as the aluminum content of the barrier is increased then mobility of electrons decreases due to scattering of the AlN alloy [27]. The bandgap energy in AlGaN depends on the mole fraction of Al in the alloy. At room temperature this value ranges from 3.5 to 6.2eV [9]. Also, a cap layer consisting of doped GaN may be introduced and has been experimentally shown to increase current and breakdown voltage in HEMTS while reducing leakage.
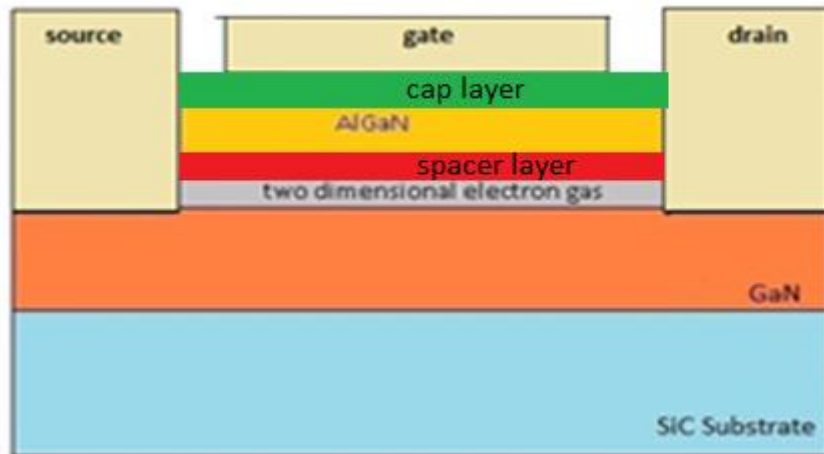
Figure 2.3 – AlGaN/GaN HEMT Structure with added layers

2.4 The basics of band theory

In solid-state physics, every solid material possesses its own unique energy-band structure. The structure of the bands and the variation in band structure play a key role in the electrical characteristics of the materials [5]. These band diagrams can be used to explain the behavior of delocalized electrons, and the energy required to get them excited [28]. As the phenomenon of the band gap became more widely understood it allowed scientists to understand the true usefulness of semiconductor materials.

Generally, a "band" is the result of a large number of atoms forming a smeared continuous distribution of energy [29]. When a single atom bonds with another atom of the same type two possible molecular orbitals result. One with a higher energy relative to the sum of individual electron orbital energies, and one with a lower energy relative to the sum of individual electron orbital energies [30]. If we take N amount of atoms consisting of N valence electron orbitals of the same energy and they all bond to one another, then N energy levels result.

Naturally, half of these energy levels will be higher in energy, and half will be lower in energy relative to the sum of N valence electron orbital energies [30]. Realistically, however, the energies will not all be exactly at the same level higher and lower with respect to the sum of valence orbital energies. The energy levels between them on either end have very small variation and the combination of all these varied energy levels become blurred to define an energy band [30]. Between energy levels exists a forbidden level of electron energies formally referred to as the band gap (Eg) [29]. The highest range of energies that an electron occupies at absolute zero temperature is referred to as the valence band, and is typically represented as the bottom band in a band diagram (Ev). The next available energy states are in a higher band called the conduction band and is normally represented as the top band in a band diagram (Ec).

In order for current to exist, some electrons must gain energy, or move to a higher electron energy levels [29]. This may happen if an electron absorbs an energy at least as great as the band gap energy [30]. In insulators, the valence band is completely filled and the conduction band is unoccupied. The band gap between the two is extremely large, requiring substantial amounts of energy to make the transition from the valence band to the conduction band. For metals, the highest occupied level exists somewhere in the middle of the energy band, so when a potential is applied current can flow because there are plenty of unoccupied energy levels in which an electron may be free to roam to. The valence band can either be partially filled, or it may overlap with the conduction band. In semiconductors, a small but appreciable band gap exists at room temperature. Conduction bands may be empty or partially filled and are also referred to as weak conductors. Various definitions exist that distinguish the difference between a semiconductor and an insulator. Normally, materials with band gaps less than 3 eV are regarded as semiconductors, while materials with band gaps greater than 3 eV are regarded as

insulators. However, in some contexts, some materials (such as GaN, and AlN) with band gaps

that lie around the 3-6 eV range are regarded as wide band gap semiconductors (WBG) [30].

Table 2.3 depicts various band gap energies of different materials.

Table 2.3 - Table of Various semiconductor materials and their band gaps

Group	Material	Band Gap	Gap Type
IV	Silicon	1.1 eV	Indirect
IV	Silicon Carbide (4H)	3.3 eV	Indirect
III-V	Aluminum Nitride	6.28 eV	Direct
IV	Germanium	0.67 eV	Indirect
III-V	Gallium Nitride	3.4 eV	Direct
III-V	Gallium Arsenide	1.43 eV	Direct
III-V	Indium Phosphide	1.35	Direct
III-V	Indium Arsenide	0.36	Direct
II-VI	Zinc Oxide	3.37	Direct
IV	Diamond	5.47	indirect

Essentially, the electrical conductivity of a solid depends on the energy band spacing and

the extent at which the bands are occupied [29]. A general band gap diagrams for metals,

semiconductors, and insulators can be seen in figure 2.4. Figure 2.5 shows a slightly more

detailed general band structure of a semiconductor. As mentioned previously, the conduction

band may be partially filled or empty. In the figures, the band gap is representative of the energy

difference between the bottom of the conduction band and the top of the valence band.
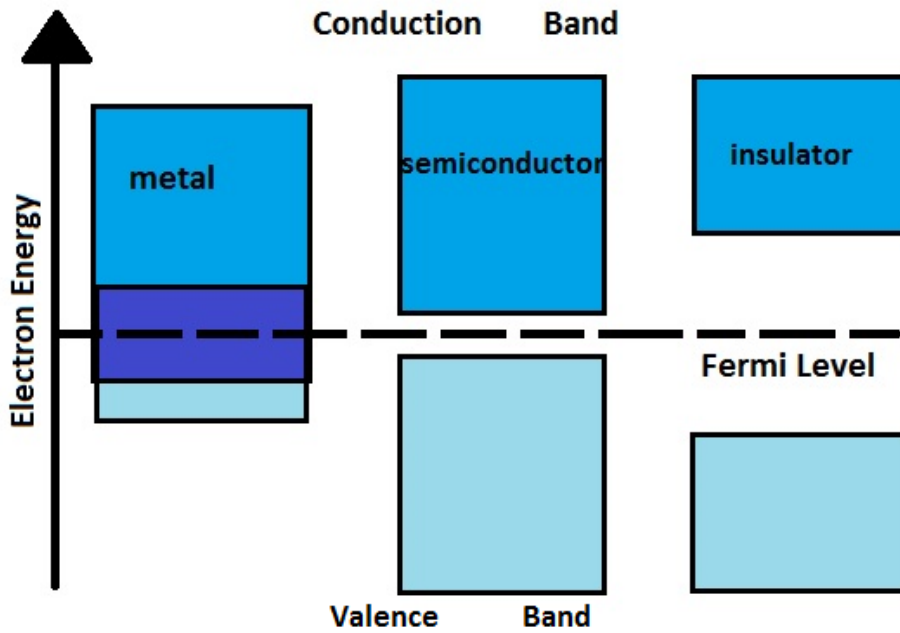
Figure 2.4 – Band gap distinctions between metals, semiconductors, and insulators [28-30]
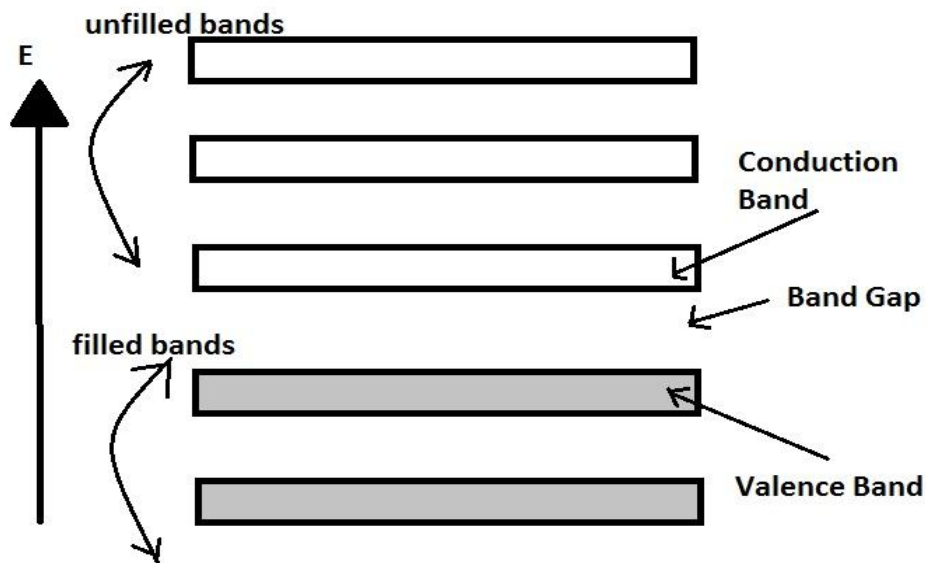
Figure 2.5 – General Structure of Band Gap in Semiconductor Material [28-30]

2.5 AlGaN/GaN HEMT development of the band diagram

Generally, the band diagram for a GaN HEMT can be thought of a wide band gap (WBG) material (AlGaN) interfacing with a narrow band gap (NBG) material (GaN) (Figure 2.6). However, to fully understand the band diagram and how the quantum well at the interface exists and its contribution to the development of its characteristic two dimensional electron gas (2DEG), further mathematical understanding of the piezoelectric and spontaneous polarization effects of AlGaN/GaN heterostructures is required. Further detail on these effects is discussed in section 2.5.1.
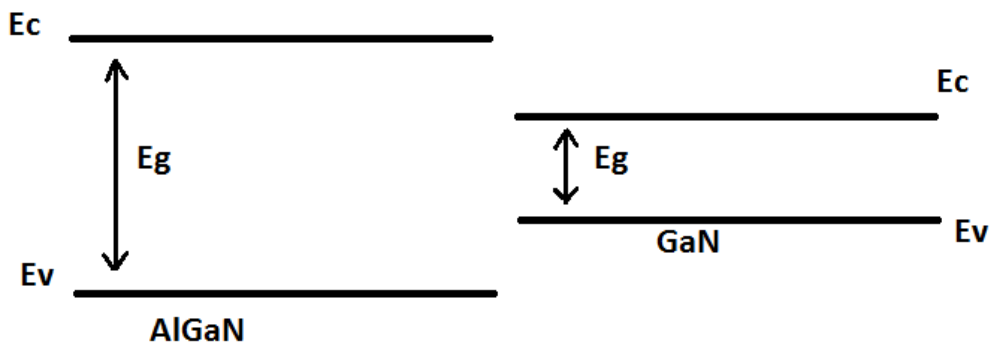
Figure 2.6 - Band structure of general AlGaN/GaN HEMT before equilibrium
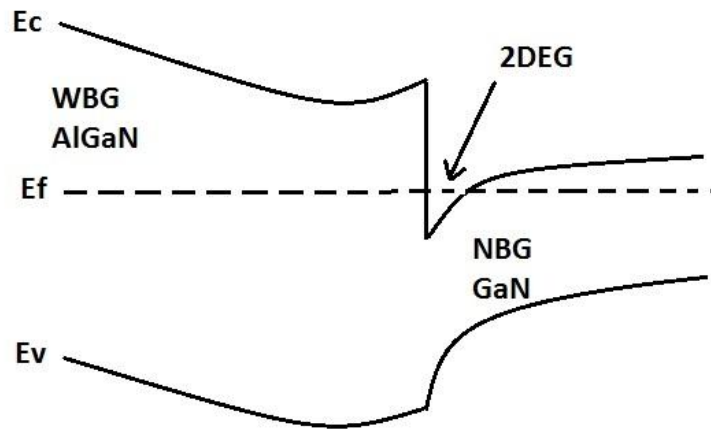
Figure 2.7 – Band structure of general AlGaN/GaN HEMT after equilibrium

The discontinuities in the conduction band are due to the different electron affinities of the two materials at each side of the hetero-junction. The bending of the bands occurs due to charge transfers from the supply layer (AlGaN) to the narrow bandgap material (GaN) [9]. After equilibrium, the large band discontinuities close and form a quantum well in the process.

2.5.1 Spontaneous and piezoelectric effects of AlGaN/GaN HEMTs

Nitrides of Group III such as aluminum nitride (AlN), and gallium nitride (GaN) exhibit strong polarization effects when structured in a heterojunction [10]. AlGaN and GaN are such materials and are comprised of polarized Wurtzite cystal structures. They both possess strong polarization in the (0001) (c-axis) direction [3]. Intrinsic asymmetry directly attributes to spontaneous polarization (P_{sp}) in equilibrium in the absence of external fields, and refers to the polarization field existing in an unstrained crystal. It is a negatively expressed value, and is expressed in increasing quantities in GaN, InN, and AlN respectively. Furthermore, tensile strain (due to lattice mismatching) caused by growth of AlGaN on GaN results in piezoelectric polarization (P_{pz}) [10] [8]. It is a negative quantity for tensile strain and a positive one for compressive strained AlGaN layers. Both P_{sp} and P_{pz} polarizations are expressed in the same direction (0001), thus the total polarization at the heterojunction interface for $Al_xGa_{1-x}N$ on GaN is given by [10] [8]:

$$P_x = P_{sp} + P_{pz} = -[(3.2x - 1.9x^2) \times 10^{-6} - 5.2 \times 10^{-6}x]C\ cm^{-2} \qquad (2.1)$$

where x is the mole fraction in the $Al_xGa_{1-x}N$ composition. The dipole can possess a maximum moment that can be represented by:

$$\Delta E_v + E_{g,GaN} \qquad (2.2)$$

The charge distribution consists of polarization dipole $\pm Q_\pi$ and an opposing dipole consisting of a surface hole gas, p_s, and a 2DEG at the heterojunction interface, n_s [8]. Net polarization charge can be seen being developed in figure 2.8 and figure 2.9.
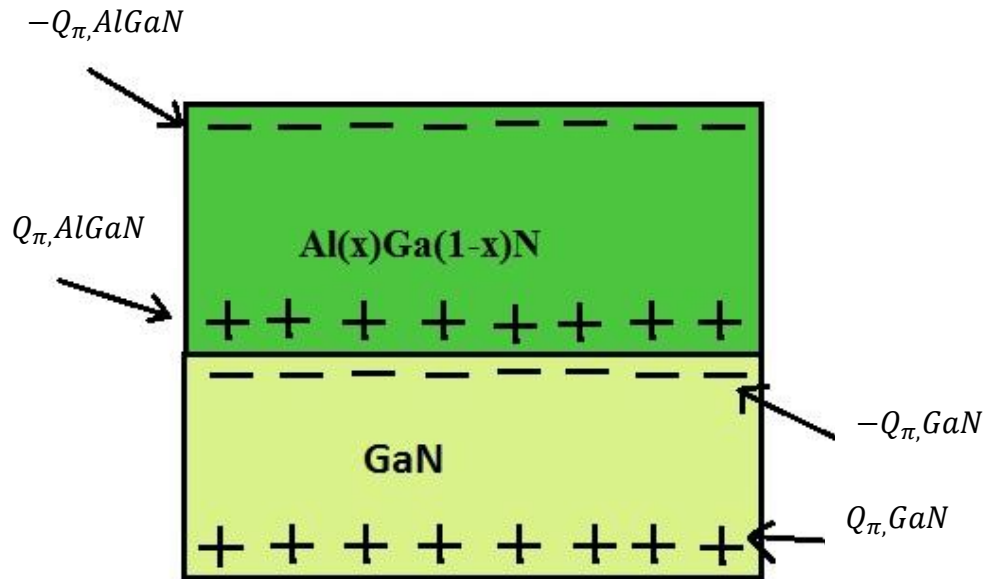
Figure 2.8 – Spontaneous and piezoelectric polarizations at the interface [8][32-33].
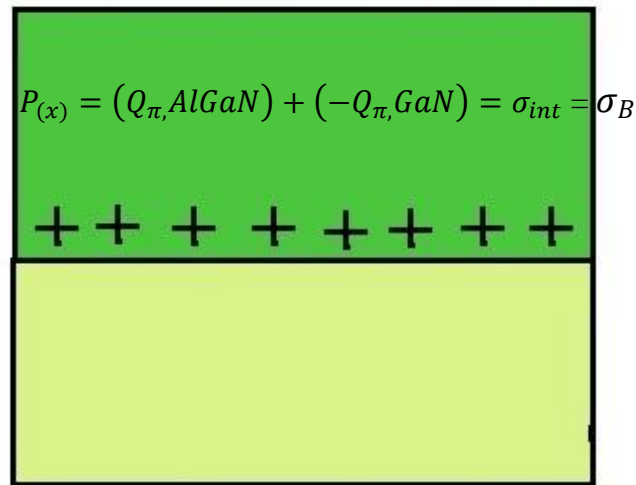
Figure 2.9 – Net polarization charge at the AlGaN/GaN interface [8][32-33].

In the band diagram, the charge dipole present across the AlGaN layer causes band bending with a constant slope. As can be seen from figure 2.8, a positive net charge exists at the heterojunction interface, while a negative net charge is seen at the surface. A triangular shaped quantum well is formed on the left side through the conduction band discontinuity, and the bending of the conduction band in the GaN layer (where the 2DEG exists with a finite spread in space) follows Poisson's equation [31][33]:

$$\frac{d^2\psi(x)}{dx^2} = -\frac{\rho(x)}{\epsilon_S} \tag{2.3}$$

where $\psi(x)$ is the potential distribution in the semiconductor, q is the charge of an electron, ϵ_s is the semiconductor permittivity, and the space charge density $\rho(x)$ can be represented as:

$$\rho(x) = q(N_D - N_A + p(x) - n(x)) \tag{2.4}$$

where the spatial variation of hole and electron concentrations can be expressed as:

$$p(x) = N_A \exp\left(\frac{-q\psi(x)}{kT}\right) \tag{2.5}$$

$$n(x) = \frac{n_i^2}{N_A} \exp\left(\frac{-q\psi(x)}{kT}\right) \tag{2.6}$$

where N_A is shallow accepter density, n_i is the intrinsic carrier concentration, k is Boltzmann's constant, and T is the temperature in Kelvin (K) [31]. A depiction of band bending with and without spontaneous and piezoelectric polarizations taken into account can be seen in figure 2.10 derived by K.F. Brown et. Al (2002), and a figure demonstrating the charge contributions of former polarizations relative to surrounding polarizations can be seen in figure 2.11.
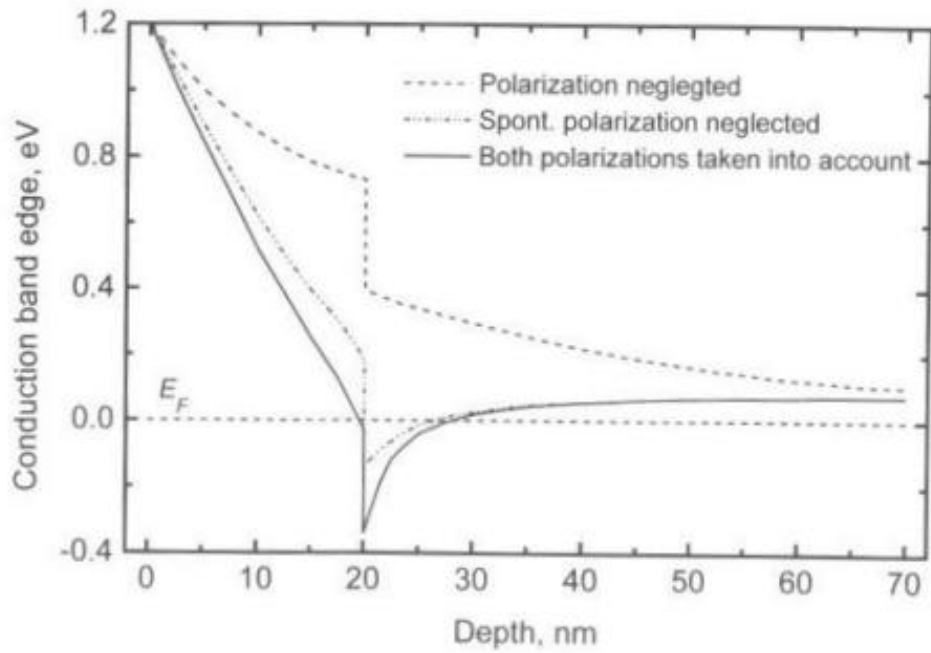
Figure 2.10 – Conduction band edges in the heterostructure with certain polarizations (source: K.F. Brown et. al Theory of Modern Electronic Semiconductor Devices 2002) [32].
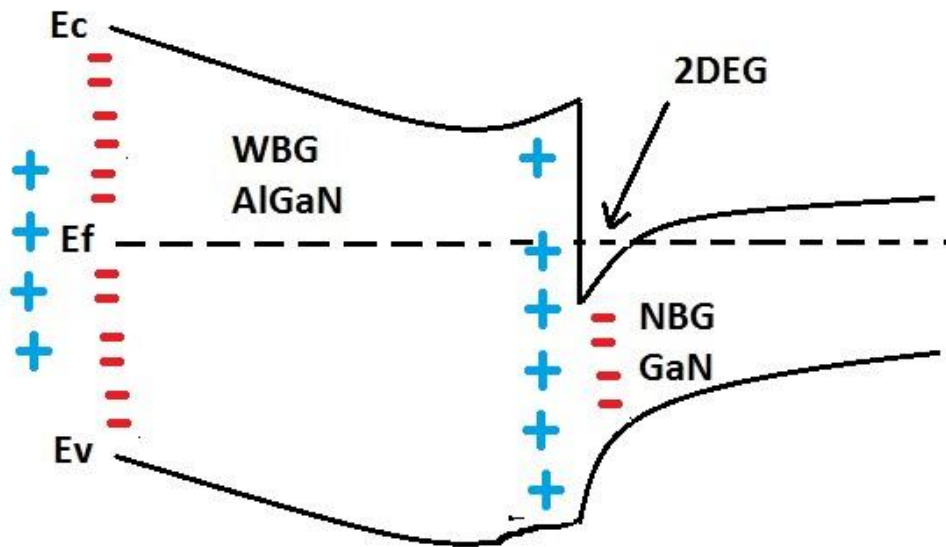
Figure 2.11 – AlGaN/GaN HEMT band diagram with polarization charge distribution.

2.6 Two-dimensional Electron Gas

As its AlGaAs/GaAs counterpart, a two-dimensional electron gas (2DEG) is what gives the HEMT its most significant characteristic. However, unlike the AlGaAs/GaAs version of the device which is provided by a donor sheet in the AlGaAs layer, the 2DEG in the AlGaN/GaN variation is formed by the strong pyroelectric and piezoelectric nature of the wurtzite structure of GaN [5]. The difference in band gaps between the AlGaN (Average Eg = 4.24eV) and GaN (Eg = 3.4eV) layers creates a deep quantum well in the heterojunction interface in which electrons are highly mobile in two-dimensions (with extreme confinement in the third) [22]. The sheet carrier density of this 2DEG is well above the order of magnitude 10^{13}cm^{-2}. This can attribute to the high-current carrying capabilities of the HEMT [5]. Now that the effects of spontaneous and piezoelectric polarizations have been developed, along with the development of the band diagram, we can now focus on the development of the 2DEG.

The two dimensional electron gas is something that is constantly being studied and updated mathematically. As of now, it is known to be a function of surface barrier, thickness of the AlGaN layer, and the net positive charges at the interface [33]. Unlike its AlGaAs/GaAs counterpart, the AlGaN/GaN variation of the device requires no doping to exhibit 2DEG presence at the interface [33]. Figure 2.12 defines the variables present in development of the 2DEG equation relative to the band diagram of the device, while Table 2.4 provides the formal definition for these parameters.
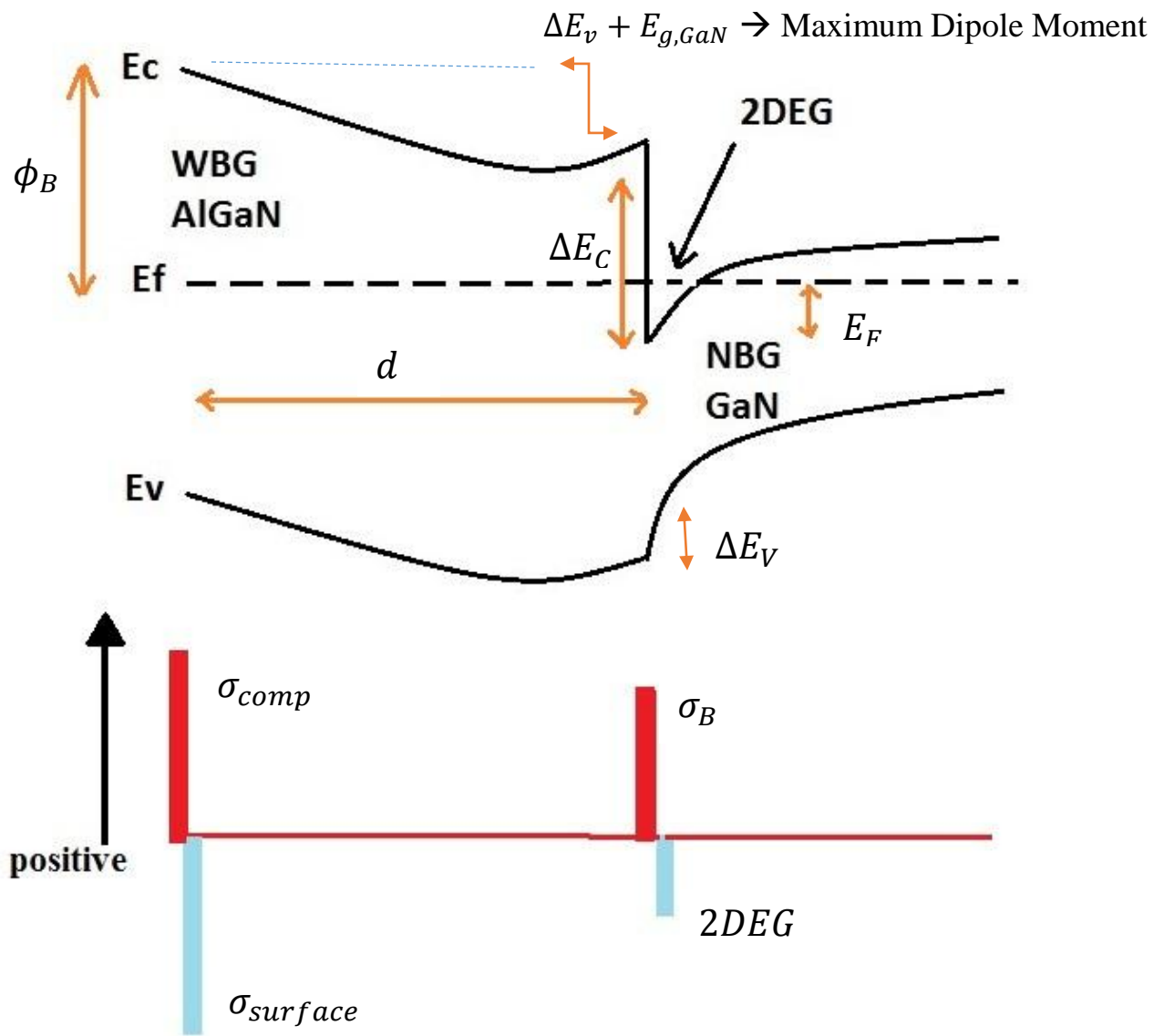
Figure 2.12 – Parameters defined in the 2DEG equation relative to AlGaN/GaN band diagram [8][32-33].

Table 2.4 below demonstrates the definition of each variable in figure 2.12.

Table 2.4 - Table of variables for Figure 2.12 [8][32-33].

Variable	Significance
ϕ_B	Schottky barrier height.
ΔE_C	Conduction band offset at the interface.
E_F	Penetration by the conduction band edge below the Fermi level measured at the interface.
ΔE_V	Change in valence band offset at the interface.
d	Thickness of the AlGaN layer.
σ_B	Net polarization charge at the interface given by $P_{(x)} = (Q_{\pi,}AlGaN) + (-Q_{\pi,}GaN) = \sigma_{int} = \sigma_{pol}$
$\sigma_{comp},$ $\sigma_{surface}$ $2DEG$	Fixed polarization charges generated by lattice mismatch between AlGaN/GaN. Length of bars in the graph determine the strengths of charges relative to the others. Also represented as $-Q_{\pi,}$ and $-Q_{\pi,}$ in figure 2.8.

The equation for 2DEG sheet carrier density is a function of mole fraction x and can be realized by the following equation [33-34]:

$$n_s(x) = \frac{+\sigma_B}{q} - \frac{\varepsilon_r(x)\varepsilon_0}{dq^2}\left[\phi_B(x) + E_F\big(n_s(x)\big) - \Delta E_C(x)\right] \qquad (2.7)$$

where $n_s(x)$ is the 2DEG sheet carrier density, q is the charge of an electron, ε_0 is the permittivity of free space, and ε_r is the permittivity of AlGaN. Unlike the MOSFET, there is no one universal formula for sheet carrier density. New publications are constantly being published that take into account other variables or phenomena that have been previously neglected, or newly discovered. However, the equation above is the general format of one of the most widely accepted equations for the 2DEG density as a function of mole fraction and material property.

For this thesis, the concept of the sheet carrier 2DEG density is significant. The former formula, along with the charge-control variation of the model are used in development of an analytical and numerical model. The charge-control model for sheet carrier density is discussed in more detail in Chapter 4.

2.7 Monokine Induced By Gamma-Interferon

Chemokine (C-X-C motif) ligand 9 (CXCL9) is a small cytokine with an atomic mass unit of 8-10 kDa that belongs to the CXC family of chemokines. It is also known as Monokine induced by gamma-interferon (MIG). The name comes from the fact that it is a potent chemoattractant induced by interferon gamma (IFN-γ) during infection, injury, or immuno-inflammatory response [18-20].This classifies MIG as a pro-inflammatory chemokine. A detailed three-dimensional depiction of MIG can be seen in figure 2.13.
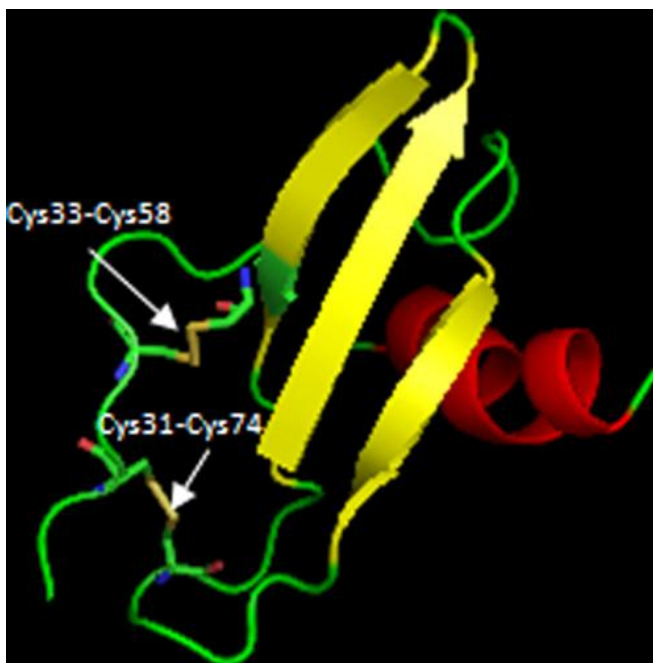
Figure 2.13 – 3D model of human CXCL9 (source: Interdepartmental Research Center for Computational and Biotechnological Sciences) [38]

According to the model developed by Trotta, Constantini, and Colonna (2009) shown in figure 2.14, the backbone ribbon of CXCL9 is shown in green, helices are noted in red, and β-strands are depicted with yellow arrows. Throughout this chapter, the terms MIG and CXCL9 will be used interchangeably.

Secretion of MIG is produced mainly from macrophages (by way of differentiation of monocytes, a type of white blood cell) and directly results in chemotaxis of various activated T lymphocytes (T cells) via the CXCR3 shared chemokine receptor (Figure 2.14) [36][38].

Figure 2.14 – 3D model of human chemokine receptor CXCR3. (source: Interdepartmental Research Center for Computational and Biotechnological Sciences) [38])

Upon interaction of the appropriate CXCL9 chemokine and appropriate receptor (CXCR3), they become binded through G-protein coupled receptors with seven transmembrane domains and release their specific biological function [38]. This function is to produce interferon-gamma (a type II interferon) to stimulate increased activity from local macrophages [38-41]. This type of interferon is characterized by two peptide chains (143 amino acids) that have N-linked glycosylations [39]. A three-dimensional model developed by Trotta, Constantini, and Colonna (2009) depicting this protein-protein interaction can be seen in figure 2.15.
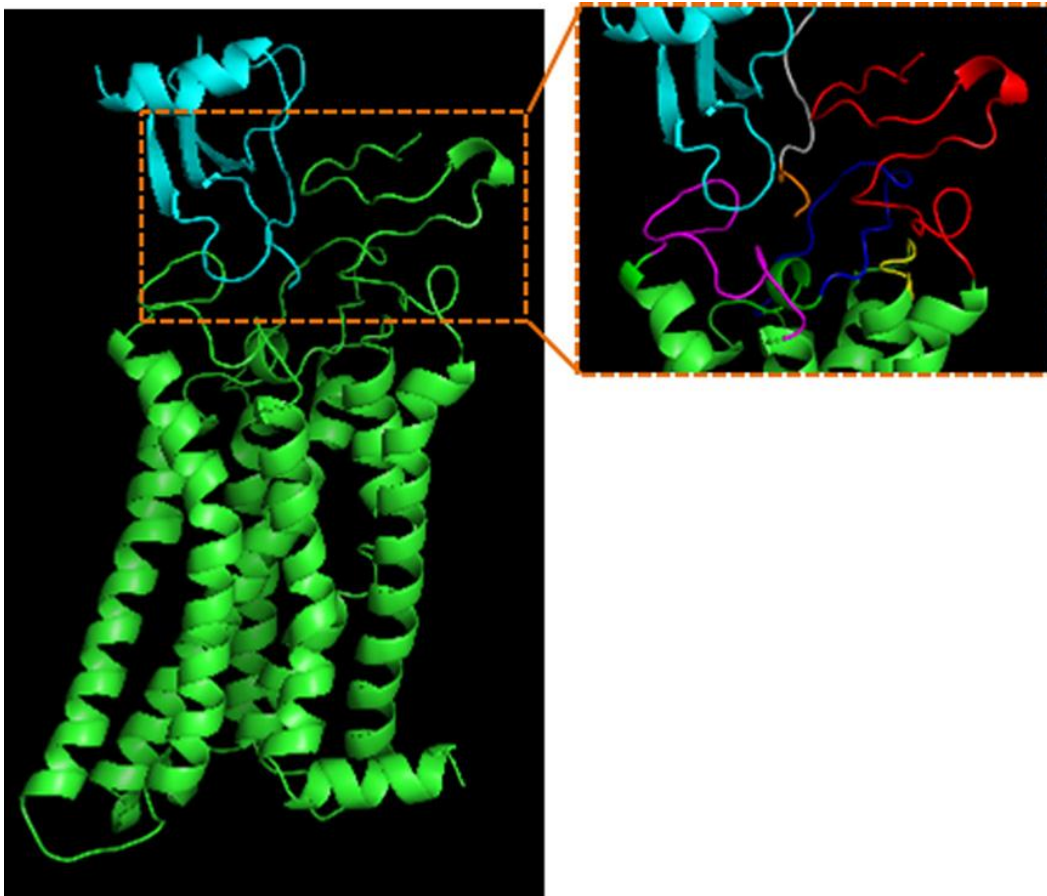
Figure 2.15 – Protein-protein interaction of CXCL9 and the CXCR3 chemokine receptor (source: Interdepartmental Research Center for Computational and Biotechnological Sciences) [38])

As noted by Trotta, Constantini, and Colonna, the green ribbon depicts the CXCR3 receptor, while the cyan ribbon depicts CXCL9 chemokine. A detailed image of the interactions can be seen in the right-most image. Extracellular loops 1, 2, and 3 are depicted in red, yellow, and blue respectively, while the N-terminal, and N-loop of the chemokine are depicted respectively in orange, and grey. In this image, the N-terminal is responsible for protein "docking" [38]. The N-loop region of CXCL9 interacts directly with the N-terminal region of CXCR3. Also, the N-terminal of CXCL9 interacts with Loops 2 and 3 of the CXCR3 receptor [38]. Detailed interactions of these proteins are beyond the scope of this paper and therefore will not be discussed. It is important however, to note how these interactions fit into the overall systemic response carried out by the human body upon recognition of a foreign allograft.

As mentioned before, the main function of the CXCL9 chemokine is to recruit leukocytes to sites of infection, injury, and inflammation [22]. A high-level overview of the process in which MIG is produced, assuming it isn't already existent as part of the non-specific immune system can be seen in figure 2.16.
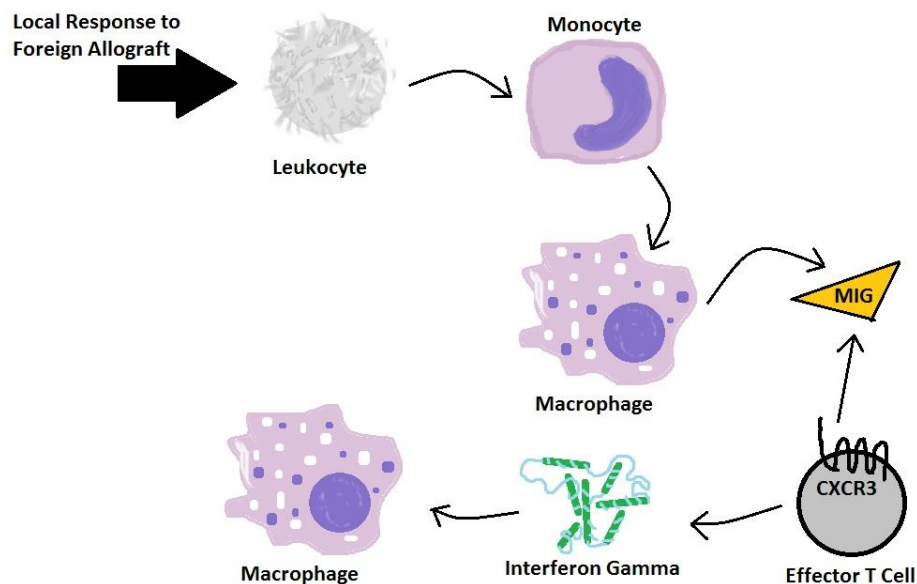
Figure 2.16 – A High level representation of how MIG is involved in allograft rejection [37-42]

Referring to figure 2.16, a flow chart of the process in which MIG is involved in allograft rejection can be seen as part of the immune system's local defense. Upon local recognition of a foreign entity (as part of the non-specific immune system), monocytes, a type of white blood cell, migrate from the blood stream and differentiate into macrophages in tissue. These macrophages, whose job is to engulf (phagocytose) foreign substances, are responsible for the secretion of MIG. MIG (CXCL9), along with CXCL10, and CXCL11 are agonists (trigger chemicals) for CXCR3, therefore Chemokine receptors present in Effector T-Cells bind with ligand CXCL9 (MIG) and transmit chemical cell signals. These chemical signals attract T_H1 cells (via chemotaxis, figure 2.17) and promote T_H1 maturation. T_H1 cells secrete interferon gamma (IFN-γ) which not only promotes Natural Killer cell (NK cell) activity, but also acts as an important activator of macrophages [38][40-42].
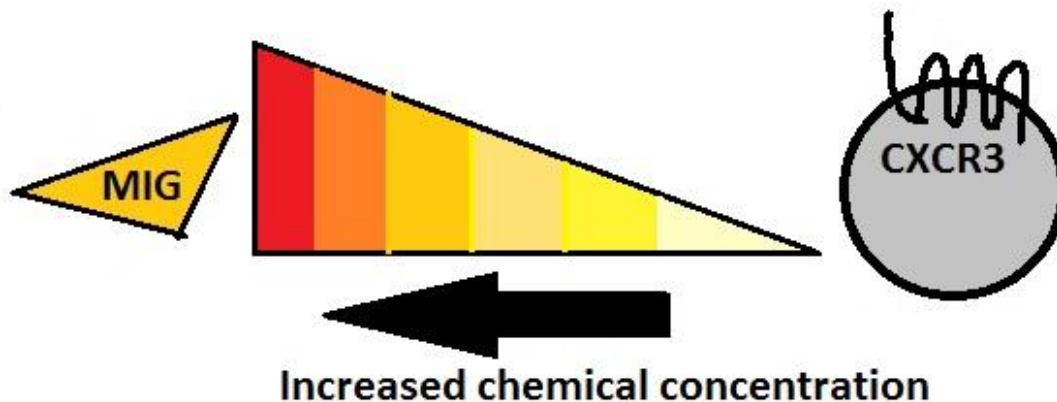
Figure 2.17 – Chemotaxis in action [43]. MIG, a chemoattractant, induces a response along a chemical gradient from cells (T_H1) that contain the right receptors (CXCR3).

2.8 MIG significance in biomedical engineering

Monokine induced by interferon gamma (CXCL9 / MIG) is a critical biological marker for determination of transplant rejection. The secretions of MIG have been shown to be expressed in acute and chronic allogeneic skin grafts / allografts several days before completion

of rejection and if gone untreated can result in the destruction of the transplanted organ / skin graft by the body's own immune system [37][44-46]. Range of concentration in normal human states is approximately 0.2-3 ng/mL (or 40-100pM) while concentration in pathophysiological disease states are 10-400 ng/mL (or as high as 34nM) [47-48]. In addition, it is a highly charged particle, having around net 20 positive charges per molecule [48-49]. This makes it an ideal candidate for detection methods that utilize changes in electric potential. Early detection of this key biomarker is significant and can result in quicker/appropriate treatment (Anti-T-Cell Treatment or Antibody neutralization of MIG/CXCL9 interactions) [38][46].

CHAPTER III

METHODOLOGY

In this chapter the methodology of the development of an amperometric biosensor using Gallium Nitride material based high electron mobility transistors is discussed. The realization of such a biosensor depends primarily on three main concepts: Careful observation of normal clean device operations, careful chemical modification of the device, and careful monitoring of chemically modified device operations. For the first requirement, certain characteristics must be measured such as threshold voltage, and floating gate drain current. This provides a reference point from which key changes are compared and contrasted. For the second requirement, a specific chemical procedure is exercised to ensure that the sensor's full potential is realized. This is to ensure it is repeatable multiple times across multiple devices. For the final requirement, careful monitoring, and observation must be exercised to confirm that any changes in performance are accurately reported.

3.1 Biosensors

Over the past several years, there has been much research and development into developing newer and less invasive ways to monitor and detect several different biological cells and molecules. Such biological elements include but are not limited to: proteins, enzymes, antibodies, and tissue cells. The need for such development arises from the current way physicians obtain data from patients. Invasive methods, such as biopsies and cardiac

35

catheterization, require making incisions and taking samples or inserting devices into the suspected tissue/organ [20-21]. With new advances in medicine and technology, there is an exponential growth in the understanding of key biomolecules that play certain roles and functions in the development of disease. Using these discoveries, it is possible to develop biosensors that can harvest energy/signals from these biomolecules and interact with them in such a way to paint a non-invasive and precise picture of the health status of a patient. Commercially available, and popular examples of biosensors in the commonplace world today are glucose monitoring devices, and pregnancy tests [50].

Biosensors are generally accepted to consist of two main parts: a sensing element, and a bioelement [50]. Usually the bioelement must be immobilized on some sort of sensing surface. The procedure in which this is done can vary from sensor to sensor. The general idea is for the biological element to recognize a solely a certain target analyte. The resulting interaction is transduced directly into a measurable medium (electrical current, light emission, mass, etc.).

While the function of a biosensor can be loosely applied to any system that achieves similar outcomes, it is not accurate to say that there is only one type of biosensor. A few of the different types of biosensors can be seen in figure 3.1 [50].
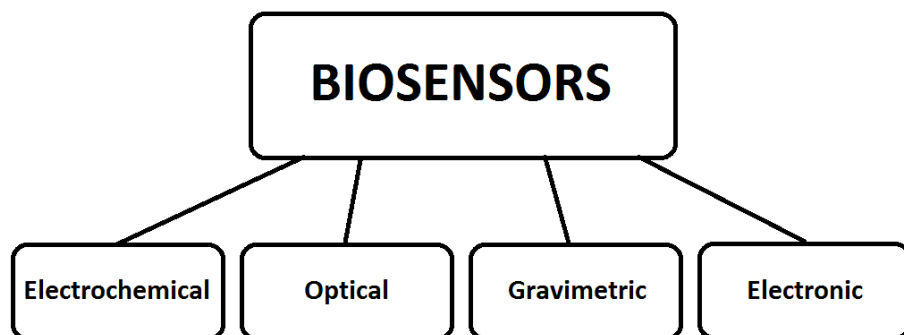
Figure 3.1 – A few categories of biosensors

Optical biosensors work by determining changes in light absorption upon interaction of the analyte and biomolecule, while gravimetric biosensors work by detecting changes in mass. Electronic and electrochemical biosensors work by measuring changes in a measurable signal and can be further divided into several different categories: conductimetric biosensors, amperometric biosensors, and potentiometric biosensors [50]. Conductimetric, as the name implies measures changes in conductance and/or resistance. Potentiometric sensors measure changes in potential/voltage, and amperometric sensors measure changes in current. In this thesis, an amperometric biosensor is proposed using the HEMT device, which measures the difference in current levels, and is discussed in further detail in the following sections.

3.2 Procedure

In order to detect Human MIG, first the gate electrode of the device must be functionalized using thiol chemistry. By utilizing gold-plated surface electrodes of an available GaN based HEMT device, a self-assembled monolayer (SAM) is constructed to immobilize a target antibody through a process called crosslinking. A benefit of using the AlGaN/GaN device is that it is chemically inert and can be operated without the need of a reference electrode.

3.2.1 Crosslinking with DSP and construction of the SAM layer

Crosslinking, is the chemical process of joining together two or more molecules by way of covalent bond [51]. This technique is also called bioconjugation when used to refer to the joining of proteins. Molecules that contain this ability to join two or more molecules are called crosslinkers or crosslinking reagents. Their mode of action is by targeting specific functional groups on proteins. These functional groups can be amine groups, carboxyls, sulfhydryls, or carbonyls for example. This is due to only a small number of protein functional groups being

37

able to possess suitable targets for crosslinking [51]. Crosslinkers are chosen based on certain features that are specific for different reactivities. There are four different features that need to be considered when selecting a suitable crosslinker: chemical specificity, spacer arm length, water-solubility/cell membrane permeability, and spontaneously reactive or photo-reactive group capability [51]. Chemical specificity refers to the reactive ends present in the crosslinker. Generally, a crosslinker can contain two identical reactive groups at each end (homobifunctional), or two different reactive groups present at each end (heterobifunctional). For the application specific to this thesis, it is desired to choose a crosslinker that contains two identical reactive groups. Since it is required to immobilize only one certain type of protein, a homobifunctional crosslinker is used to increase the binding capacity. Spacer arm length gives the molecular span of the crosslinker, and can estimate the distance between conjugated proteins [51]. Cleavability also falls into this category and refers to whether the bonds between conjugated proteins can be broken (cleavable) or not (non-cleavable). For the application specific to this thesis, cleavability is something that needs not be worried about. Water-solubility and cell-membrane permeability refers to whether or not the crosslinker can permeate through cell membranes and crosslink proteins that are hydrophobic (afraid of water), or that exist within a membrane [51]. For the application specific to this research, this is a good feature to have due to the cellular component of CXCL9 (MIG) containing a plasma membrane. Finally, spontaneously reactive or photoreactive group capability refers to whether or not the crosslinker reacts as soon as a sample is added, or by the addition of a UV light source [51]. For this research, after careful consideration of the former categories of consideration, a decision is made to use dithiobis succinimidyl propionate as a crosslinker.

Dithiobis Succinimidyl Propionate (DSP, or Lomant's reagent) is a homobifunctional crosslinker that is also membrane permeable to allow for intracellular crosslinking [51]. DSP possesses identical amine-reactive N-hydroxysuccinimide (NHS) esters at both ends of a cleavable 12 Å spacer arm. At pH 7-9 the NHS esters present in DSP react with primary amines in proteins to form stable amide bonds. This crosslinker is chosen because its reactive groups are able to successfully form covalent bonds with the primary amines in our target antibody (Anti-MIG). Secondly, the disulfide linkages in DSP are known to chemisorb rapidly to gold surfaces, while the NHS reactive groups present on each end of the crosslinker remain intact and available for attachment to primary amines in proteins [51-53]. figure 3.2 below shows the molecular structure of DSP.
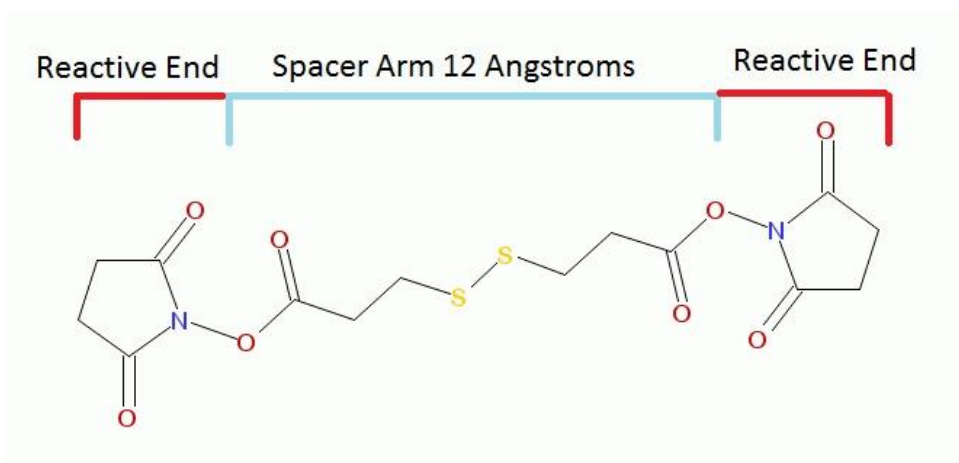
Figure 3.2 – Molecular structure of DSP [52]

The bonds created by the attachment of DSP to gold is one of the most important key aspects of this crosslinker, and assists in the immobilization of the target antibody [53]. The linkage formed between DSP and the gold surface is very stable, exceeding the strength and stability of covalent silane bonds with glass [53]. Utilizing gold plated electrodes on the device, a self-assembled monolayer (SAM) is constructed using the crosslinker. Then, the target antibody, Anti-MIG is

39

introduced to the crosslinker to complete the construction of the SAM layer. After completion of

this step, the sensor is ready to use. A visualization of a prepared biosensor can be seen in figure

3.3, while an enhanced, theoretical visualization of the SAM layer can be seen in figure 3.4.
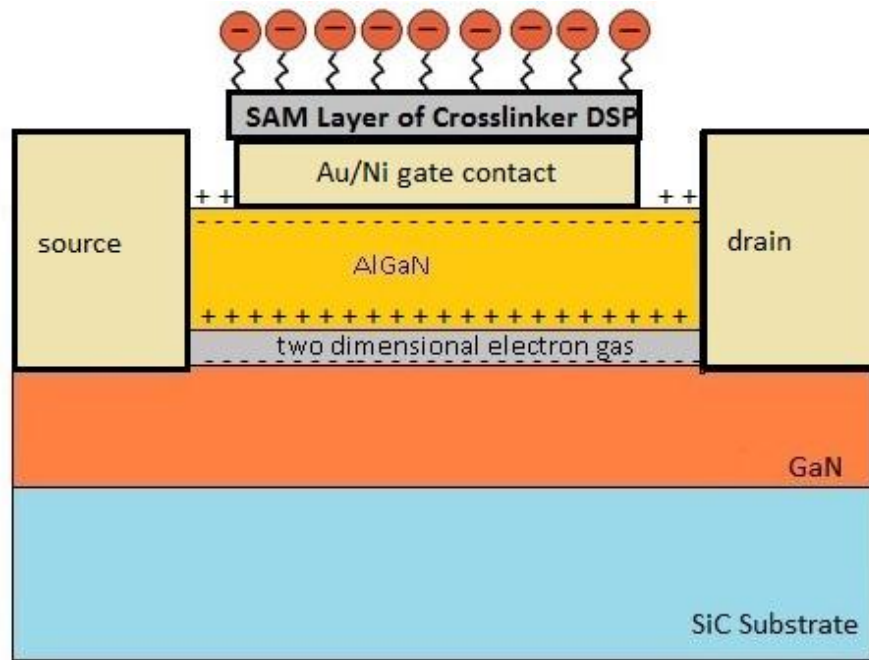
Figure 3.3 – Charged biosensor on SiC substrate
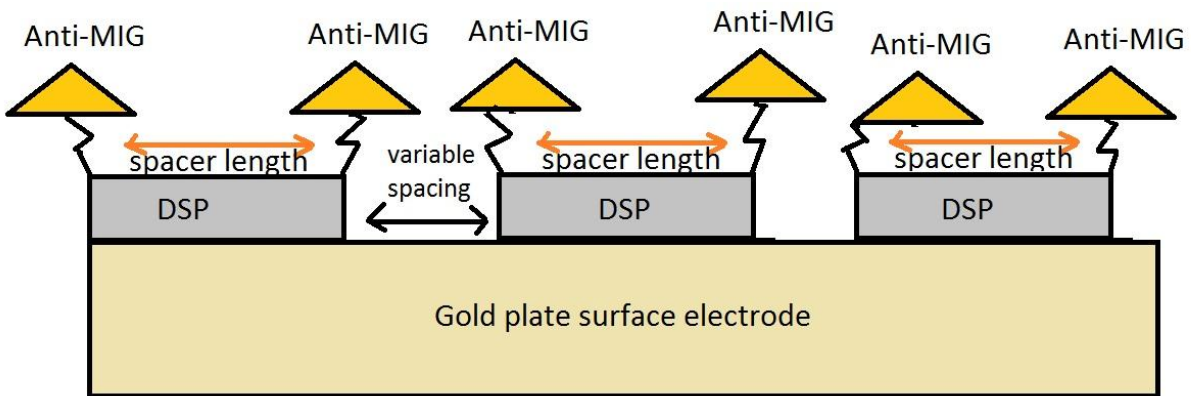
Figure 3.4 – Enhanced visualization of the theoretical SAM layer

As can be seen in figure 3.3, the biosensor consists of an AlGaN HEMT on a silicon carbide substrate. Spontaneous and piezoelectric polarization charges are included for reference. In figure 3.4, the SAM layer is depicted at a closer view. This layer consists of covalently bonded DSP molecules to a gold plated surface. The immobilized proteins are attached to the two reactive ends of the DSP. They are separated by the spacer arm length, which for DSP is 12 Å [52]. There is a further variable spacing between the DSP molecules that is due to the non-uniformity bonding of the DSP molecules to the gold surface. In Chapter 6, a detailed SEM image of the SAM layer is provided and discussed.

3.3 Proposed biosensor mode of action

As the highly charged protein is immobilized on the surface through crosslinking, an increase in drain current occurs, as the positive surface charge potential is altered and the resulting sheet charrier concentration (2DEG) in the hetero-interface is influenced [54-55]. The accumulation of these immobilized charges cause this change in surface states by extending the depletion region [8]. The antibody (Anti-MIG) only interacts with the target analyte (MIG), and upon introduction of the analyte, binding occurs to the immobilized Anti-MIG. The positively charged MIG pairs with the negatively charged Anti-MIG, neutralizes it, and the resulting activity alters the conductivity of the channel once again by changing the charge distribution in the conjugated molecules, ultimately resulting in further change in surface states of the AlGaN/GaN HEMT gate surface [14-19][23][47][54]. This produces an observable decrease in drain current. The charges induced by these events are by way of capacitive coupling and therefore are analogous to the application of a DC bias at the gate surface. [54-56]. A visualization of this process can be seen in figure 3.5.

41
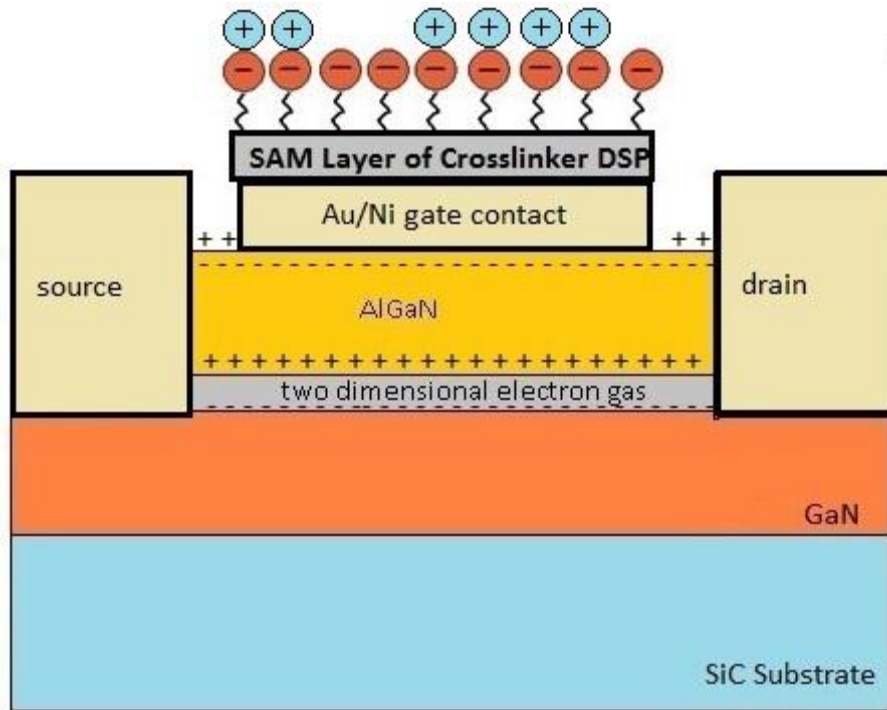
Figure 3.5 – Biosensor after protein conjugation

In figure 3.5, it can be seen how the charge distribution of immobilized surface charges on the

gate is altered by the addition of the target analyte (MIG). This visualization is further elaborated

on in chapter 4 and chapter 5, where the mathematics and theory behind this phenomenon is

developed analytically and numerically.

CHAPTER IV

ANALYTICAL MODELING OF THE BIOSENSOR

In this chapter, the theory behind the development of an analytical and numerical model for the proposed AlGaN/GaN based HEMT biosensor is discussed. An analytical method is developed using the Charge-control model for AlGaN/GaN based HEMT devices, John Albrecht's equations for low-field mobility, and chemistry techniques. Then, the analytical model is furthered elaborated on numerically using SILVACO™ and used as a basis to understanding the quantum mechanical functions of the proposed biosensor in the real-time experimental applications seen in Chapter 6.

The analytical and numerical models are developed on the basis that there exists surface states that are products of the large polarization fields discussed in Chapter 2. These surface states have been widely accepted to be directly influential on the formation of the 2DEG, and are also attributed to some of the negative effects in AlGaN/GaN HEMT devices, such as current collapse [55][57][24][58-60]. This phenomena has become so critical in recent heterostructure devices that it has become the subject of much research and analysis. Introductory detail on the nature and importance of these surface states is provided as a prerequisite, along with the mechanism of charge transfer of an electrolyte to the gate electrode. These are important considerations to the analytical and numerical models developed in this thesis.

4.1 The science of the surface states in AlGaN/GaN HEMT devices

By now, it is clear that spontaneous and piezoelectric polarizations play a major role in the development of the 2DEG in the AlGaN/GaN interface. Numerous studies performed in the past 20 years have widely accepted the fact that charged surface states in the intrinsic and extrinsic HEMT devices are directly responsible for the origin of the 2DEG at the interface [55][59-62]. This widely accepted theory is first thought to be proposed by Ibbetson et al. (2000) by means of strong empirical data [55][61].

The theory of surface states maintains that there are two different kinds of surface states in a crystal that come about when the periodicity of the crystal lattice is interrupted. These surface states are intrinsic surface states, and extrinsic surface states [55]. Intrinsic surface states are surface states that are present on the implication that the surface of the crystal is perfect. When the periodicity of the crystal lattice is abruptly broken, "dangling bonds" result, indicating that the surface atoms contain unsatisfied valence shells [55]. They were first demonstrated by William Shockley and Igor Tamm using two mathematical approaches, and for this reason, they are also referred to as Tamm-Shockley states. Intrinsic surface states can both be represented as either solutions to the Schrödinger equation (Shockley states), or by using the tight-binding model (Tamm states). They can take on donor-like states if they originate at the conduction band, and acceptor-like states if they originate at the valence band [55][61-62].

Contrary to intrinsic surface states, extrinsic surface states are caused by defects in the growth process and/or impurities introduced to the device during the procedure. In 1988, William E Spicer noticed that a perfect GaAs crystal exhibits no surface states intrinsically, yet exhibits noticeable surface states when examined on in situ experiments [55][63]. This prompted him to develop a defect model that to this day is still widely accepted and used to explain

extrinsic surface state defects in crystals and Fermi level pinning in III-V semiconductors [55][63].

In 1969, a paper published by S. Kurtin et al. in which the Schottky barrier height Φ_{Bn} of various metals on different semiconductor compounds is plotted versus electronegativity X_M of the metal. The slope of the line, S, is represented as a fundamental parameter in determination of a predictability of a junction to contain surface states [64]. The slope is given by the following equation, and is found to be inversely proportional to the degree of Fermi-level stabilization [64].

$$S = \frac{d\Phi_{Bn}}{dX_M}$$
(4.1)

In this study, it is found that the slope is approximately equal to 1 in a "strongly ionic" material, indicating no Fermi level stabilization. Contrarily, a slope closer to 0.1 indicates a "strongly covalent" material, and a nearly complete Fermi level stabilization [64]. This work lead to the conclusion that a "strongly ionic" material is characterized by a small density of surface states while a "strongly covalent" material is characterized by a large density of surface states. The terms "ionic" and "covalent" as categories for semiconductors have been disputed over the years by physicists, but this work does an excellent job at predicting the presence of surface states in general Schottky/semiconductor junctions [55]. According to Ramakrishna Vetury (2000), the slope of GaN as applied to equation 4.1 is greater than 1, which would place it the "strongly ionic" category. This would suggest little to no density of surface states. However, as of now it is known that surface states do indeed exist on the GaN crystal surface, and certainly exist as a result of an AlGaN/GaN heterostructure, so the existence of some other influential entity had not been taken into account previously. At the moment, current understanding of solid state physics

draws the conclusion that these surface states are products of the spontaneous and piezoelectric polarizations [55][59-62].

According to experimental hall data on AlGaN/GaN HEMTs by Ibbetson et al (2000), in order to satisfy net neutrality on the device, the sum of the total space charges should be zero in the absence of an external electric field [61]. This introduces the net neutrality equation for AlGaN/GaN HEMT devices and is given by [60-61]:

$$\sigma_{Surface} + \sigma_{AlGaN} + \sigma_{pol} + \sigma_{buffer} - qn_s = 0 \qquad (4.2)$$

where $\sigma_{Surface}$ is the charge contributed by ionized surface states, σ_{AlGaN} is the charge due to ionized donor states in the AlGaN layer, σ_{pol} is the net charge present at the interface, σ_{buffer} is the net charge due to the GaN layer, nucleation layer, and substrates all combined into one term, q is the elementary charge of an electron, and n_s is the sheet carrier density of the 2DEG. A few important conclusions can be made from the above equation based on some fundamental understandings of an intrinsic AlGaN/GaN HEMT device. The dipole created in the AlGaN layer due to the combined effects of spontaneous and piezoelectric polarizations contains poles that are exactly opposite and equal in magnitude, so by convention, the total net spacial charges contributed by these two poles cancels out and thus dismiss the concept of "piezoelectric doping" [61]. Also, in order for the negatively charged 2DEG to be confined to the quantum well at the AlGaN/GaN interface, the total polarization in the buffer must have a net negative charge. However, we can ignore this term on a transistor grown optimally on a substrate with little to no lattice mismatching, which is usually accomplished by the careful engineering of a nucleation/buffer layer [61]. This nucleation layer creates a smooth transistion from the GaN bulk to the substrate and eases the bulk-to-substrate lattice matching, which normally contains a slightly to drastically different lattice constant (depending on the substrate material) [65]. By

46

carefully engineering this layer such that the transition from bulk GaN material to substrate is smooth, the polarization due material strain becomes negligible. This theoretical absence of polarization in the substrate should ideally maintain that the Fermi level in the transition from bulk GaN to substrate sits near the conduction band [61]. Furthermore, Ibbetson determined that while σ_{buffer} affects the 2DEG sheet carrier density, it is highly unlikely that electrons thermally generated in this buffer are a source of electrons in the quantum well, because they would need to leave behind a positive space charge if this were true [61]. It is also further suggested that in an ideal undoped AlGaN/GaN HEMT, the net contribution due to polarization charges in the AlGaN dipole, interface, and buffer (σ_{AlGaN},σ_{pol},σ_{buffer} respectively) is zero [60-61]. By reformulating 4.2, we get:

$$\sigma_{Surface} = qn_s \qquad (4.3)$$

The equation in 4.3 shows that the sheet carrier density at the interface is directly impacted by the surface states in the AlGaN/GaN HEMT. This was experimentally proven by Ibbetson, in which it is concluded that any negative surface states degrade the 2DEG and are a result of the transfer of electrons into acceptor-like surface states [61]. Also, any positive surface states are a result of electron transfer from donor-like surface states into lower energy GaN acceptor states [61]. This study first developed the notion that spontaneous and piezoelectric polarizations create the quantum well at the interface, but the surface states are responsible for the accumulation of electrons there [61]. A depiction of the parameters defined in equation 4.2 and their contribution to the device can be seen in figure 4.1.
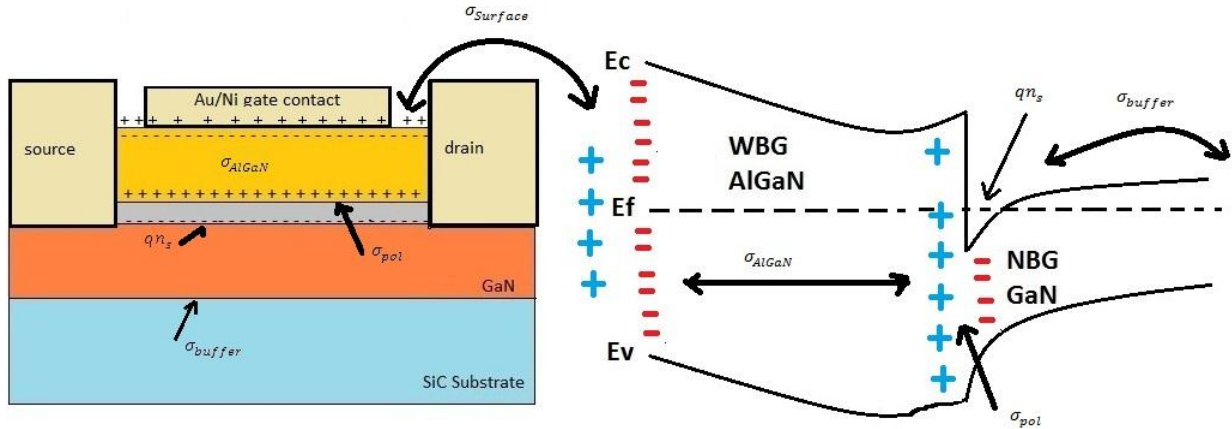
Figure 4.1 – Visualization of net neutrality on the AlGaN/GaN HEMT

As can be seen in figure 4.1, there exist surface states both on the free AlGaN surface, and the Au/Ni Schottky gate contact, and their total surface states can be combined to develop a net amount. Up to this point all surface states that have been discussed have been states that are assumed to be on the free surface of the AlGaN layer. But what about the gate electrodes contribution to these surface states? Does the metal play any significant role in these surface states? Recent studies suggest that it does. In the following section, the role of the metal in the contribution to net surface states is discussed.

4.2 The influence of the Schottky-semiconductor junction on surface states

In the 1940s, The Schottky-Mott model accurately predicted the Schottky barrier height in a metal-semiconductor junction based on the metal's work function, ϕ_B, and the electron affinity, χ, of the semiconductor and can be seen in the following series of equations [66-67]:

$$\phi_B^n = \phi_M - \chi \tag{4.4}$$

$$\phi_B^p = \left(\frac{E_G}{q}\right) + \chi - \phi_M \tag{4.5}$$

where ϕ_B^n corresponds to Schottky barrier height for an n-type semiconductor, ϕ_B^p, corresponds to Schottky barrier height for a p-type semiconductor, E_G is the bandgap energy, ϕ_M, is the metal work function, q is the charge of an electron and χ is the electron affinity of the semiconductor [66-67]. The Schottky-Mott model, while theoretically accurate at predicting band bending in the semiconductor, fails to account for Fermi level pinning. This essentially means that in this scenario, the Schottky barrier height becomes unphased by the metal work function. This is due to the model posing the assumption that the semiconductor contains ideal interfaces and possesses no surface states, which experimentally does not usually hold [67-69].

In 1947, John Bardeen made further contribution to this model that explains the observed Fermi level pinning in metal-semiconductor junctions. This model assumes a very high density of surface states for the semiconductor. In this model it is derived that these highly dense surface states persist underneath the metal overlayer and absorb a large amount of the metal's charge leading to the bands of the semiconductor aligning to a position convenient to that of the surface states. This ultimately leads to Fermi level pinning. At this point the influence of the metal work function becomes negligible [70]. In current understandings of solid state physics, it is now known that in an ideal Schottky junction, the Fermi levels of both the metal and semiconductor must align after thermal equilibrium. A previous knowledge of the work function of the metal and electron affinity of the semiconductor would allow an accurate prediction of Schottky barrier height [71]. Since the Fermi level must align at the interface of these two materials, charges must flow between the two materials to bend the bands appropriately as first predicted by Bardeen [70-71]. However, this model was further deemed as incomplete by Cowley and Sze in 1965 [72]. In the Bardeen model, it is assumed that the work function of a deposited metal onto a semiconductor has no effect on the Fermi level's position at the interface [71]. Cowley and Sze

49

conducted experiments in which different non-polar materials are used with different metal

contacts to view changes in surface states after metal deposition [72]. This study suggested that

not only is the deposition of metal causing a noticeable change in surface states, but also the

Schottky barrier height is dependent on the nature of these interface surface states [71-72]. A

depiction of Schottky junction metal work function vs band diagrams in n and p type

semiconductors can be seen in figure 4.2.
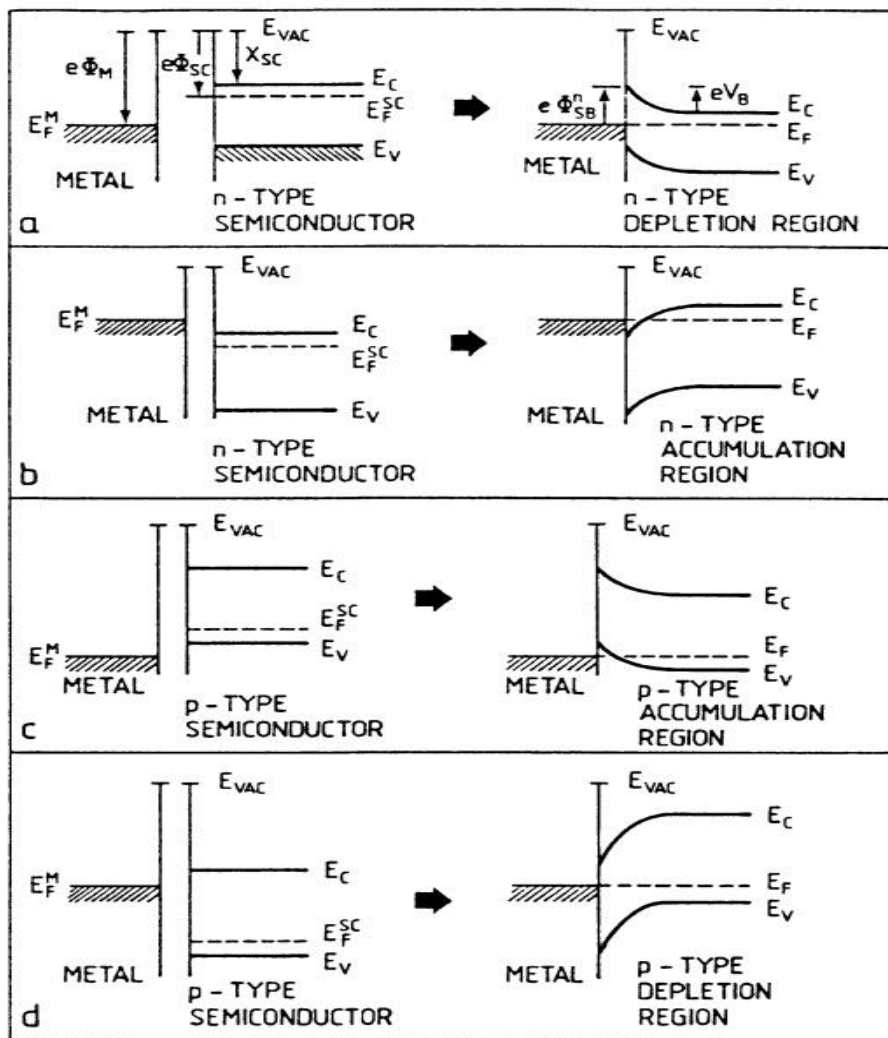
**Figure 4.2 – Effect of Schottky barrier height on the band diagram in semiconductors
(source: H. Luth, *Solid Surfaces, Interfaces, and Films* (2001))**

In this figure, boxes a and b depict the effect of a high metal work function, and a low metal work function on an n-type semiconductor respectively, while boxes c and d depict the effect of a high metal work function, and a low metal work function on a p-type semiconductor respectively. The band bendings in these diagrams correlate to Poisson's equation (eqn 2.3) and the charge transfer between these two materials can result in newly formed interface states, defect states, and production of dipoles [71]. Unfortunately, the current Schottky model for description of metal-semiconductor junctions cannot be applied to the Schottky gate in AlGaN/GaN based HEMTs. Recent experiments have shown the deposition of metal in formation of a HEMT not only reduces the Schottky barrier height, but also reduces the 2DEG by both partially neutralizing surface states, and redistributing them [69][72]. This is thought to be due to the net polarization charges present in the AlGaN layer. Furthermore, the barrier height is also a function of AlGaN barrier thickness and Al mole fraction which according to Goyal and Fjeldy, places the AlGaN/GaN Schottky barrier behavior somewhere between the Schottky-Mott model and the Bardeen model (2013) [69]. The new AlGaN/GaN bare surface model demonstrates experimentally by carefully examining surface donor density (donor-like surface states) and their distribution before and after the deposition of a Schottky gate metal (Ni). Their findings show that upon deposition of a metal, the Schottky barrier height, and 2DEG are reduced as the surface states are influenced by both the metal, and its alloy composition [69]. The bare surface model yields:

$$q\Phi_b = \frac{(n_o E_d + \sigma_{pz}/q)d + \varepsilon_{AlGaN}\,\Delta E_c/q^2}{n_o(d + \varepsilon_{AlGaN}/q^2 n_o)} \tag{4.6}$$

$$qn_s = n_o d\,\frac{\sigma_{pz} - \varepsilon_{AlGaN}(E_d - \Delta E_c)/q}{n_o d + \varepsilon_{AlGaN}/q^2} \tag{4.7}$$

where n_o is the surface donor density, E_d is the surface donor level, ΔE_c is the conduction band offset, d is the AlGaN barrier thickness, σ_{pz} is the polarization charge density, and $\mathcal{E}_{AlGaN}$ is the permittivity of the AlGaN layer. Since in this equation n_o and E_d depend on the work function of the metal, it can be seen from equations 4.6 and 4.7 that Schottky barrier height (Φ_b), and 2DEG sheet carrier density (n_s) do too.

To test their conclusion, a simple Silvaco simulation is conducted where a sample AlGaN/GaN HEMT model is simulated twice with only the work function being changed. The model consisted of a 250 Å undoped layer with a composition of 0.3 grown on top of a 1.475 μm GaN bulk indendent of substrate. The gate electrode is 2 μm with equal 3 μm source to gate, and gate to drain spacing. The model is simulated independent of substrate.
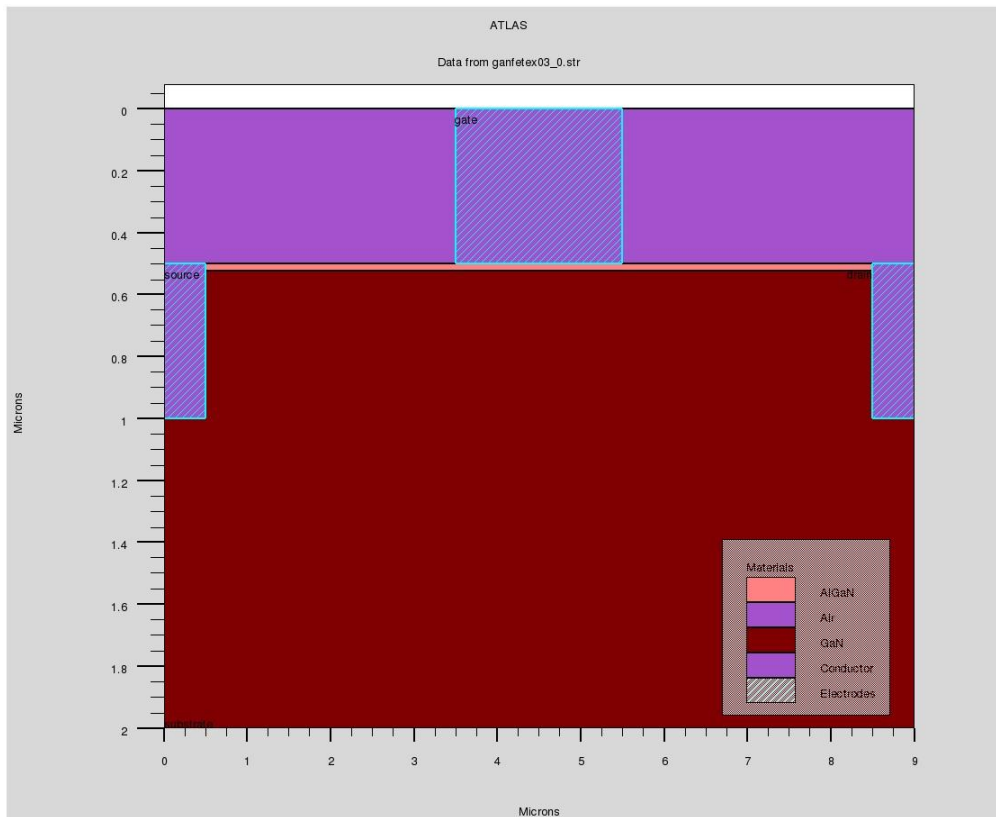
Figure 4.3 – HEMT SILVACO model developed to evaluate work function effect.

52
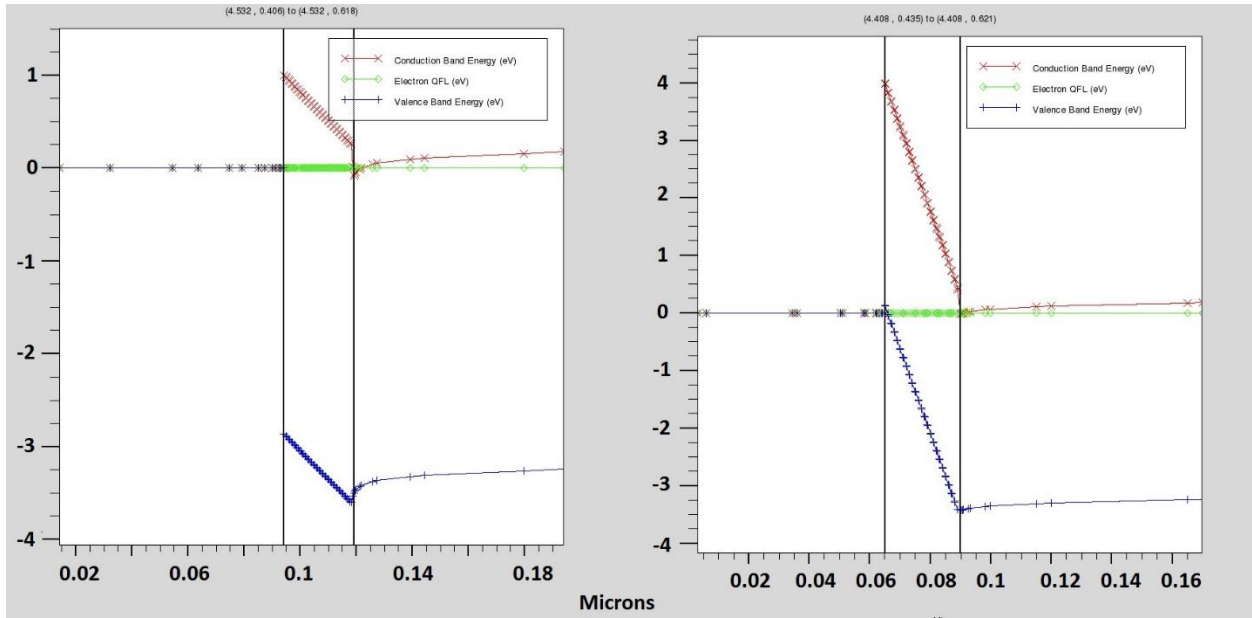
Figure 4.4 – Work function vs quantum well depth for work functions 5 and 8. (axes are enhanced for legibility and work functions 5 and 8 are seen from left to right respectively.)
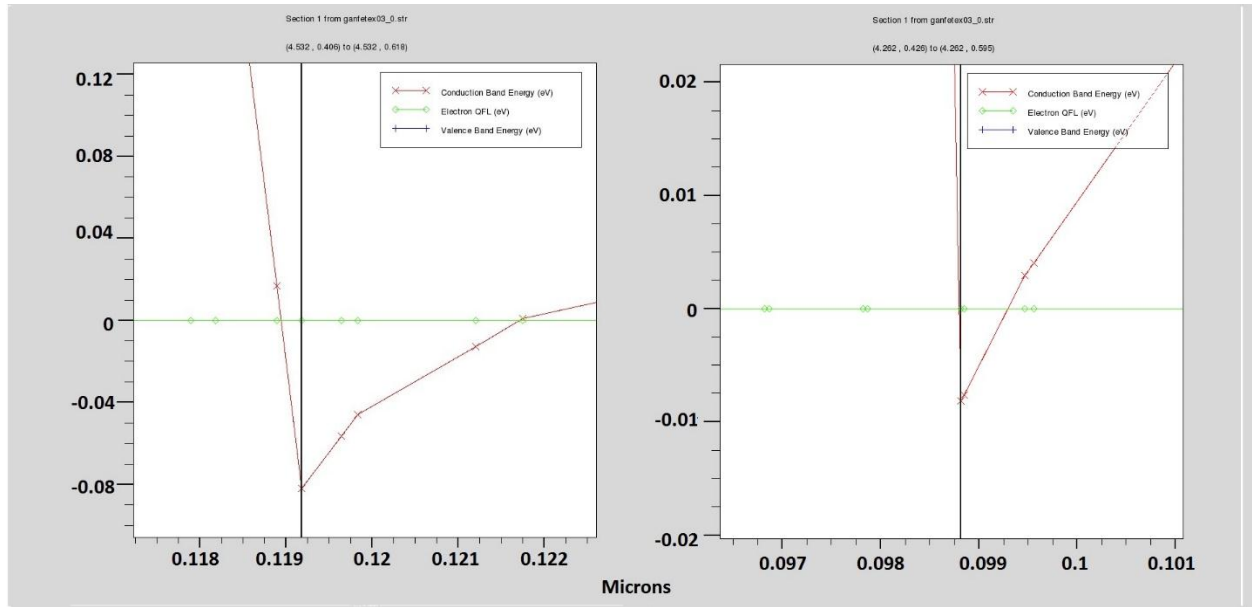
Figure 4.5 – Work function vs quantum well depth for work functions 5 and 8 zoomed. (axes are enhanced for legibility and work functions 5 and 8 are seen from left to right respectively.)

As can be seen by the previous figures, the bare surface model developed by Goyal and Fjeldy

holds true, as the quantum well area diminishes as the work function of the gate electrode

increases. This clearly leads to a reduced 2DEG density. In order to achieve the same 2DEG density, the AlGaN thickness or mole fraction would need to be increased (assuming all other values are held constant) as seen in the equation for 2DEG density (eqn 2.7).

The most important point that the Goyal-Fjeldy findings demonstrate, is that since the effect of the metal on the distribution in the band gap is dependent on the work function, it is possible to rule out the existence of high density surface states as demonstrated in the Bardeen model. However, since the Schottky-Mott model and its dependence on metal work function are also dependent on the assumption that there exists no surface states. It is then reasonable to conclude that surface states, while not distributed in a high density, most certainly exist on the AlGaN surface and are undoubtedly affected by the work function of the metal.

While the work function of a metal for the most part is constant, it is not governed by the characteristic bulk characteristics of the material, but more so on the condition of the surface [73]. The work function can be significantly altered by contaminant particles on the surface and/or chemical surface reactions (such as oxidation or chemical reactions/alterations) [73]. As the condition of the surface worsens, the formation of dipole barriers at the surface becomes apparent. This in turn, changes the amount of energy needed to remove an electron from the sample [73]. As the work function on a sample is measured and compared to the work function of its pure counterpart, the reading can give the researcher insight on the condition of the surface of the sample [73]. It has also been experimentally shown that an adsorption of a target at the surface changes the work function of that surface by altering its electronegativity [73-74].

This section draws many important conclusions that serve as a strong backing for the analytical and numerical models that follow. The notion that surface states in the AlGaN are influenced by the work function that are in turn, governed by the condition of the metal surface is

critical to the theorizing of analytical and numerical models. Before this, however, the mechanism of charge transfer and capacitive coupling of the charged solution onto the surface electrode must be discussed.

4.3 The Mechanism of charge transfer, and the double layer phenomena

The final prerequisite before the analytical and numerical models can be developed is the mechanism of action taken when a charged sample solution is left to incubate on the gate electrode. The concepts that follow are so greatly researched that they fall under a new sub-category of electricity and chemistry labeled electrochemistry. This category as a whole is concerned with the conversion of chemical energy into electrical energy [75]. Within this category of electrochemistry exists a branch that concerns itself with electrodes as a platform for chemical reactions to occur. This is a popular topic in the field of electrochemistry and still to this day is not fully understood. This section explains a mechanism of charge transfer between the target solution and the sensing platform.

When an electrolyte is adsorbed onto a metal, an interface is created between the electrode/electrolyte that is commonly called a double layer [76-77]. This phenomena is not limited to metals. It may also exist in alloys, semiconductors, insulators, liquids, and even polar and non-polar gases [76]. In the scenario where the interface consists of a metal and an electrolyte (as in the research presented in this thesis), there exists a potential between the electrolyte and the metal when the former is adsorbed on the latter [76-77].

The notion that a metal/electrolyte interface resembles that of a capacitance was first proposed in 1879 by Hermann von Helmholtz [76][78-79]. His model suggests that the interface between the metal and the electrolyte resembles that of a steady state capacitor. That is, two

parallel layers of opposing charges separated by a fixed distance [76]. The parallel-plate

capacitor model, or the Helmholtz model, is given by:

$$C_H = \frac{\varepsilon}{4\pi d} \tag{4.8}$$

where ε is the dielectric constant between the two "plates", and d is the distance separating them

[76]. This theory is suggestive that the capacitance is dependent on the distances between the

hypothetical "plates" and that changes in charge density between the metal and the electrolyte

are negligible [76][78]. Experimentally this was proved otherwise, but the model suggested by

Helmholtz helped pave the way for greater understanding of the effects between an electrode and

an adsorbate.

More than 30 years later, Louis Georges Gouy (1910), and David Leonard Chapman

(1913) proposed that the double layer in the theoretical "capacitor" is subjected to electrical and

thermal fields [76][78]. These two models would later be combined and dubbed the Gouy-

Chapman model. Their model proposed that a distribution of ions exists at the metal-electrode

interface that is subject not only to electrical changes, but also to thermodynamic changes of

particles in a solution. Furthermore, it is suggested by this model that there exists a diffuse layer

at lower concentrations. It is suggested that in a lower concentration electrolyte, the greatest

concentration of electric charge in the liquid would accumulate in a layer very near the electrode

as a result of the overcoming of thermal processes by electrostatic forces. Contrarily, as the

concentration becomes lower, the forces become weaker therefore separating the charges further

from the electrode [76-78]. This notion of thermal processes allows by definition, the Maxwell-

Boltzmann statistics can be applied. This, in turn, allows the capacitive model to be extended to

not only planar metal-electrolyte layers, but also to spherical ion-ion layers as well [76][78]. The

Gouy-Chapman model given by:

$$C_{GC} = \left(\frac{n_0 \varepsilon e_0^2}{2\pi kT}\right)^{1/2} \cosh\frac{e_0 V}{2kT} \tag{4.9}$$

where n_0 is the ion concentration per unit of volume in the electrolytic liquid, V is the potential drop between the metal and the electrolyte, k is the Boltzmann constant, ε is the dielectric permittivity, e_0 is the electronic charge, and T is the temperature [76][78]. This model, while good for modeling capacitances in low ionic concentration, fails to take into account ion-ion interactions. Thus, it cannot be used to model metal-electrolyte interfaces at higher ionic concentrations [76-78]. This prompted Otto Stern in 1924 to propose a new model that combines understandings from both the Helmholtz model, and the Gouy-Chapman model. His reasoning suggested that the charge distribution in the electrolyte solution is governed by two factors. The fact that ions are located at a finite distance from the metal surface (as suggested by Helmholtz), and that the charge distribution contains two charge effects (Gouy-Chapman): The first effect is that the greatest excess concentrated charges are immobilized on the electrode surface, and the second effect is that the weaker charges form a diffuse layer, spread out in the liquid, and decrease exponentially as the distance between the metal and the "charge plate" increases [76-78]. These two factors can be visualized as layers called the Helmholtz layer, and the diffuse (or Gouy-Chapman) layer respectively. Thus, the Helmholtz, and Gouy-Chapman models both exhibit contribution to the overall capacitive effect according to Stern. The total capacitance in this model is the Helmholtz capacitance in series with the Gouy-Chapman capacitance and is given by:

$$\frac{1}{C_S} = \frac{1}{C_H} + \frac{1}{C_{GC}} \tag{4.10}$$

where C_S is the Stern capacitance [76-78]. This leads to the notion that in concentrated electrolytes the capacitive effect is governed strongly by the Helmholtz approximation, while in dilute solutions the capacitive effect is governed by the Gouy-Chapman approximation [76][78].

Since electrolytes involved in charge transfer reactions are typically performed in an aqueous medium, a further contribution to the Stern model by Esin, Markov, Grahame, and Devanathan (1963) suggested that in between the Helmholtz layer there exists another layer comprised of partially solvated ions [77-78]. The solvents in these electrolytes can be water, or organic liquids. These solvents, however, are characterized as having a polarity [78]. It is suggested in this model that because of competitive adsorption, solvent dipoles are also contributors to the potential drop across the metal-electrolyte interface. A layer of dehydrated solvent dipoles can be thought of as the Inner-Helmholtz-Plane (IHP) while the previously theorized Helmholtz layer is regarded as the Outer-Helmholtz-Plane (OHP) [78]. The model derived is called the Triple-Layer Model and the equation for this model is the following:

$$\frac{1}{C} = \frac{1}{C_{M-1}} + \left(\frac{1}{C_{M-2}} + \frac{1}{C_{2-b}}\right)\left(1 - \frac{dq1}{dq_M}\right) \tag{4.11}$$

where C_{M-1} and C_{M-2} are the capacities between the metal and the IHP, and between the IHP and OHP respectively, C_{2-b} is the capacity of the diffuse double layer, and dq1/dqM is the rate of change for the adsorbed charge with respect to the charge on the metal [78]. This model raises a good point and is now is a commonly used model, along with the Gouy-Chapman-Stern alternative. Although the layer in this model is called the triple-layer model, generally a metal-electrolyte interface is still regarded as a double layer for convention. A depiction of the various models, along with their changes in potential vs varying distance can be seen in figure 4.6.
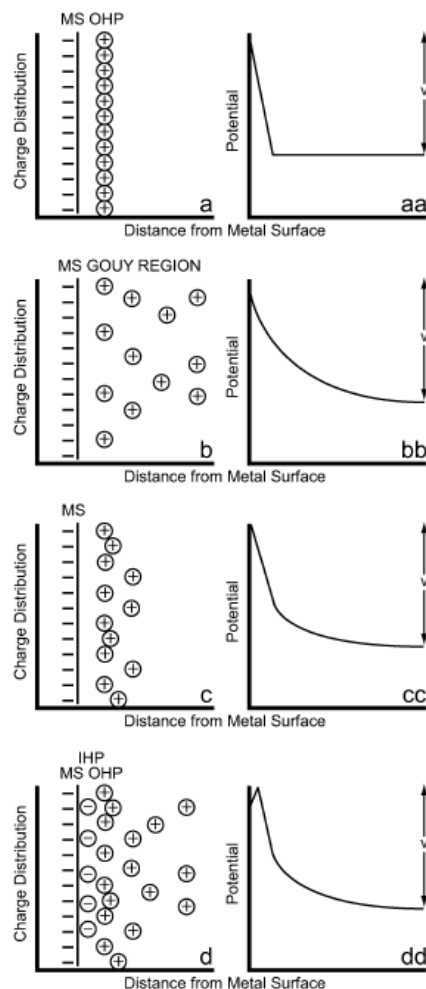
Figure 4.6 – Various double layer model properties with varying distance. (source: Delahay, Paul. *Double Layer and Electrode Kinetics* 1965)

In the figure above, blocks "a" and "aa" correspond to the Helmholtz model, blocks "b" and "bb" correspond to the Gouy-Chapman model, blocks "c" and "cc" correspond to the Stern model, and blocks "d" and "dd" correspond to the triple-layer model [76]. This representation assumes the metal surface (MS) has a net negative charge, but this can also exist the other way around, and has the same effect on ions of opposite charge. From the blocks "a" through "cc", the visualization of this "double layer" becomes apparent. The first layer consists of the adsorbed ions of greater charge to the surface through chemical interactions (Helmholtz layer), while the second layer (Gouy-Chapman layer) consists of the diffuse layer (loose weaker ions attracted to

the surface through coulombic forces) [76]. Also the potential in block "cc" (Stern Capacitance),

can be seen to be a summation of the potential curves seen in block "bb" and "cc". Nowadays,

researchers are incorporating new previously unknown, or previously neglected effects into the

double-layer phenomenon, but the triple-layer model is still the most widely accepted model.

Modern day findings, however, have helped for greater understanding of other phenomenon,

such as the concept of pseudo-capacitance [77]. A detailed figure depicting the double-layer, as

well as its effect on potential versus distance in its currently accepted form can be seen in figure

4.7.
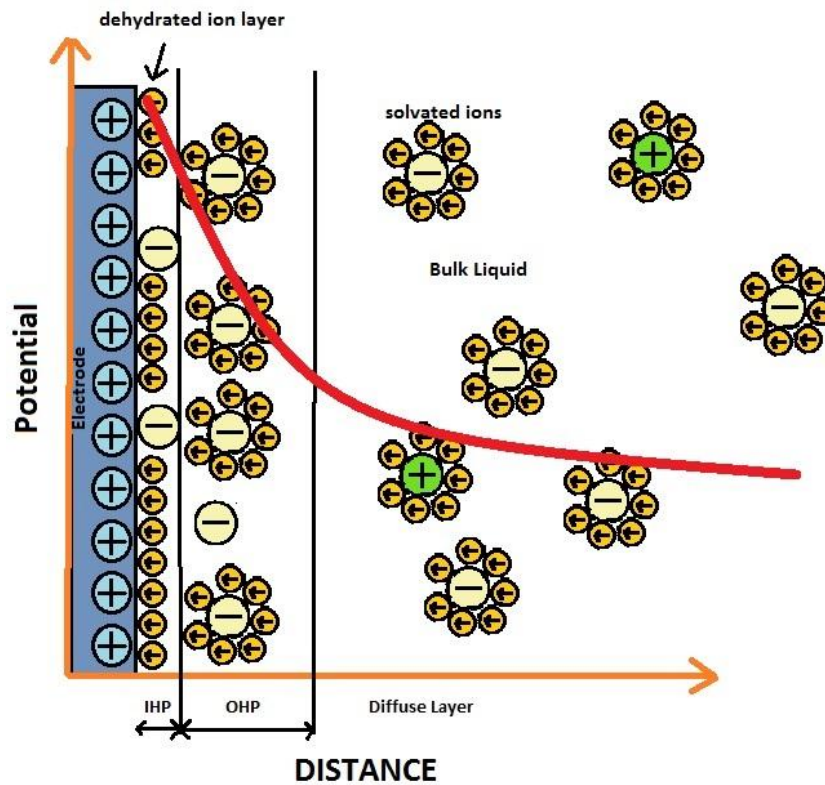
Figure 4.7 – Currently accepted double layer model for a metal-electrolyte interface [76-78]

This capacitance formed by the immobilized double-layer and the redistribution of charges at

each step in the methodology initiates a coupling effect with the transistor. Thus, it is safe to say

that the immobilizing of these charges on the gate surface are analogous to a DC bias through this capacitive coupling effect, where the floating gate voltage can be calculated as [56]:

$$V_{Floating} = \frac{Q_{Gate}}{C_{doublelayer}} \qquad (4.12)$$

Research done by Eliza et al. (2009) has concluded that this floating gate voltage contributes to the 2DEG density, and can justly be added to the original 2DEG density equation (eqn 2.7) to become [56]:

$$n_s(x) + \Delta n_s(x) = \frac{+\sigma_B}{q} - \frac{\varepsilon_r(x)\varepsilon_0}{q(d_d + \Delta d)}\left[\phi_B(x) + E_F - \Delta E_C(x) + V(x) - \frac{d_d + \Delta d}{d}V_{Floating}\right]$$

$$(4.13)$$

where $n_s(x)$ is the 2DEG sheet carrier density, q is the charge of an electron, ε_0 is the permittivity of free space, ε_r is the permittivity of AlGaN, d_d, and Δd correspond to the thickness of the AlGaN layer and the offset of the 2DEG from the interface respectively. V(x) corresponds to the channel potential at x, and $V_{Floating}$ is the floating gate voltage derived in equation 4.12 [56].

The conclusion of this section provides the final piece of theory needed to realize the AlGaN/GaN based HEMT biosensor's mechanical mode of action. The process of chemically modifying the gate of the device ultimately creates a chain of events. The double layer at the surface immobilizes highly charged molecules and initiates a charge transfer through capacitive coupling that acts as a DC bias on the gate. This altering of the surface of the gate electrode changes the work function of the metal (via chemical surface reaction) which affects the surface states in the AlGaN layer. Finally, as we know from the net neutrality equation, this modification of surface states directly affects the channel sheet carrier density (2DEG) of the AlGaN/GaN interface which results in an absolute change in drain current.

4.4 An Analytical model for the proposed biosensor

4.4.1 Modeling the biosensor using the Charge-Control Model

Now that the concept of net neutrality, metal-electrolyte interface physics, surface states, and the impact on these surface states by the metal electrode has been considered, an analytical model for a biosensor in the detection of human MIG (CXCL9) using AlGaN/GaN based HEMT devices on a silicon carbide (SiC) substrate is developed using the Charge-control model, John Albrecht's low field mobility equations, and chemistry techniques. The models are appropriate for ideal HEMT devices with the assumptions that surface states are present, and that net neutrality is satisfied at room temperature.

Assuming total depletion at 300K a two-dimensional theoretical model for the total 2DEG sheet carrier density in the AlGaN/GaN HEMT interface can be approximated by [81-82]:

$$n_s(x) = \frac{\varepsilon(x)}{q(d_d+d_i)}(V_{gs} - V_{th} - \frac{E_F}{q}) \qquad (4.14)$$

where q is electron charge, $\varepsilon(x)$ is the permittivity, d_i is the total thickness of the AlGaN layer, d_d is the thickness of the cap layer, and E_F is the Fermi level with respect to the GaN layer conduction band [81-82]. Vth is the threshold voltage of the transistor and can be expressed by:

$$V_{th} = \phi_B - \Delta E_C - \frac{qN_s d_{AlGaN}^2}{2\varepsilon_{AlGaN}} - \sigma \frac{d_{AlGaN}}{\varepsilon_{AlGaN}} \qquad (4.15)$$

where ϕ_B is the metal-semiconductor effective schottky barrier height, ΔE_C is conduction band discontinuity at the interface, N_s is the doping concentration in n infused AlGaN layer, and σ is the overall net polarization charge density at the AlGaN/GaN interface [81-82]. The current-

voltage relationship in the HEMT with respect to 2DEG density, n_s, can be seen in equation 4.16 [81].

$$I_{dsat} = Z\mu q n_s(x)\frac{dV(x)}{dx} \tag{4.16}$$

where Z is the channel width and μ is the mobility of carriers [81]. The former equations are used to model the threshold and drain current magnitude. However, as seen in equations 4.14 and 4.15 the sheet carrier density is inversely proportional to threshold voltage. Then by further analysis, we see sheet carrier density is directly proportional to the drain current (eqn 4.16). This becomes problematic when developing a device model to match threshold and current magnitude to a specific range. To overcome this, John Albrecht's mobility equations (eqn 4.17), are used to model low-field mobility as a function of doping and lattice temperature [83-84].

$$\frac{1}{\mu(N,T_L)} = a\left(\frac{N}{10^{17}cm^{-3}}\right)\left(\frac{T_L}{300K}\right)^{-1.5}\ln\left[1 + 3\left(\frac{T_L}{300K}\right)^2\left(\frac{N}{10^{17}cm^{-3}}\right)^{-\frac{2}{3}}\right]$$
$$+b\left(\frac{T_L}{300K}\right)^{1.5} + \frac{c}{exp\left(\frac{\Theta}{T_L}\right)-1} \tag{4.17}$$

where $\mu(N,T_L)$ is mobility as a function of lattice temperature and doping concentration. N is the total doping concentration, T_L is lattice temperature, Θ is a function of LO phonon scattering equal to $\frac{\hbar\omega_{LO}}{k_B}$, or $1065K$, and parameters a, b, and c are constant fitting parameters expressed in $Vs\ cm^{-2}$ [83-84]. By modifying these constants the mobility can be adjusted accordingly. This affects the drain current output magnitude, and the knee voltage without affecting threshold.

4.4.2 Modeling the charge concentration

CXCL9 (MIG) as referenced before, is positively correlated with transplant rejection and has been shown to have about net 20 charges per molecule at a pH concentration of 7.4 (the normal concentration of human blood) [53]. Assuming a disease concentration of 34nM, and considering the elementary charge to be $1.6 \times 10^{-19}C$, then we can calculate the number of charges per molecule in diseased states (eqn 4.19), and the total number of molecules by using Avogadro's number (eqn 4.18). The step by step process can be seen in the following series of equations:

$$(34 \times 10^{-9} \; mol) * (6.022 \times 10^{23} \; mol^{-1}) = 2.04748 \times 10^{16} \; \text{molecules} \qquad (4.18)$$

$$2.04748 \times 10^{16} \; \text{molecules} * 20 \; \text{charges per molecule} =$$

$$4.09496 \times 10^{17} \; \text{total charges present in a diseased state} \qquad (4.19)$$

Recombinant MIG is a complex protein consisting of about 103 amino acid residues with a predicted molecular mass of $11.7 - 12$ kDa [85-87]. Using solely the molecular mass, the number of charges per vial of sample solution used in experimentation (each vial contains 5µg/mL of sample) can be determined by first finding the molarity of the solution. Then, we can find the number of molecules in the sample size and associate a charge with each molecule independently. The following equations are used to determine the total number of charges per vial:

$$\frac{.000005g}{11700\frac{g}{mol}} = 427.35 \; pmol \qquad (4.20)$$

$$\frac{427.35 \; pmol}{.001L} = 427.35 \; nM \; \text{in a 5µg/mL sample of solution.} \qquad (4.21)$$

Then, solving again for the number of charges per mole we obtain:

$$(427.35 \times 10^{-9} mol) * (6.022 \times 10^{23} mol^{-1}) = 2.5735 \times 10^{17} \text{molecules} \qquad (4.22)$$

$$2.5735 \times 10^{17} \text{ molecules} * 20 \text{ charges} = 5.147 \times 10^{18} \text{ total charges} \qquad (4.23)$$

Given that .3mL samples are used during experiment, we obtain:

$$5.147 \times 10^{18} \text{charges}* \frac{1}{3} = 1.71567 \times 10^{18} \text{ total charges per experiment} \qquad (4.24)$$

Multiplying these total charges by +1e, we obtain:

$$(1.71567 \times 10^{18}) * (1.6 \times 10^{-19} C) = 0.274507 \, C \text{ of charge total.} \qquad (4.25)$$

In solid state physics, electron-volts (eV) are used to represent a unit of kinetic energy obtained by accelerating an isolated electron across a potential difference of 1 volt. Thus, 1eV is equivalent to 1 electric charge times one (1*e) Joules. Since one volt is equal to one Joule per Coulomb, then one Coulomb is equal to one Joule per volt. This would, in turn, allow for the solving of the equivalent voltage present in the sample by determining the amount of collective energy present in the sample. However, this is a complex calculation requiring need for accommodation of double-layer charge distribution, and careful measurement of the solution using sophisticated equipment. The derivation of the equivalent voltage in an electrolytic solution of MIG can be left for future work.

CHAPTER V

NUMERICAL MODELING AND SIMULATION

A numerical simulation is developed using the ATLAS tool from the SILVACO™ virtual

wafer fab (VWF) tools. An input deck is generated using DECKBUILD, solved through the

ATLAS routine, and visually plotted using TONYPLOT. The basis of this model is to develop

an AlGaN/GaN structure using the VWF tools to simulate output characteristics that are ideally

identical (or very close) to experimental clean device characteristics. First, the actual device

biosensor is tested for its clean device operations. This data is then collected and used to develop

a structure that exhibited similar results using the Analytical techniques derived in chapter 4.

Then, after a satisfactory model is created, using an assumed bias voltage of 120mV, two bias

voltages are applied to the gate to simulate the prepared device, and the device after protein

conjugation. Drain current is measured along with a variety of other impactful parameters to

determine the effect of detection on the device properties.

5.1 SILVACO™ software

SILVACO™ is a powerful simulation software that uses physics based simulations rather than

empirical modeling. Physics-based simulations can predict electrical characteristics based on the

nature of the material and the way that it is structured in conjunction with one another. Using

differential equations derived from Maxwell's laws it is possible to model the electrical

performance of the device in DC, AC or transient analysis [90]. SILVACO™ is a TCAD process

that provides simulations not only based on material processes, but also impact of different processing recipes / techniques as part of its VWF (virtual wafer fab). The tools in this suite include powerful editors and plotting software such as DECKBUILD, TONYPLOT, DEVEDIT, MASKVIEWS, and OPTIMIZER [90]. Three of the most widely used simulators are ATHENA, MOCASIM, and ATLAS.

ATHENA, often used in conjunction with ATLAS can allow for two-dimensional modeling of a process. This simulation framework allows engineers to simulate and optimize fab process techniques by predicting physical structures that result from processing steps [90]. The output from ATHENA is used as input for ATLAS, which predicts the electrical characteristics of the resulting device under user-specified bias conditions. By using these two powerful tools together, it is possible to determine the impact on device performance based on not only the nature of the materials being used, but also by the processing steps taken.

ATLAS is a two-dimensional, and/or three-dimensional device simulator. It can be used to predict the electrical behavior of a device based on the material used and its structure and provide useful information to help understand the behavior of the device as a whole, and the device at the quantum level [90]. It can be used as a standalone editor or in conjunction with various tools in the Virtual Wafer Fab toolset.

Using an ATLAS process is similar to using another compiler. It has its own syntax, structure, and sequence. Generally speaking, there are five groups of statements. Structurally speaking, it is best to execute these groups of statements in order to avoid runtime errors. Figure 5.1 demonstrates the various groups and corresponding statements that are required when using DECKBUILD.

Specifying the structure	Specifying materials within that previously established structure	Numerical Method selection	Solution	Analysis
MESH	MATERIAL	SOLVE METHOD	LOG	Extract
REGION	MODELS		SOLVE	TONYPLOT
ELECTRODES	MOBILITY		LOAD	
DOPING	OTHER PARAMETERS		SAVE OUT	
SUBSTRATE	CONTACT INTERFACE			

Figure 5.1 – Modules involved in created a structure in DECKBUILD [90]

A thorough understanding must be maintained when building a structure in ATLAS. Minute changes in certain parameters can have a very impactful effect on the outcome of the modeled device, and as any other programming language the syntax used in ATLAS is unique and very specific. Once all structures within the groups of figure 5.1 are satisfied, then a systematic approach is taken and each line is analyzed one at a time. The following figure (Figure 5.2) demonstrates a flowchart of the approach taken by SILVACO's ATLAS software [90].
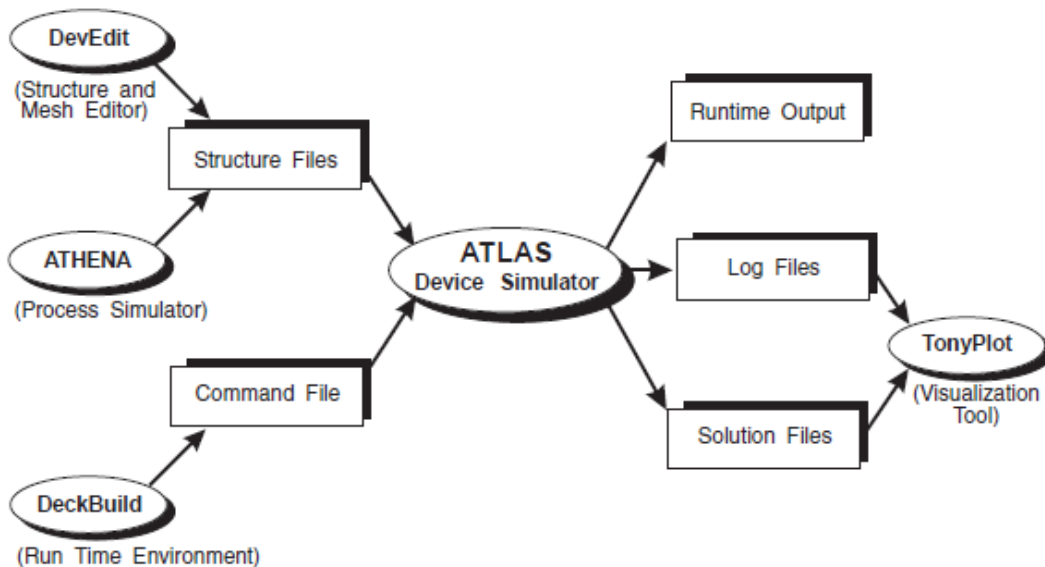
Figure 5.2 – SILVACO simulation flowchart

As mentioned beforehand, Deckbuild can be run as a standalone compiler, or can be run in parallel with ATHENA and DEVEDIT. For the purpose of this thesis, the compiler is run as a standalone since electrical characteristics and physical properties are desired, and there is no concern for process techniques taken to create the device.

5.2 Approach to developing a model

In order to develop an appropriate model to fit specific characteristics of the experimental device (such as threshold voltage, and drain current), a variety of factors need to be taken into account from the charge-control equations and the Albrecht low-field mobility equations (equations 4.14 - 4.17). An example model is first simulated through the SILVACO™ load example feature, to obtain the output characteristics of a basic AlGaN/GaN HEMT. Then the drain current and threshold voltage are adjusted by modifying various parameters in the charge control equation that are responsible for the increase/decrease of both threshold voltage and drain current. These parameters are mainly the low-field mobility, AlGaN barrier thickness, and Al mole fraction in the AlGaN alloy. The effects of doping and the addition of a 1 nm spacer layer between the AlGaN and GaN layers are also investigated. The material properties (i.e. saturation velocity, breakdown voltage, hole mobility,etc) are left to their default accepted values. A series of preliminary models are taken to compare and contrast the effect of changing various parameters in the Charge-Control equations and slowly molding the desired output characteristics for clean device operations. The nucleation layer is left as a constant across all models and the gate lengths are left constant at a conventional 2μm gate length. Table 5.1 shows various preliminary SILVACO™ models and their parameters, and table 5.2 shows output characteristics taken from those models.

Table 5.1 – Preliminary SILVACO models with various parameters

Model number	Substrate	Gate Length (μ)	AlN Spacer layer (nm)	AlGaN comp	AlGaN doping (cm^{-3})	AlGaN thickness (Å)	GaN thickness (μ)	AlN buffer layer thickness (Å)	AlGaN buffer layer thickness (Å)
1	SiC	2	---	0.25	---	250	1.5	150	250
2	SiC	2	---	0.30	---	250	1.5	150	250
3	SiC	2	---	0.35	---	250	1.5	150	250
4	SiC	2	1	0.25	---	240	1.499	150	250
5	SiC	2	---	0.25	1e15	250	1.5	150	250
6	Sapphire	2	---	0.25	---	250	1.5	150	250
7	Sapphire	2	---	0.25	1e10	250	1.5	150	250
8	Diamond	2	---	0.25	---	250	1.5	150	250

Table 5.2 – Output characteristics of various preliminary models

Model Number	Threshold Voltage (V)	Max drain Current at Vg=-3 (mA) VDS=4v	Quantum well depth (eV)	Polarization charge concentration C/cm^{-3}
1	-5	25 mA	.05	1.5
2	-6	30 mA	.055	1.8
3	-7	45 mA	.055	2.1
4	-10	90 mA	.07	4
5	-7	45 mA	.055	1.5
6	-5	25 mA	.053	1.5
7	-7	55 mA	.055	1.5
8	-5	30 mA	.053	1.57

Model 1 in the tables can be taken as a reference figure to which the rest can be compared. As can be seen from the tables, barrier thickness, composition, and doping all play a substantial role in the modulation of the drain current and threshold voltage. Also, as expected, threshold voltage and drain current share an inverse relationship. The effects of doping and the addition of the spacer layer produce drastic changes in drain current and threshold voltage, so these parameters are neglected in future modeling. In order to simplify the effects of the net neutrality equation

emphasis is placed on the development of an intrinsic device. Furthermore, comparing the

diamond substrate (model 8) with SiC (model 1), and Sapphire (model 6) it can be seen that

diamond is theoretically the optimal substrate for maximum output characteristics. However, in

practice this is infeasible due to the very high cost. A figure depicting a basic analysis of the

previous data can be seen in table 5.3.

Table 5.3 – Breakdown of parameter effects on threshold voltage and drain current

Parameter Changed	Adjustment	Effect on Threshold (in signed magnitude)	Effect on Drain Current
Interface charge	higher	↓	↑
Interface charge	Lower	↑	↓
Barrier thickness	Greater	↓	↑
Barrier thickness	Lesser	↑	↓
AlGaN composition	Greater	↓	↑
AlGaN composition	Lesser	↑	↓
Work function	Higher	↑	↓
Work function	Lower	↓	↑
An.albrct	Higher	-----	↓
An.albrct	Lower	-----	↑
Bn.albrct	Higher	-----	↓
Bn.albrct	Lower	-----	↑
Cn.albrct	Higher	-----	↓
Cn.albrct	lower	-----	↑

In this table, An.albrct, Bn.albrct, and Cn.albrct are the three fitting parameters from Albrecht's

low-field mobility equations. They can be modeled accordingly to adjust the magnitude of the

drain current without having any effect in threshold voltage. The results from these simulations

show conclusions of various parameters that are in good agreement with that of which is

generally accepted. With these effects taken into consideration a model is carefully and precisely

developed.

5.3 Modeling and simulation of Final model

A two-dimensional device is constructed in DECKBUILD consisting of a 180 Å undoped Al_xGaN_{1-x} barrier with a molar composition of x=0.18 grown on a 1.507µm GaN layer. A 400 Å nucleation layer consisting of a 150 Å AlN layer and a 250 Å AlGaN layer is included between the bulk GaN and the substrate, which consists of a 2 µm thick SiC substrate. The nucleation layer is added to help ease the mismatch between the bulk GaN layer and the SiC layer. The gate length is 2 µm. A visualization of this device can be seen in figure 5.3.
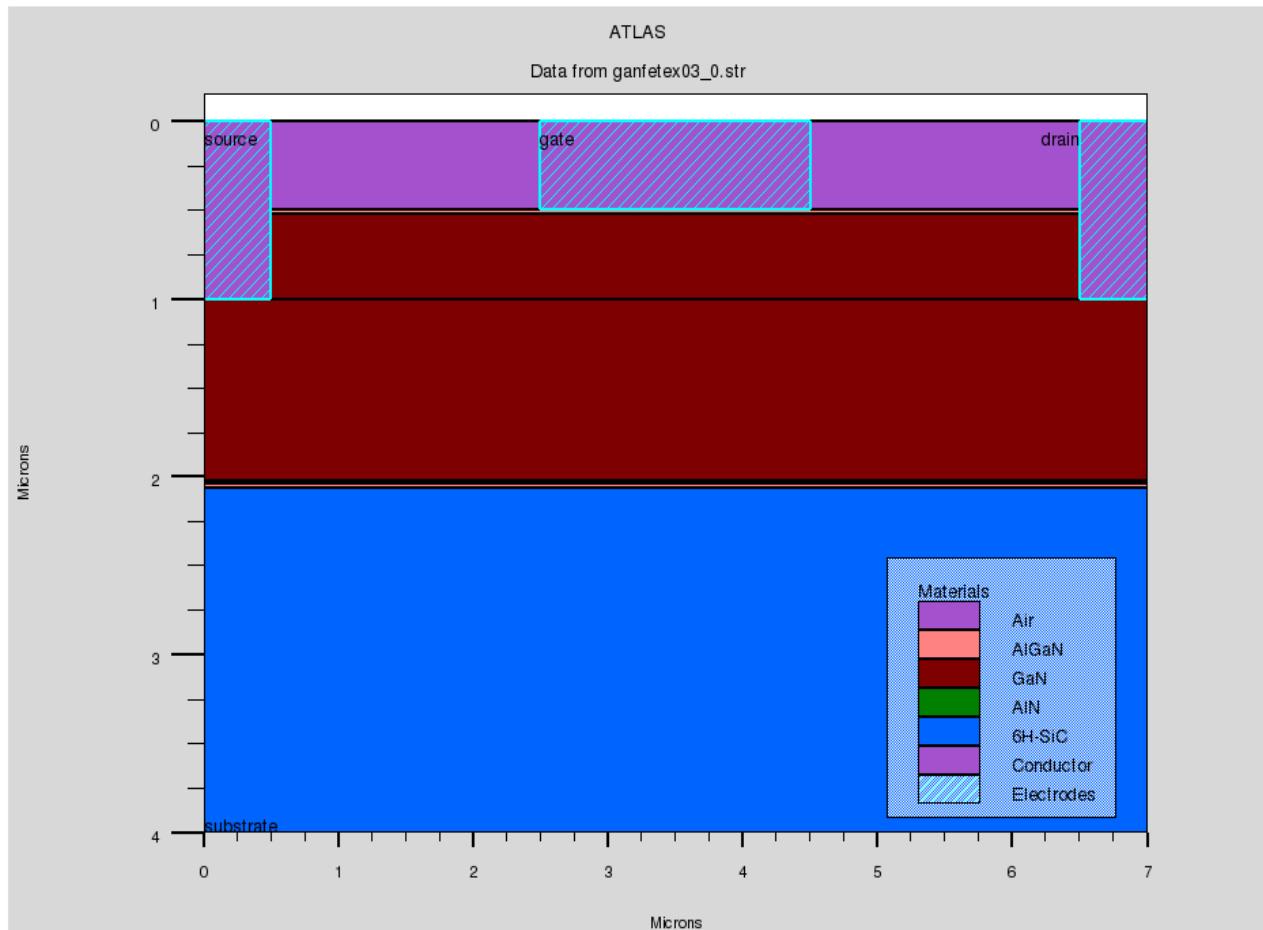
Figure 5.3 – Modeled device using SILVACO

The model in figure 5.3 is considered the final biosensor model. The corresponding band

diagram taken from a cutline taken at the metal/AlGaN/GaN interface can be seen in figure 5.4.
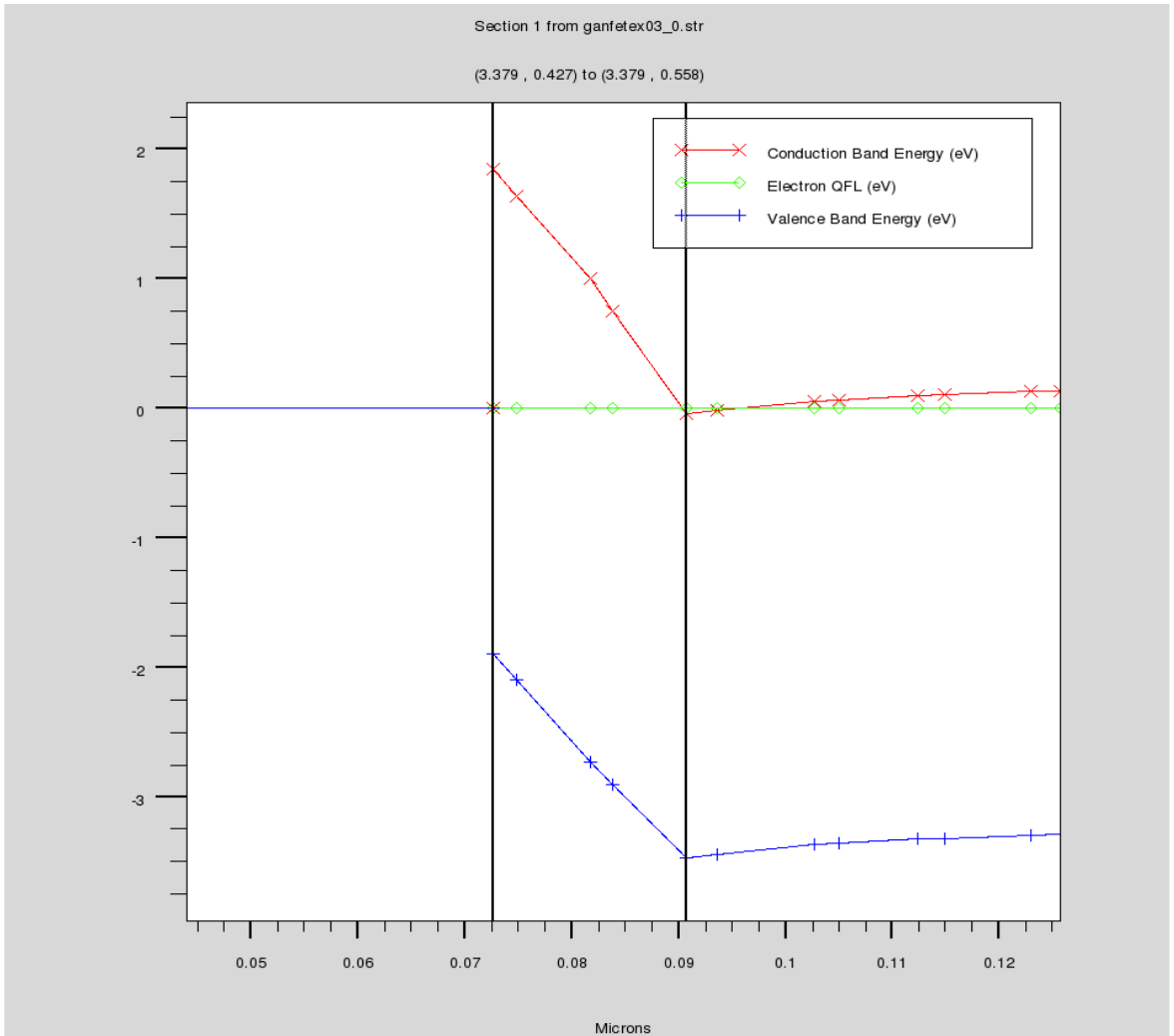
Figure 5.4 – Band diagram of HEMT model taken at the interface

As can be seen in figure 5.4, the quantum well is formed at the AlGaN/GaN cutline interface.

This is where the 2DEG is accumulated. A comparison of simulated threshold voltage vs

Experimental threshold voltage can be seen in figure 5.5, and the simulated output characteristic

curves can be seen in figure 5.6 and figure 5.7.

73
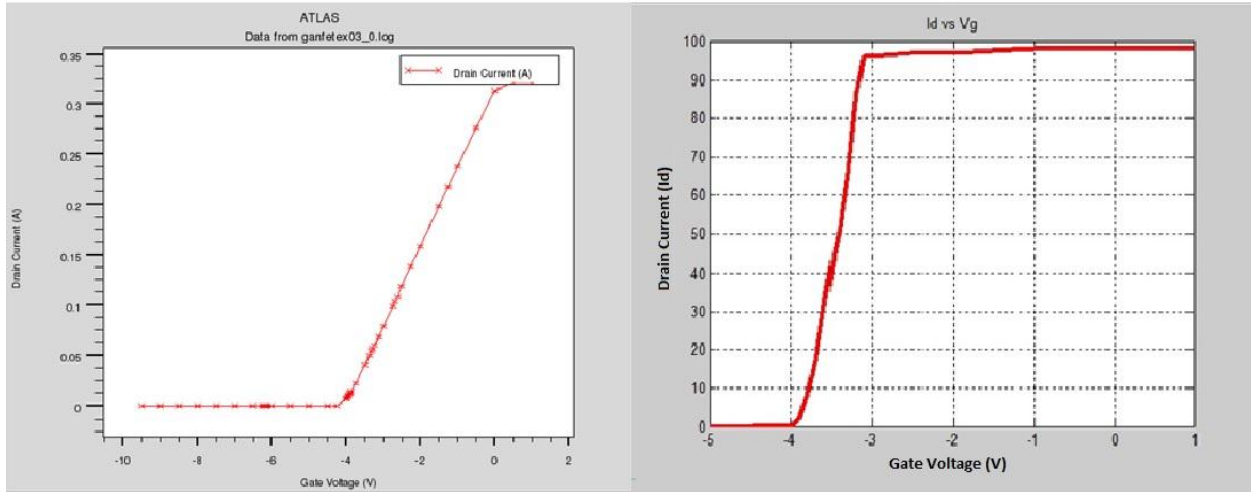
Figure 5.5 – Simulated vs Experimental threshold voltage
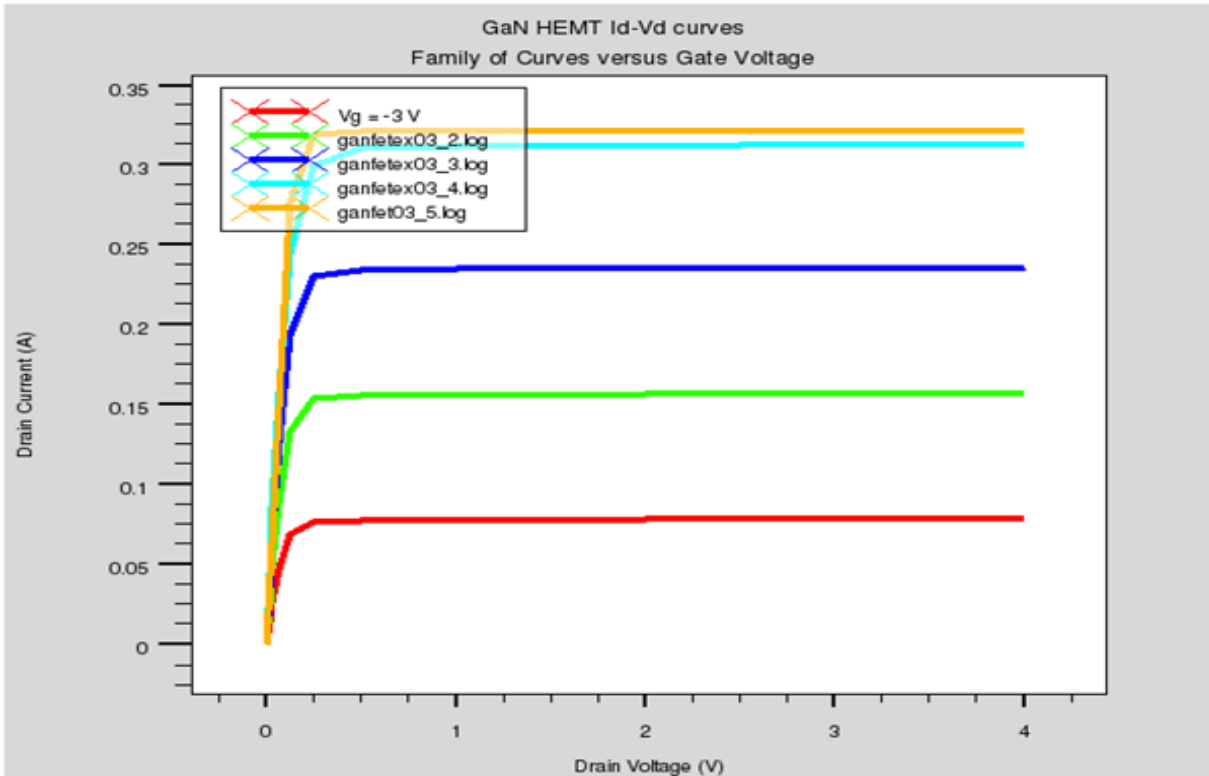
Figure 5.6 – Simulated output characteristic curves

In figure 5.6, the gate is swept from Vg=-3v to Vg=0v. In this model it is safe to assume floating

gate is analogous to a zero volt potential because the two exhibit matching experimental output

characteristics, and we expect the ambient environment to provide (if any) a negligible amount

of electric potential.
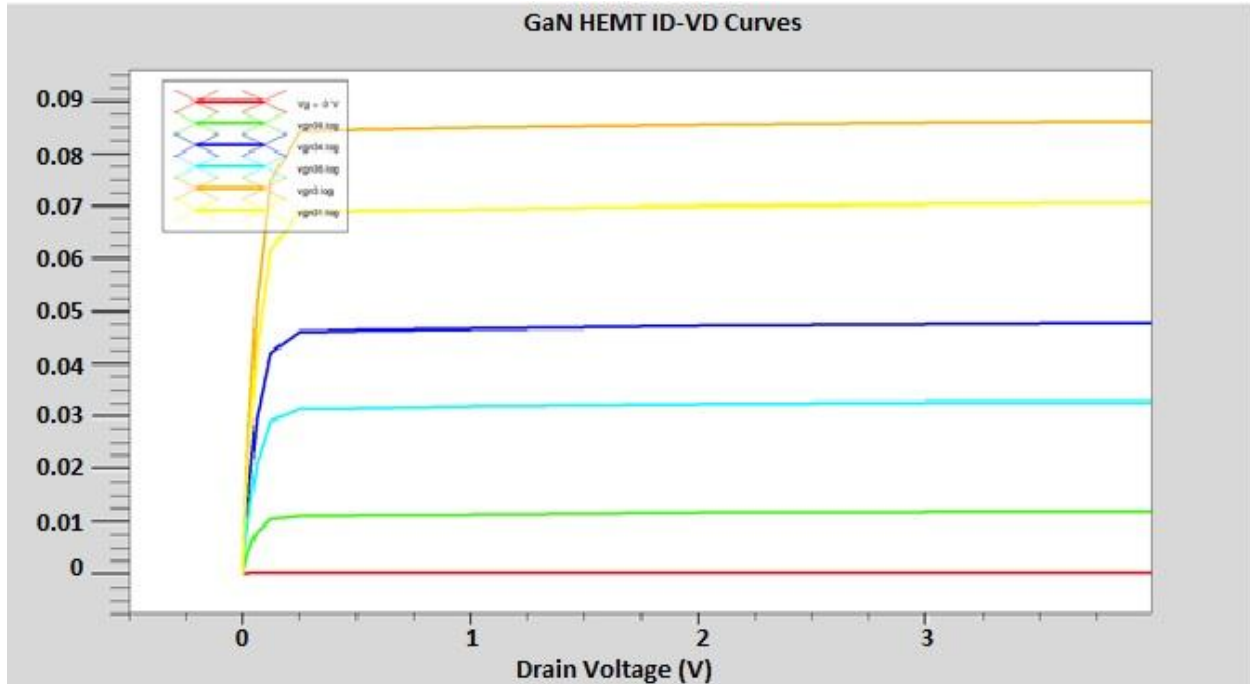
Figure 5.7 – Output characteristics taken at the Threshold area (Vg=-4 to Vg=-3)

The characteristic device parameters associated with the developed clean device model can be

seen in table 5.4.

Table 5.4 – Modeled intrinsic device parameters taken at the interface

Parameter	Value
Charge concentration (C/cm3)	0.75
Cond. Current Density (A/cm2)	6.5e8
Quantum well depth (eV)	0.04
Electric Field (V/cm)	9e5
Polarization charge (C/cm3)	0.75
Potential (V)	1.9
Mobility (x) (cm2/V-S)	920000

The values are obtained using the cutline tool in Silvaco and are taken as the intrinsic values for

the device. They also serve as the reference values for which simulated operating and sensing

performance parameters are compared. Using this final intrinsic model, various sweeps are

performed to determine the effect of changing the Alloy composition, and AlGaN barrier

thickness. These observations are plotted in figures 5.8, 5.9, and 5.10.
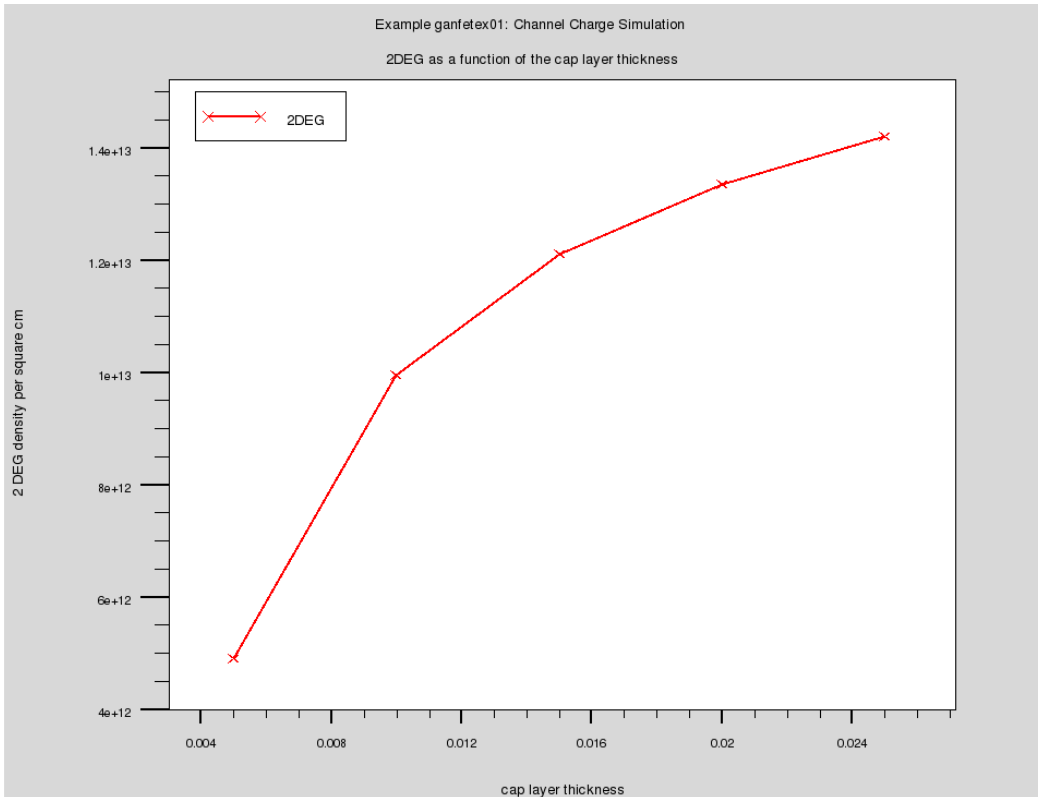
Figure 5.8 – 2DEG as a function of AlGaN barrier layer thickness
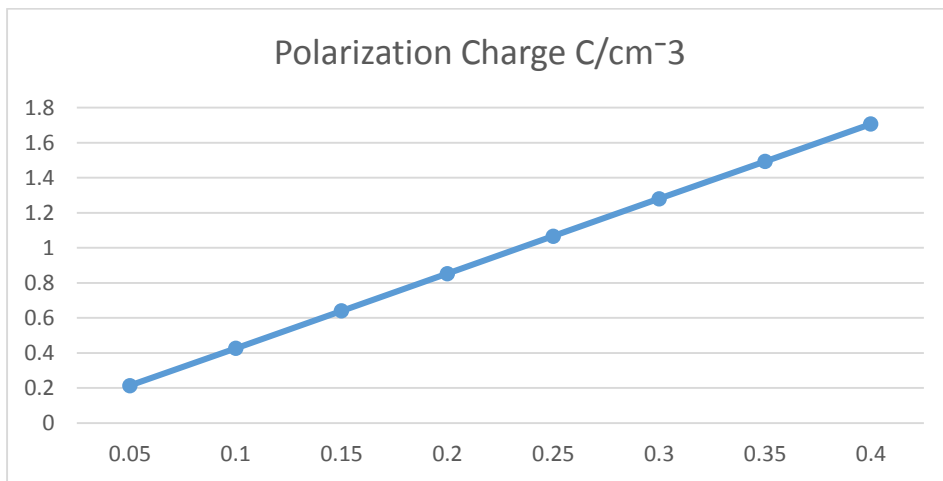
Figure 5.9 - Polarization charge versus Al alloy composition
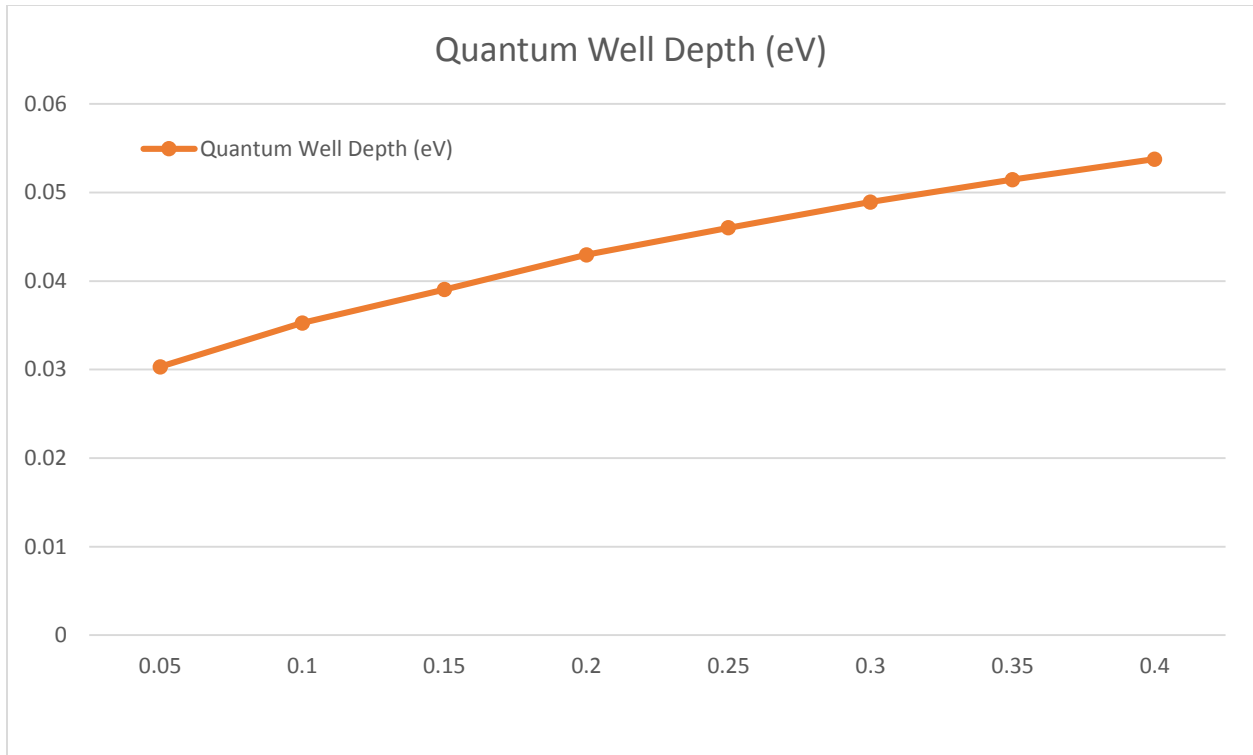
Figure 5.10 – Quantum well depth vs alloy composition

As predicted, the alloy composition and AlGaN barrier thickness play a substantial role on the output characteristics and polarizations of the device. This is because as the composition of the AlGaN increases, the lattice constant, a, decreases [91]. Based on the theory derived in Chapter 2, this shrinking in lattice constant results in a greater strain on the AlGaN crystal when it is grown on top of GaN. This increase in strain causes the piezoelectric polarization to increase and cause an increase in 2DEG density [91]. This is further justified by the results taken from SILVACO in table 5.2. This creates the notion that experimentally it is possible to create a device with targeted characteristics, however the use of very sophisticated equipment and growth techniques would likely need to be exercised.

5.4 Bio-detection Simulation and Analysis

Upon derivation of an appropriate model, an assumed bias voltage of 120mV is applied to a floating gate curve generated in SILVACO™ to simulate the effect of capacitive coupling effects due to the creation of the SAM layer (metal-electrolyte double layer), and the effect of bioconjugation. The simulation is performed multiple times to verify consistency. The results of one sweep can be seen in figures 5.11, 5.12 and 5.13 at different intervals of VDS.
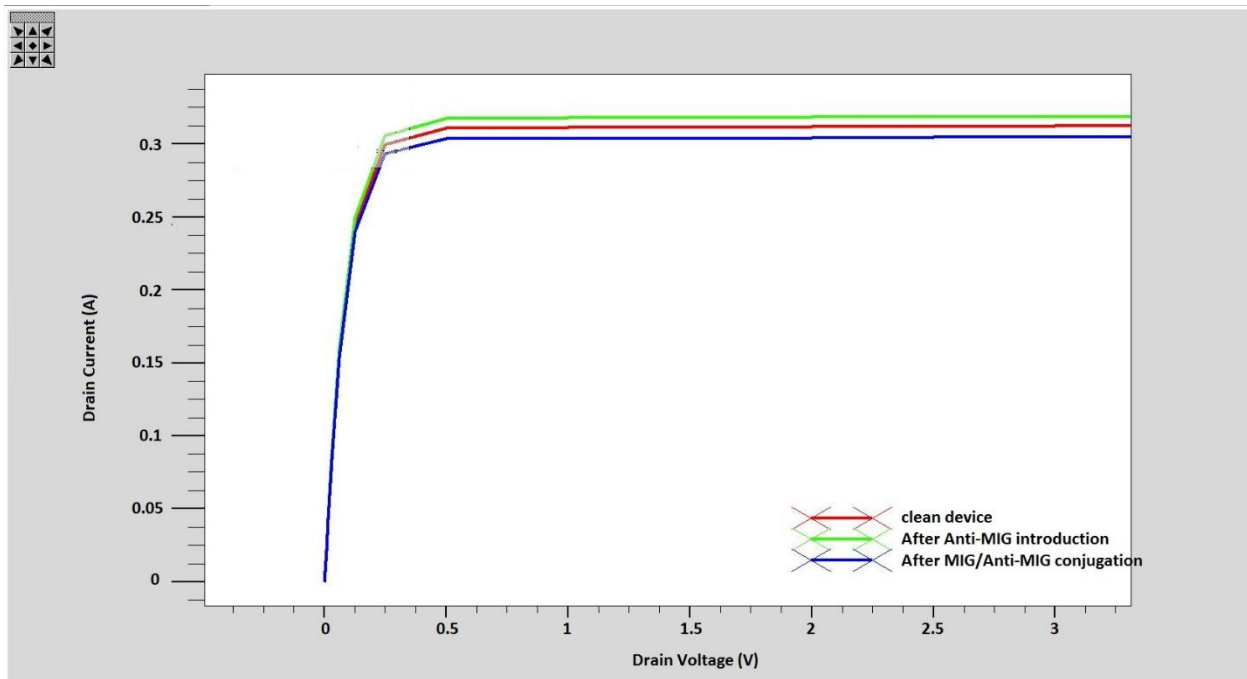
Figure 5.11-Simulated working biosensor
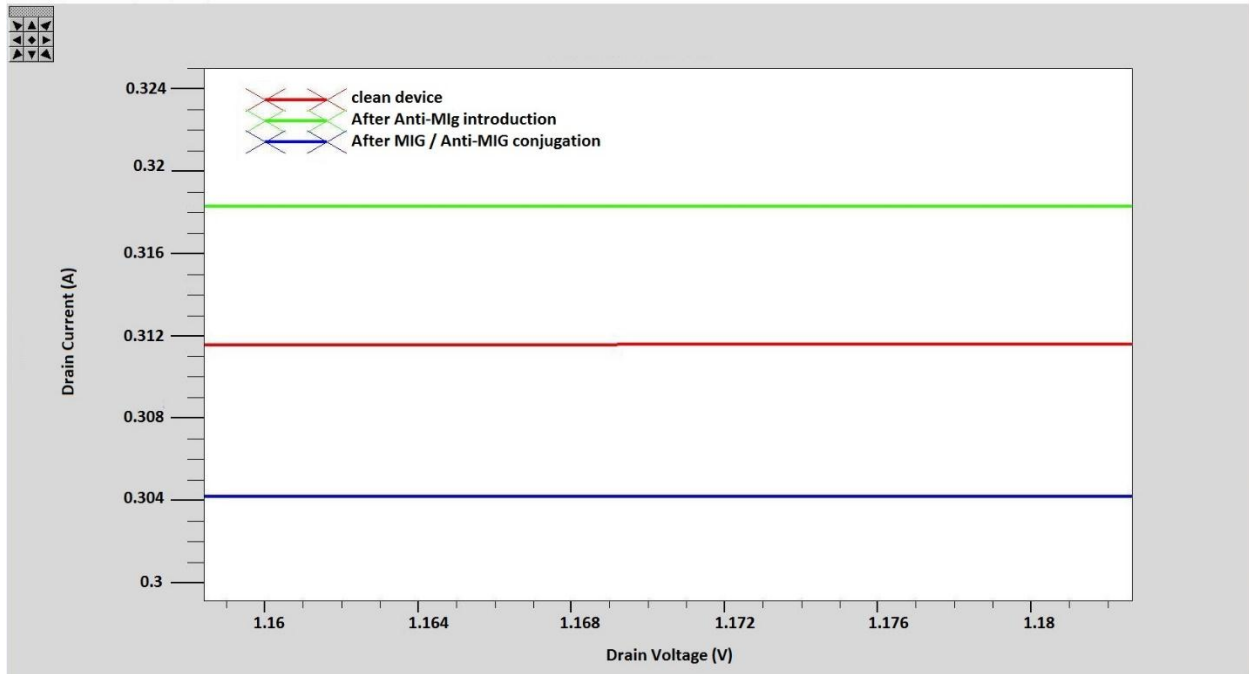
Figure 5.12- Simulated working biosensor zoomed in at VDS=1.16
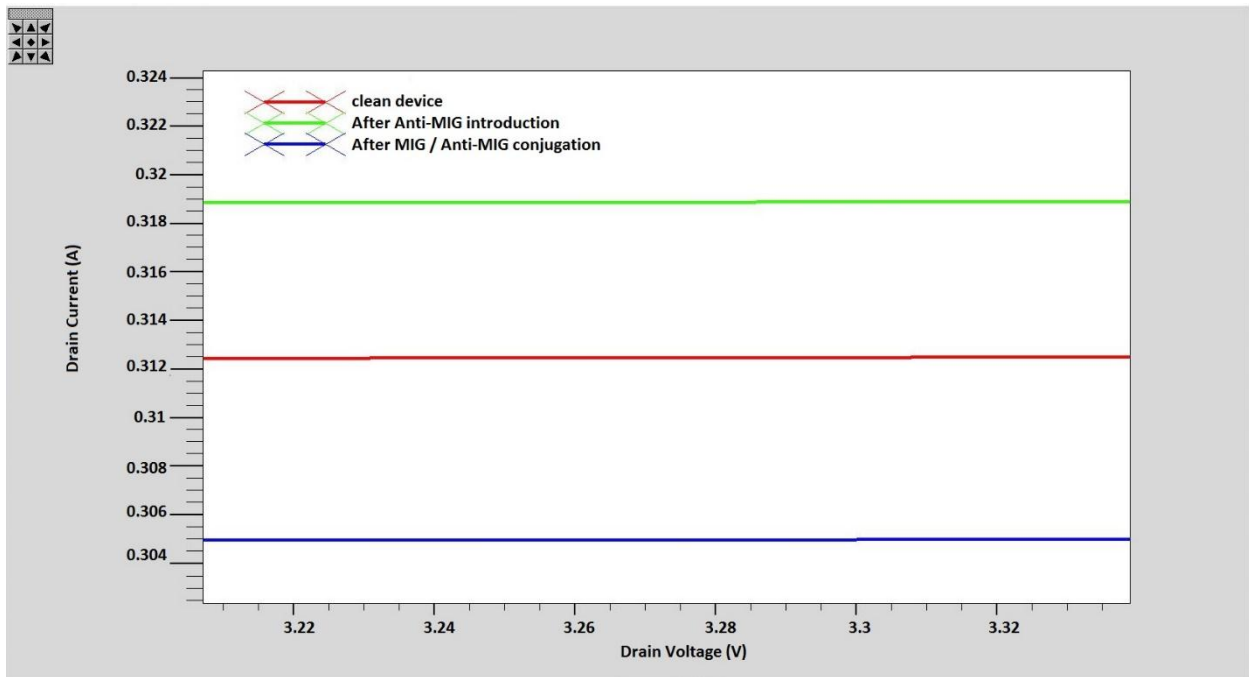
Figure 5.13 – Simulated working biosensor zoomed in at higher VDS

As can be seen in figure 5.7, the device should reach saturation at between about 0.2 and 0.4

volts, which is also demonstrated in figure 5.11. The simulated biosensor is first simulated with

an application of 0 volts to simulate the clean device. Then the DC bias of 120mV is applied to

obtain the Anti-MIG (SAM layer) curve. Finally, assuming a realistic conjugation rate of about

86.7%, a third DC bias is applied that is an 86.7% multiple of the bias voltage multiplied by -1.

This is because we know that Anti-MIG and MIG are equal and opposite in magnitude due to the

fact that upon introduction they completely neutralize each other, so they should, in theory, have

negative sign values. In figure 5.12, at $VDS \cong 1.2V$ we see a change of 6mA between the clean

device and the device after the inclusion of the SAM layer, and an absolute change of 14mA

between after simulation of bio-conjugation. Figure 5.13, is taken at a $VDS \cong 3.15V$ and

demonstrates a change of 7mA between clean device and simulation of the SAM layer, and an

absolute change of 14mA after simulation of bio-conjugation. The conclusion drawn from this

simulation is that as VDS becomes larger, the drain current becomes theoretically more stable as

it reaches steady state. This steadies the effect of the capacitive-coupled applied DC bias

voltages, and undoubtedly has a noticeable effect. Multiple simulations performed with the same

device under the same conditions repeated similar outcomes with deviations of about $\pm 20\mu A$.

Table 5.5 shows the various device physical characteristics gathered from the device at each step

of its operation, as well as the expected behavior on different substrates. Detailed graphs

corresponding to this data can be found in Appendix C.

Table 5.5 – Physical characteristics of simulated biosensor taken at interface

Mode	Parameter	SiC	Sapphire	Diamond
Operating/Floating	Charge concentration (C/cm3)	0.82514	0.8259	0.82697
Operating/Floating	Cond. Current Density (A/cm2)	2.9065e7	2.9066e7	2.9069e7
Operating/Floating	Electric Field (V/cm)	1.0228e6	1.0234e6	1.024e6
Operating/Floating	Polarization charge (C/cm3)	0.768	0.768	0.768
Operating/Floating	Potential (V)	2.0364	1.9085	1.9105
Operating/Floating	Mobility (x) (cm2/V-S)	21886	21717	21444
Operating/Floating	Drain Current (A)	0.3116	0.3122	0.31195
Operating/Floating	Quantum well depth (eV)	0.0405	0.0404	0.0405
Operating/Floating	Schottky barrier height (eV)	1.8431	1.8431	1.843
Anti-MIG	Charge concentration (C/cm3)	0.79397	0.79516	0.8555
Anti-MIG	Cond. Current Density (A/cm2)	2.9663e7	2.9677e7	2.8507e7
Anti-MIG	Electric Field (V/cm)	9.804e5	9.7944e5	1.0629e6
Anti-MIG	Polarization charge (C/cm3)	0.768	0.768	0.768
Anti-MIG	Potential (V)	2.0812	1.9502	1.8897
Anti-MIG	Mobility (x) (cm2/V-S)	21355	21216	21809
Anti-MIG	Drain Current (A)	0.31825	0.31824	0.3183
Anti-MIG	Quantum well depth (eV)	0.04	0.04	0.04
Anti-MIG	Schottky barrier height (eV)	1.7231	1.7231	1.9331
MIG	Charge concentration (C/cm3)	0.86032	0.85923	0.85167
MIG	Cond. Current Density (A/cm2)	2.841e7	2.8404e7	2.8512e7
MIG	Electric Field (V/cm)	1.0697e6	1.066e6	1.0594e6
MIG	Polarization charge (C/cm3)	0.768	0.768	0.768
MIG	Potential (V)	2.0163	1.8795	1.8803
MIG	Mobility (x) (cm2/V-S)	21923	22173	22585
MIG	Drain Current (A)	0.3044	0.30416	0.3059
MIG	Quantum well depth (eV)	0.04	0.039	0.04
MIG	Schottky barrier height (eV)	1.9481	1.9481	1.9331

From this data it can be seen that the polarizations remain constant at the interface regardless of process step, and substrate used. This is an important conclusion and is a result of lattice mismatching between the AlGaN/GaN layers and simulations show that it is independent of other factors. Also, as expected, changes in charge concentration are observed as the DC bias for the chemically modified, and MIG simulations are applied. These are indicators that the 2DEG

sheet carrier density has been modulated and appropriately results in changes in steady state

drain current (Figure 5.14). It is also worth mentioning that in these simulations the Schottky

barrier height is slightly fluctuated across all substrates and all operations (floating, SAM layer,

and after conjugation). Although, the work function was kept constant in these simulations, it can

be seen that drain currents results in fluctuations in Schottky barrier height. The effects presented

in this data are performed under the assumption of ideal conditions. Parameters reflect changes

as a result of capacitive DC coupling, and do not reflect surface reaction changes at the gate

electrode which certainly do exist. In practice, as seen in chapter 4 the work function is expected

to change as the surface of the electrode of the device undergoes a chemical and/or physical

reaction resulting in changes in the Schottky barrier height and surface states.

Drain Current and Detection For Simulated Biosensor vs Sapphire and Diamond

	SiC	Sapphire	Diamond
Floating	0.3116	0.3122	0.31195
Sam Layer	0.31825	0.31824	0.3183
After Conjugation	0.3044	0.30416	0.3059
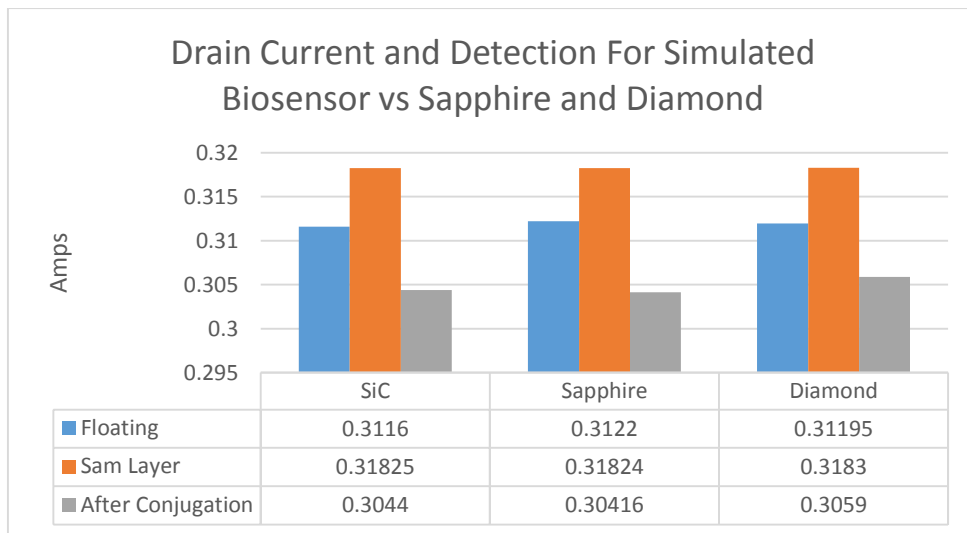
Figure 5.14 – Drain current and detection for simulated biosensor versus substrate

As can be seen in figure 5.14, the modeled biosensor with SiC and diamond substrates exhibit

similar expected results, with SiC showing optimal performance. Sapphire, however exhibits a

slightly weaker effect. Further investigation into this anomaly can be a possible standalone topic

with experimental results needed before any conclusions can be made. As of now, this is thought

to do to large lattice mismatching between Sapphire and the bulk GaN causing a non-negligible effect. A graph depicting lattice constants vs material can be seen in figure 5.15.
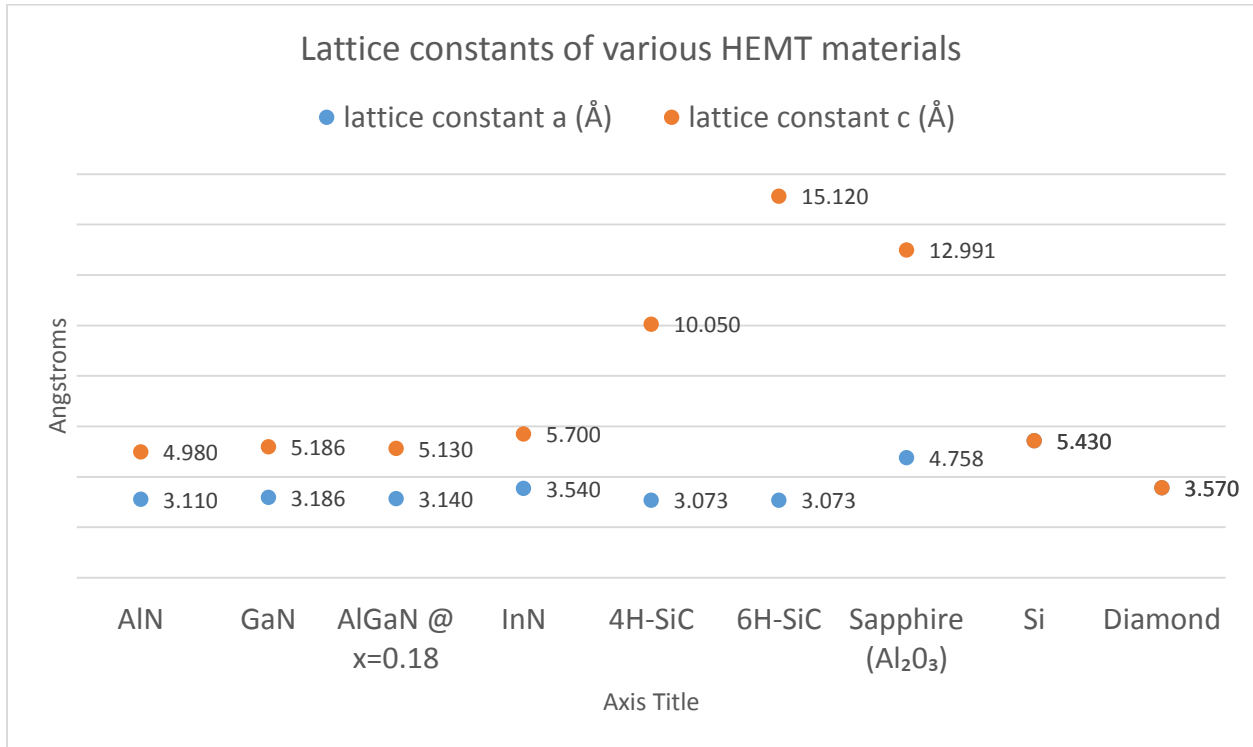
Figure 5.15 – Lattice constants of different materials used in HEMT devices [91-99]

This large substrate mismatching doesn't completely rule out Sapphire as a suitable substrate for AlGaN/GaN HEMT biosensor applications, but simulations suggest using Sapphire as a substrate to detect Human MIG may not be optimal. According to Ibbetson et al. (2000) in order to truly ignore the effects of substrate into the charge neutrality equation, it is inferred that that in a truly undoped HEMT device that the net polarization induced by the substrate (along with other polarizations) is negligible. This leads to the assumption that the Fermi level is located near the conduction band edge [61]. However as seen in figure 5.16, there exists a shifting in Fermi level energy as well as a larger gap between the conduction band and the Fermi level as compared to the favorable SiC, and diamond. This leads to the previous assumptions, while still technically

sound, to be less applicable. Furthermore, in the numerical simulations sapphire exhibits greater fluctuations in Electric field at various operating modes than SiC and diamond. This could play a substantial role as well. A table depicting full cutline parameters extracted at the bulk GaN/nucleationlayer/substrate interface can be seen in table 5.6. The observations about most optimal substrate in this application, as mentioned before, are basis for a possible standalone topic and further experimental testing is required to determine if the two-dimensional simulations hold true.
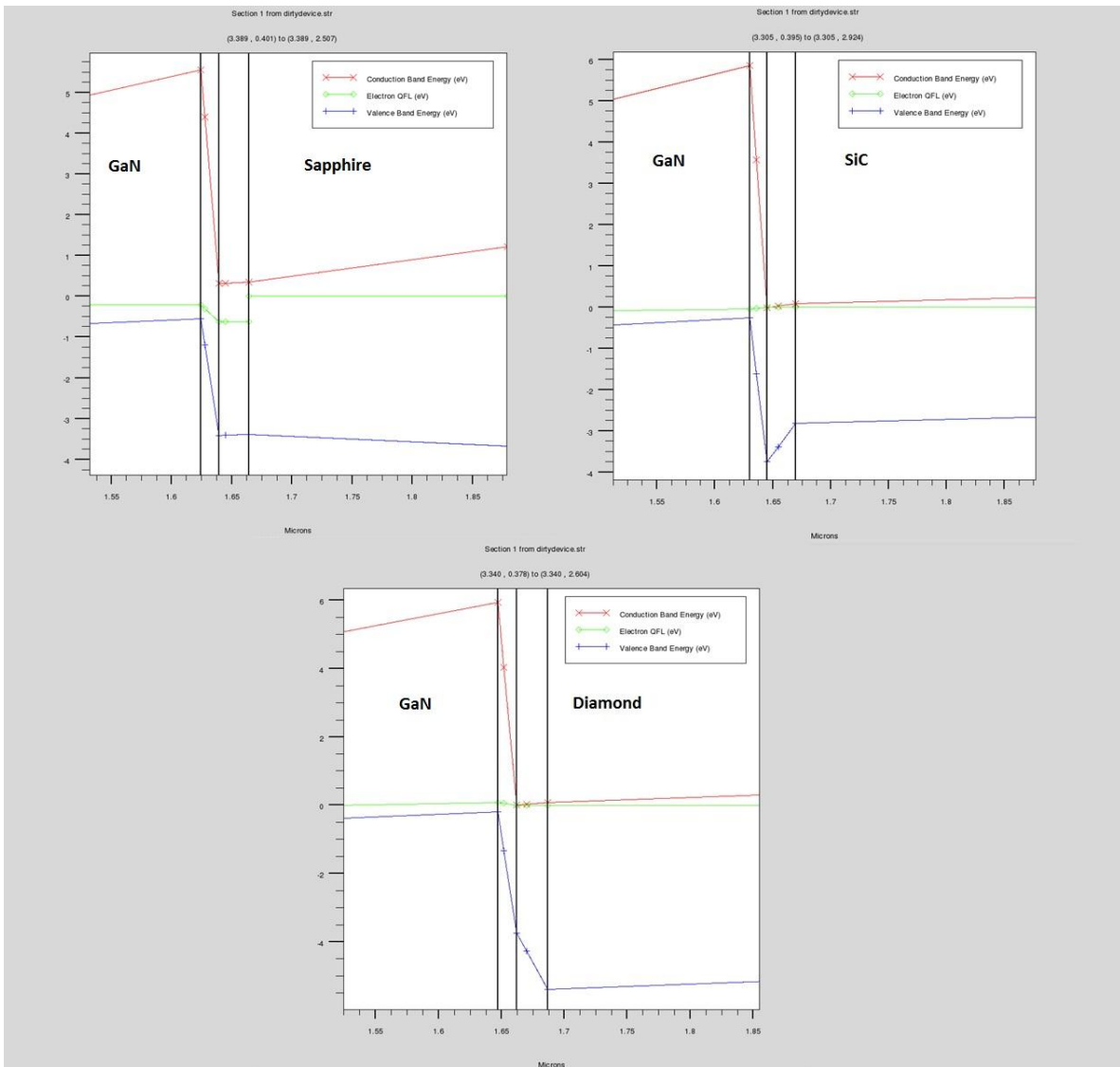
Figure 5.16 – Band diagrams of SiC, Sapphire, and diamond at bulk/substrate junction.

84

Table 5.6 – Physical characteristics of simulated biosensor taken at bulk/substrate

Mode	Parameter	SiC	Sapphire	Diamond
Intrinsic	Charge concentration (C/cm3)	-0.004385	0	-0.015242
Intrinsic	Electric Field (V/cm)	7067	5995	14551
Intrinsic	Polarization charge (C/cm3)	0.0355	0	.03553
Operating/Floating	Charge concentration (C/cm3)	-0.0042	0	-0.015568
Operating/Floating	Electric Field (V/cm)	13348	8100	14617
Operating/Floating	Polarization charge (C/cm3)	0.0355	0	0.03553
Operating/Floating	Knee Voltage (V)	0.25	0.25	0.25
Anti-MIG	Charge concentration (C/cm3)	-0.004335	0	-0.015856
Anti-MIG	Electric Field (V/cm)	5775	1508	13603
Anti-MIG	Polarization charge (C/cm3)	0.0355	0	0.03553
MIG	Charge concentration (C/cm3)	-0.004389	0	-0.015569
MIG	Electric Field (V/cm)	7040	4244	14617
MIG	Polarization charge (C/cm3)	0.0355	0	0.03553

Corresponding graphs for each of the parameters in this table can be found in Appendix D.

While the model developed in this chapter is far from complete, it serves as a rough basis for understanding the mode of action of an AlGaN/GaN HEMT based biosensor and through empirical and theoretical data/modeling, validates the theory developed in this chapter with two-dimensional numerical simulations.

CHAPTER VI

EXPERIMENTAL DATA AND ANALYSIS

In this chapter experimental procedure is performed to test the theories previously

developed in chapters 4 and 5. The biosensor was tested several times to determine if the results

were consistent. Other concerns such as repeatability, device packaging, and effect on device

characteristics are also discussed in this chapter. Detailed scanning electron microscopy (SEM)

images are also provided in this chapter to further support the claim that the SAM layer exists

and is chemically bonded to the device.

6.1 Experimental Procedure

6.1.1 Clean device characteristics

Before any chemical modifications are conducted, a collection of uncharged intrinsic

device characteristics are taken by means of DC circuit analysis, and a DC probe station in

conjunction with a dual channel high speed source monitor working with IC-CAP software Both

approaches are utilized to ensure proper clean device operation and consistent characteristics.

The significance of this step is to provide a reliable, experimental reference from which any

absolute changes in output characteristics can be compared. Figures 6.1 and 6.2 represent output

characteristics taken from a built circuit, and a DC probe station respectively. Figure 6.3

represents the configuration used when extracting parameters with the DC probe station.
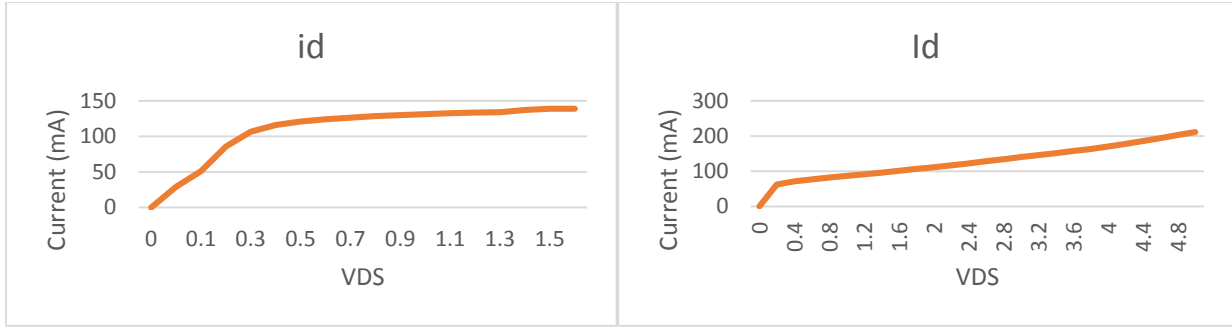
Figure 6.1 – ID vs VDS at Vg=-3.1 for two clean devices of the same type. Current is given in millamps and voltage is given in volts
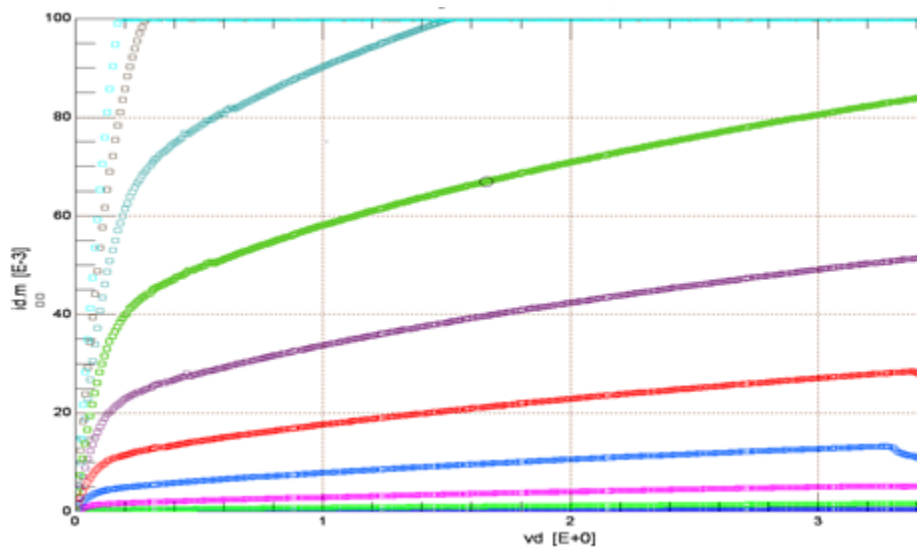
Figure 6.2 – ID vs VDS at varied gate voltage around the threshold area (-4 to -3). Vg=-3.1 is represented by the second graph down from the top (green)
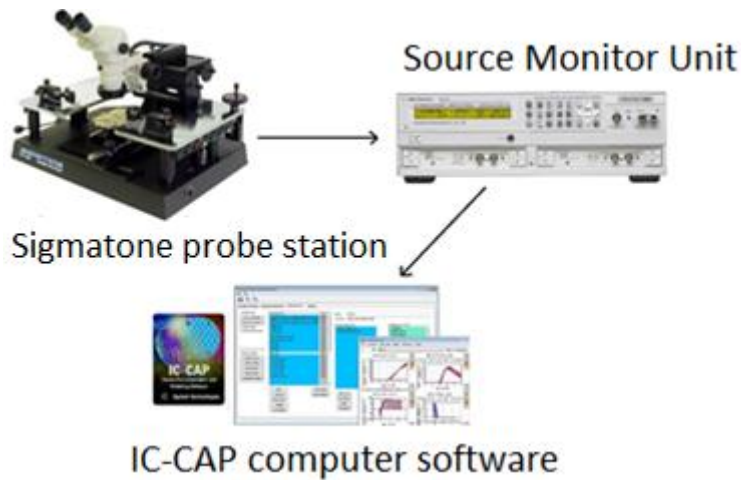
Figure 6.3 – Flow chart demonstrating device parameter extraction

In figure 6.1, the current is given in milliamps as the device is measured at vg=-3.1 volts to verify results that are consistent with the extracted probe station results in figure 6.2. The circuit consisted of a 50 ohm resistor at the drain with a power supply sweep of 0 to 32 volts. Obvious current collapse is observed in DC probe station results. After some investigation the cause is found to be due to weak connections from the power supply to the DC probe station probe tips causing the probe station to generate pulsed DC signals and random AC components. Current collapse phenomena is beyond the scope of this thesis, but it is a greatly researched topic and known to occur in AlGaN/GaN HEMT devices under pulsed and AC conditions, and is attributed to surface traps [24][57-59]. It is worth noting, however, that the knee voltages of approximately 0.2V to 0.4V remain consistent across the various methods. A combination of characteristics from these three graphs were used to create the modeled device in chapter 5 (figure 5.3). Similarly, the device threshold was extracted using the same built circuit above but with a 10 volt fixed power supply and a fixed resistance of 100 ohms. Figure 6.4, shows the modeled threshold voltage as taken from the actual device.
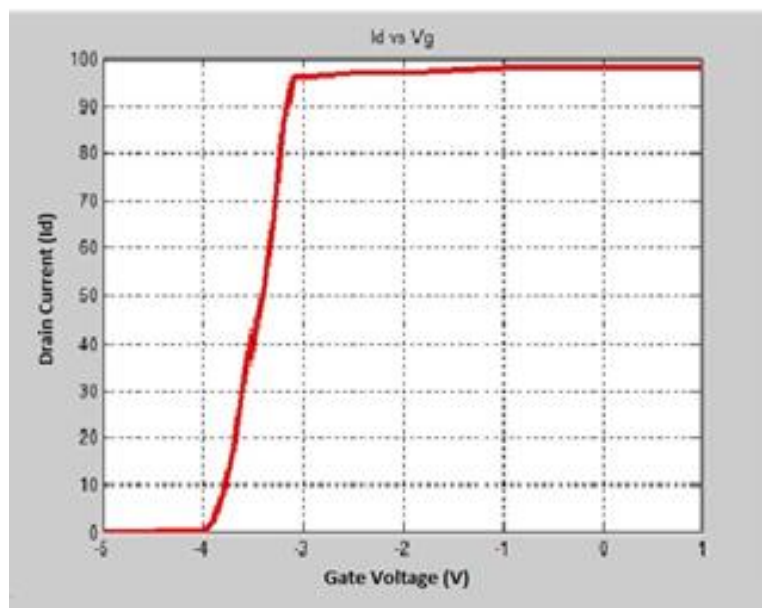
Figure 6.4 – Threshold voltage taken from clean device

6.1.2 SAM layer preparation

After extraction of clean device characteristics are obtained, a chemical procedure is practiced that follows the methodology developed in Chapter 3. A simple circuit is constructed to fix the amount of drain current flowing through the device. A figure depicting the circuit can be seen in Figure 6.5.
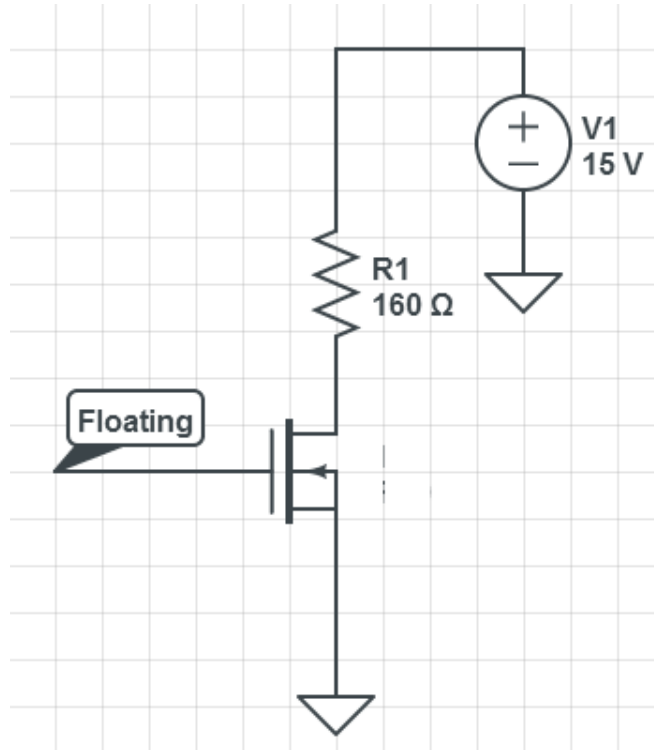
Figure 6.5 – Schematic of proposed biosensor

Clean device floating gate drain current for depletion mode AlGaN/GaN HEMT is reported as 92.64 mA. This current is taken as a reference from which the changes are compared.

The first step in the chemical process is to prepare physiological conditions that closely mimic the environment in the human body to allow the proteins to thrive. For human blood, pH is typically in the slightly basic range of 7.35 to 7.45 [100]. This environment that exhibits similar pH to human body conditions is created using a 0.1M phosphate buffer solution (PBS). A

pH meter verifies a pH of 7.44 upon dissolution of 1.826g of PBS in about 10 mL of de-ionized water.

Next, 5mg of crosslinker, DSP, is dissolved in 1mL of Dimethyl Sulfoxide (DMSO), an organic solvent. DMSO is used because DSP is water insoluble. Acetone may also be safely used to create an aqueous solution with DSP. The aqueous solution created by dissolution of DSP in DMSO is used to coat the surface of the gate electrode. The electrode is left to incubate at room temperature for 18 minutes.

After 18 minutes of incubation, the surface is rinsed with PBS to remove any unbinded DSP. The surface is then immediately treated with 0.3mL of target antibody (Anti-MIG) harbored in 0.1mL of the previously prepared PBS environment. This solution is then slowly applied to the gate and allowed to incubate for an additional two and a half hours. This step needs to be performed immediately after the 18 minute incubation period of DSP to ensure proper protein coupling [53]. If the former isn't done appropriately then the NHS reactive groups will hydrolyze, ultimately resulting in negligible protein coupling [53].

Upon completion of the former step, the SAM layer is now formed. Two separate experiments demonstrate consistent increases in drain current. The magnitude for the absolute increases in drain current are reported to be between 80μA – 90μA and is a successful indication that the surface states of the device are modulated by the chain of events described in chapter 4 and are therefore influencing the sheet carrier density at the interface. Images depicting the SAM layer are taken using scanning electron microscopy (SEM) and investigate the clean surface of the device versus the chemically modified surface. The results obtained from this imaging inherently validates the existence of the SAM layer as a clear modification of the surface. The

depictions in figure 6.6, and figure 6.7 can be compared to the theoretical depiction derived in

Chapter 3 (Figure 3.4).
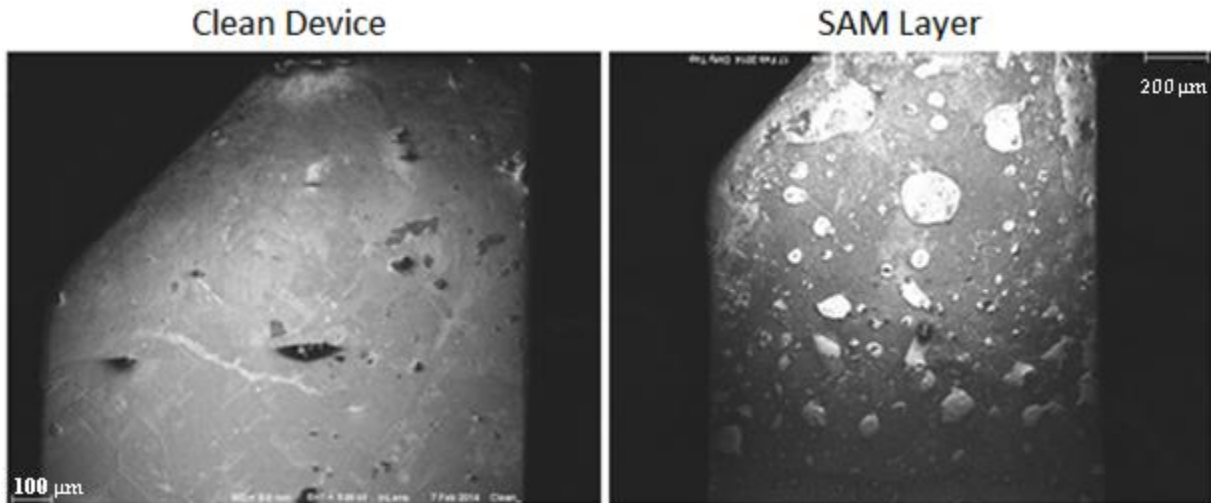
Figure 6.6 – SEM imaging of clean device vs chemically modified device
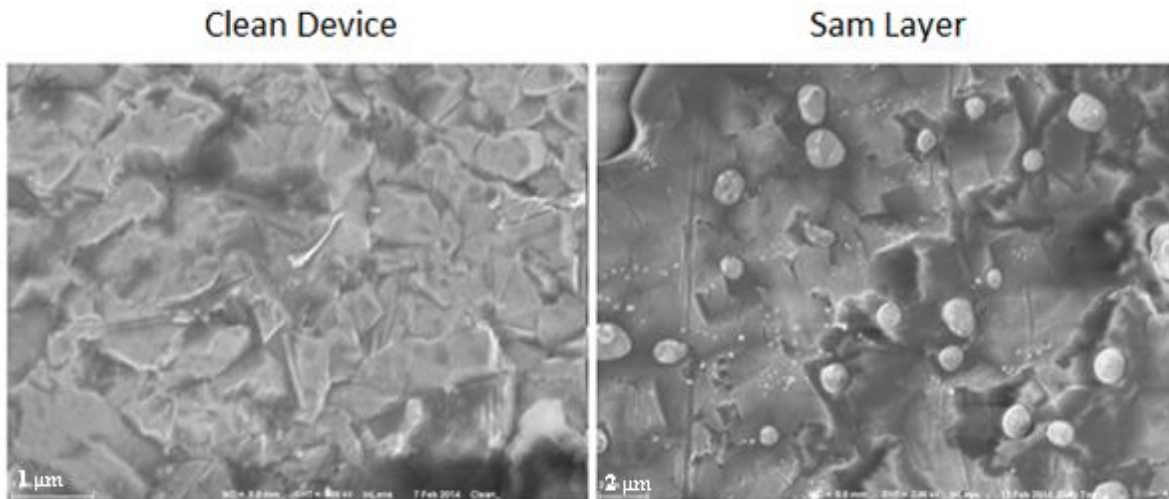
Figure 6.7 – SEM imaging of Figure X taken at 1 micron

Figure 6.6 is taken at a scale of 100 microns and 200 microns for the clean and chemically

modified device respectively, while Figure 6.7 demonstrates the same device taken at 1 micron

and 2 microns for the clean and chemically modified device respectively. The roughness of the

surface is attributed to surface imperfections. Furthermore, it can be seen that variable spacing

exists between each observed element, as well as variable size. SEM imaging taken of two

separate single elements present in the SAM layer can be seen in Figure 6.9.
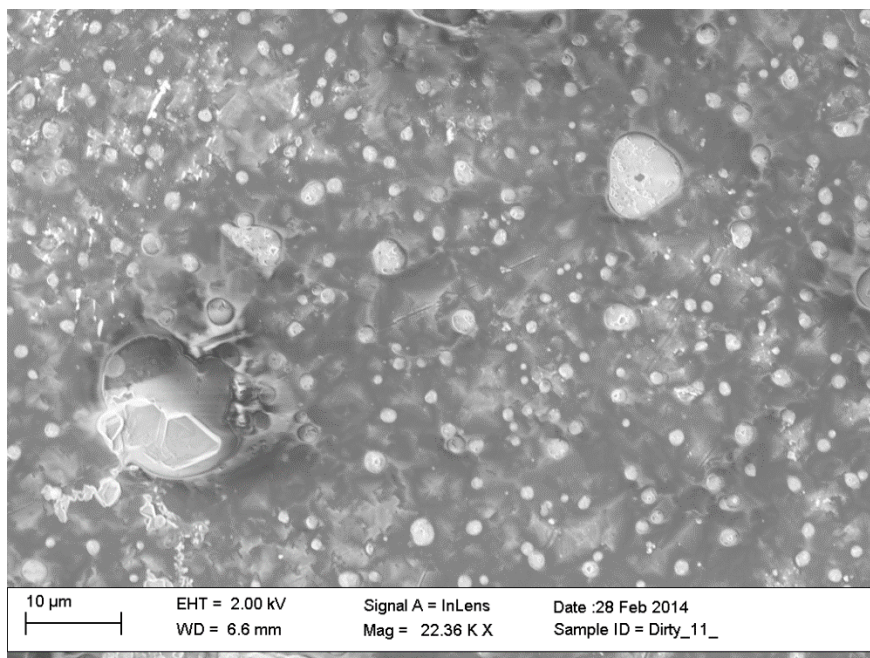
Figure 6.8 – Additional SEM image of SAM layer taken at 10 microns
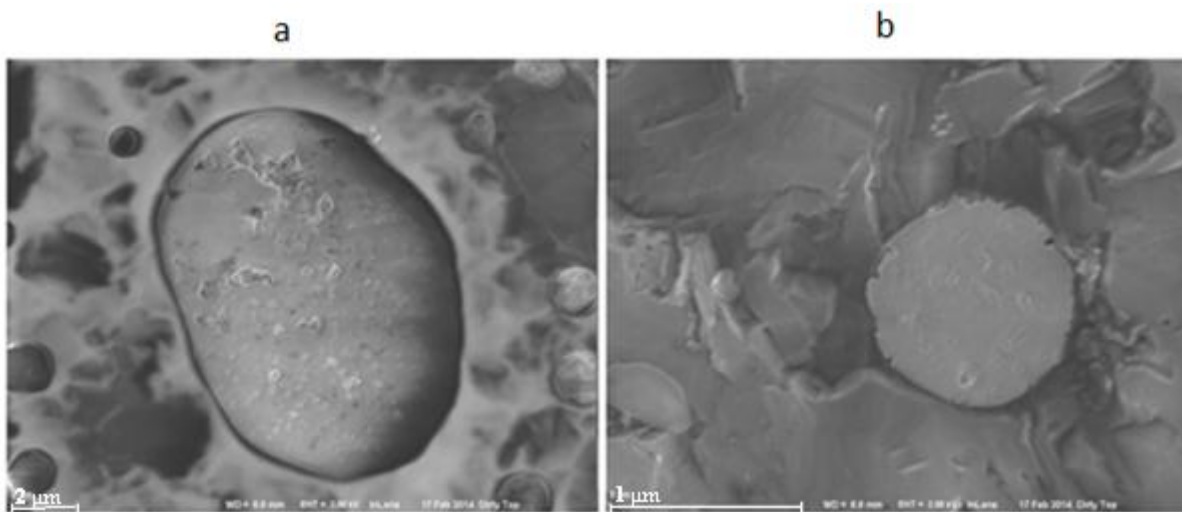
Figure 6.9 – SEM imaging of a SAM layer element up close

Figure 6.9, depicts two separate elements present on the gold surface after chemical preparation

of the SAM layer. The image on the left (a) is shown at a scale of 2 microns, while the image on

the right (b) is shown at a scale of 3 microns. As can be seen from the two elements, variable size

exists among each of the elements and at this point it is unclear what governs the size or spacing of these elements.

6.1.3 Sensing performance

Upon introduction of target analyte (Human MIG) a decrease in current is observed. Two separate experiments verify the change is consistent and the magnitude of this change falls between the range of 80µA-90µA. The volume of sample used is kept constant throughout experiments and any deviation between experiments is due to non-uniform concentration distribution and/or SAM layer integrity. A figure demonstrating results of the two most profound experimental results on different HEMT devices can be seen in Figure 6.10.
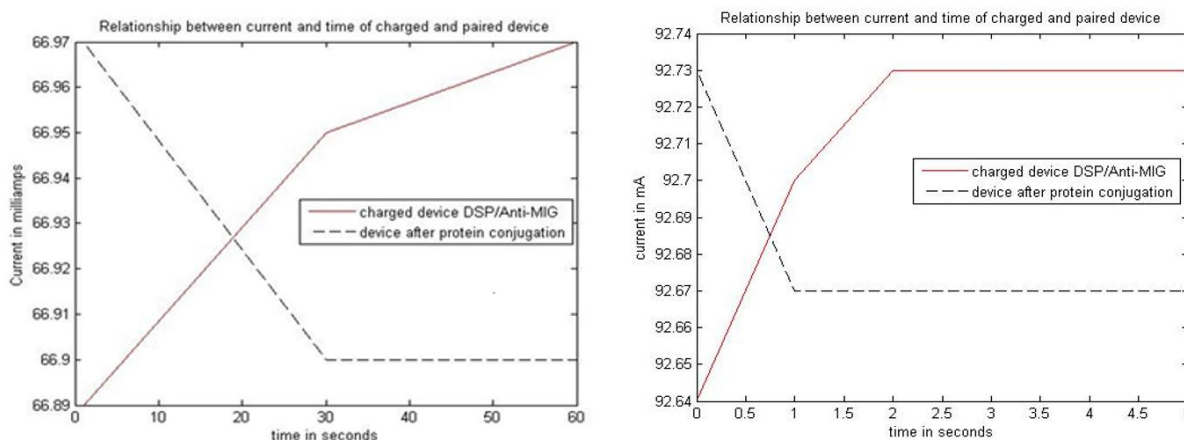
Figure 6.10 – Experimental data taken from two experiments

In the left image, the resistance used is 140Ω and power supply is 10 volts, while the image on the right consists of the circuit seen in Figure 6.5. The left image depicts the first successful results obtained, while the right image depicts the most recent results. Changes in steady state current in more modern procedures are seen to occur much more rapidly than the first results obtained. This is most likely attributed to trial and error, and developments in the preparation techniques resulting in better development of the recipe for biosensor preparation. Images taken of the biosensors used

in experiment can be seen in Figure 6.11 and SEM images can be seen in Figure 6.12 of the surface

after the addition of MIG.
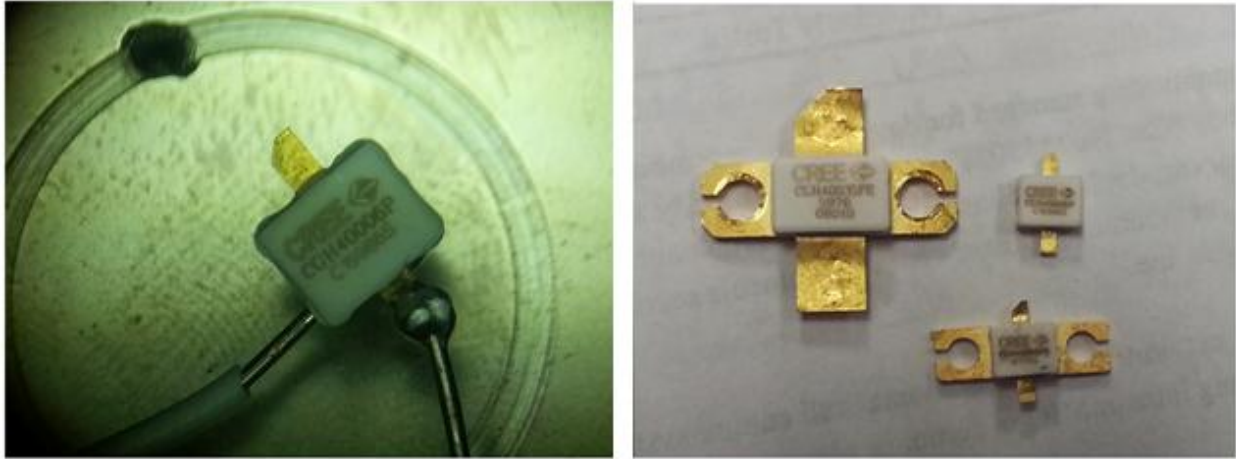
Figure 6.11 – Variations of biosensors used in experiment
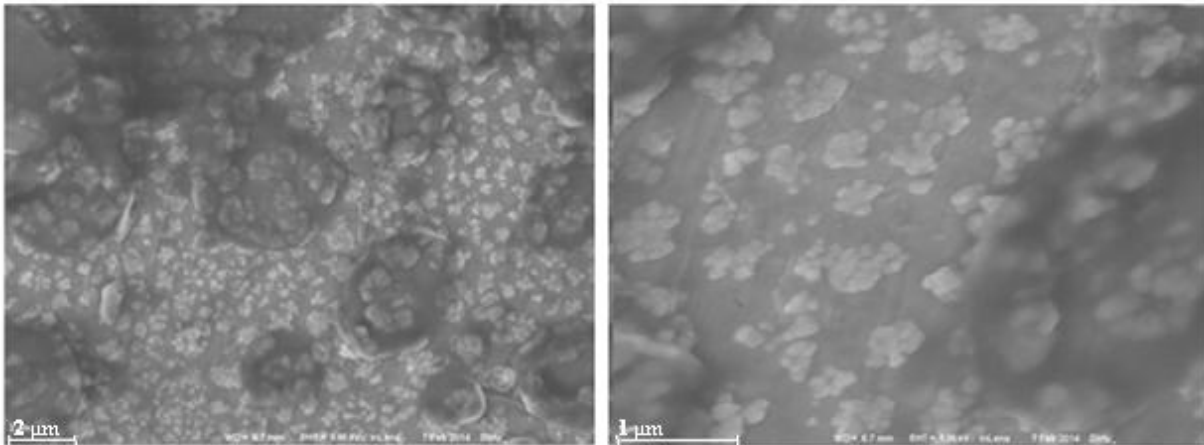
Figure 6.12 – SEM imaging of gate surface after addition of MIG

In figure 6.11, the left-most image represents a ready-to-use biosensor while the right-most

image represents the variety of GaN HEMTs used in experiment. In figure 6.12 images taken

from the surface after the addition of Human MIG are taken at 2 microns and 1 micron

respectively from left-most image to right-most image. A noticeable change in size and shape of

the elements seen before in SAM layer images are apparent.

The HEMTs used in preparation of these biosensors are seen to be packaged AlGaN/GaN devices. The use of packaged devices over bare die holds many advantages. For example, preparation of a biosensor on a bare die is rigorous and due to the fragile nature of the devices, careful preparation and cleanliness must be exercised to ensure device characteristics are not altered by the addition of any ambient contamination. The packaging also serves as a convenient insulating barrier between device contacts and greatly reduce the effect of creating a short across the terminals through the electrolytic solution. Secondly, the packaging provides greater stability and the extension of external contacts provide surface electrodes of a greater area allowing for greater quantities of target solution to be used. This should, in theory, provide greater detection results. The influence of device packaging and its effects must be addressed to relieve any doubts in the integrity of the sensing process. The packaging, along with other concerns will be addressed in the following sections.

6.2 Influence of device packaging

The influence of device packaging is discussed in this section and validated with both literature, and the standard 2DEG model as given in Chapter 4. Two major concerns that may arise from the use of packaged devices may be parasitic effects, and electrode-to-die connections. To address the parasitics induced by the packaging, some literature is reviewed.

According to work done by Mark Pavier et al. (2003) the effect of packaging on power MOSFETs was found to induce resistive and inductive effects [101]. These effects extend to device packaging found on GaN based HEMT devices [102-103]. Since no alternating current is being applied in this application, and the charges induced by way of capacitive coupling are DC, the effect of internal inductance can be ignored. Package resistance may also be neglected experimentally, because the sensing effects observed in this thesis are apparent and are taken

95

from the device after the packaging effects are taken into consideration. Further testing can be

done however to determine if a bare AlGaN/GaN HEMT die may exhibit greater detection

sensitivity than its packaged counterpart. This study may also address deviations in drain current

between experiment and simulation.

Now the effect of external electrode-to-die connections is discussed. In order to address

this concern, the general model for 2DEG sheet carrier density must be revisited. The equation is

reposted here for convenience.

$$n_s(x) = \frac{+\sigma_B}{q} - \frac{\varepsilon_r(x)\varepsilon_0}{dq^2}\left[\phi_B(x) + E_F\big(n_s(x)\big) - \Delta E_C(x)\right] \qquad (5.1)$$

At this point, it is clear that the Schottky barrier height plays a significant role in the

2DEG sheet carrier density. First, it is apparent from equation 5.1 that any degradation of the

Schottky barrier height will directly result in a decrease in 2DEG. Secondly, any increase in

Schottky barrier height would provide a bigger factor in the increase of the 2DEG, however, as

seen before in figure 4.4 in chapter 4, as the Schottky barrier height increases, if all other factors

are held constant, the quantum well depth (and area) will decrease as the conduction band at the

interface requires greater band bending to form the quantum well. In order to achieve the same

quantum well depth, compensation would need to be made in AlGaN barrier thickness, molar

concentration, or by the addition of impurities. This option isn't cost-effective compared to using

a solely intrinsic device, so for this reason two scenarios are proposed to maintain the integrity of

the 2DEG. The first scenario is that the connection that connects the die to the electrode is all

made of the same material. Nickel-gold is a common metal deposited on AlGaN/GaN HEMT

dies to ensure a desired Schottky barrier height [60]. It is also known that the devices used in

experiment are also made from a nickel-gold alloy which makes this a reliable option. The

second scenario is that the interconnect that connects the electrode to the die is made from a

metal exhibiting a similar work function to the nickel-gold alloy. This would allow consistency

in the Schottky barrier height and allow the device to maintain the same output characteristics

without any degradation in the 2DEG. Furthermore, the addition of this interconnect doesn't

interrupt any sensing performance. To obey the net neutrality equation, the external electrode

(and interconnect) serves as an extension of the gate on the die. The net surface states exhibited

by the extended electrode modulate the 2DEG until net neutrality is satisfied (as all other

polarizations are held constant and not affected by the deposition of metal). Any change in these

surface states will be directly impactful on the 2DEG and sensor operation will work in the same

manner as its die counterpart. A table listing several elements and their work functions (which

are dependent on surface cleanliness, and crystal structure) can be seen in Table 6.1 [103].

Table 6.1 List of Various Elements and their work functions [103]

Element	Work function (eV)
Silver (Ag)	4.60-4.85
Gold (Au)	5.31-5.47
Copper (Cu)	4.48-5.10
Nickel (Ni)	5.04-5.35
Chromium (Cr)	4.5
Tungsten (W)	4.32-5.22
Titanium (Ti)	4.33
Tin (Sn)	4.42
Zinc (Zn)	3.63-4.9
Aluminum (Al)	4.06-4.26

To further validate the use of packaged AlGaN/GaN HEMTs for sensor usage, some

literature is referenced. Experiments done by Thapa et al. (2012) in which GaN based HEMT

devices are used in packaged form to detect DNA hybridization are also key indicators that

packaged biosensors from AlGaN/GaN based HEMT devices are not only feasible, but much more convenient and facile to prepare [60].

6.3 Repeatability

Repeatability is an issue with details that need to be investigated further, and can possibly be conducted as a standalone topic. However, from datasheets and previous research it is known that DSP is a cleavable crosslinker, which allows the antibodies to be removed from the reactive groups of the crosslinker. This would allow the crosslinker to be used again in theory. However, in practice a variety of concerns need to be addressed beforehand, mainly inactivity of the crosslinker. DSP has a storing temperature of 4 degrees Celsius and is moisture sensitive. If it is stored outside that temperature for too long, it is possible for the reactive ends to become inactive [53][105]. Furthermore, hydrolization of these reactive groups may have also occurred during the process in which the DSP molecules were bonded to the gold surface. This results in non-reactivity from the NHS-ester reactive end groups. This is another concern that needs to be taken into account, and for this reason each experiment requires a fresh preparation of crosslinker [53][105].

Since DSP bonds covalently to the gold surface, it is highly unexpected that these elements can be removed from the gold surface without rigorous chemical procedure. To validate that the elements are bonded to the gold surface covalently, a previously modified device is rubbed with a solution of 91% Isopropyl alcohol and observed using scanning electron microscopy (SEM). Figures 6.13, and 6.14 demonstrate the images of the surface before and after this "cleaning".
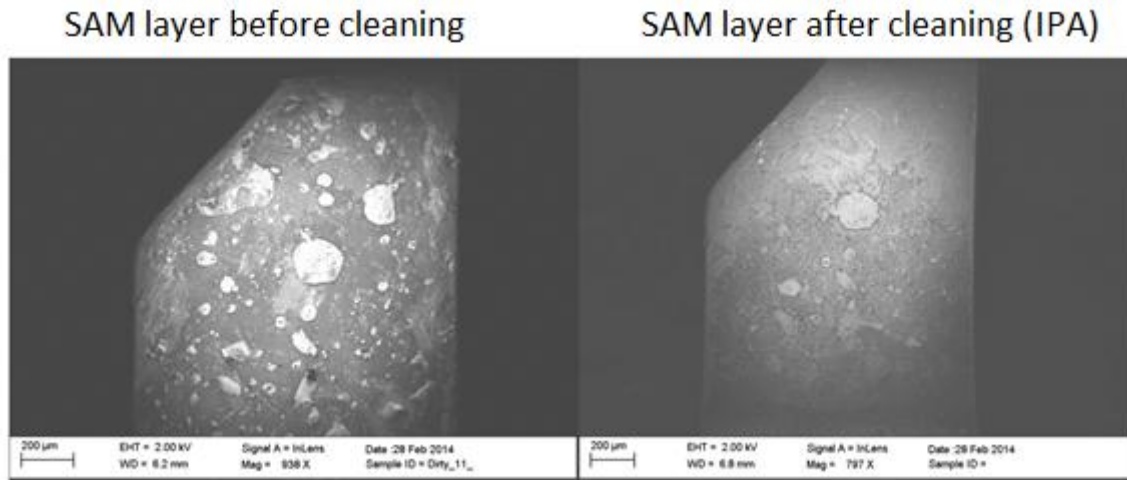
Figure 6.13 – SAM layer before and after cleaning with 91% IPA
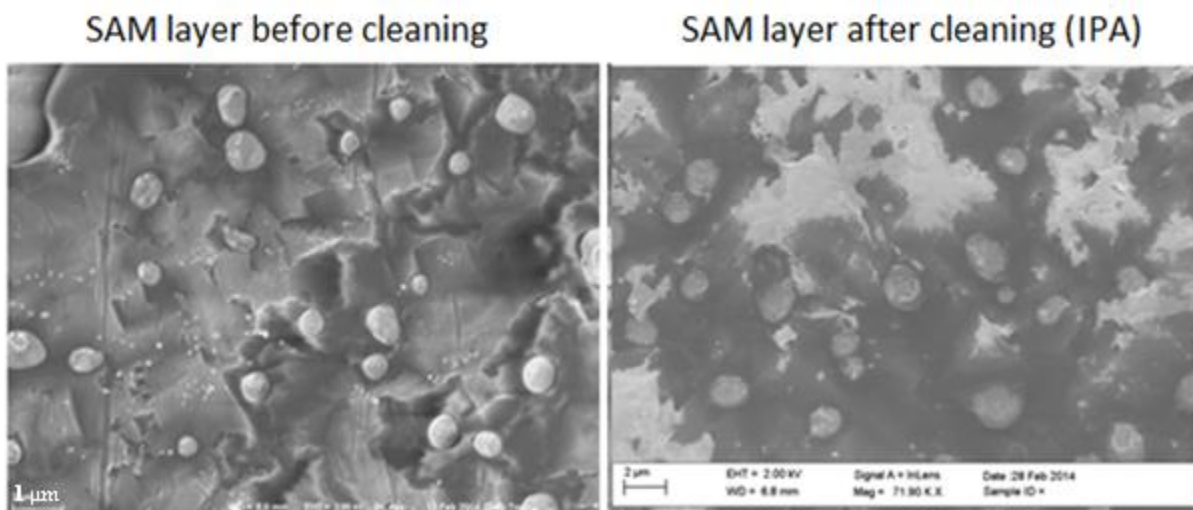
Figure 6.14 – SAM layer before and after IPA viewed at 2 microns

In these images, residues left from the isopropyl alcohol become apparent, but the elements from beforehand are still present as expected.

Results from these experiments validate that theoretically it is possible to use the same biosensor again by cleaving the used antibodies and re-attaching new ones, but further investigation is needed to validate it. Some other factors are also important to maintain sensor integrity such as proper handling and storage, procedure to guarantee repeatability, etc. These are factors that also require further investigation.

6.4 Effect of chemical modification on threshold

An interesting effect was noticed in changes in threshold voltage after chemical

modification of the device. A device that was tested for output characteristics approximately 6

months after experimentation was found to exhibit a more positive threshold voltage value

outside the range guaranteed by the manufacturer datasheet. This prompted further investigation

into this phenomenon with newer experimental devices. Figure 6.15, depicts this initial

discovery, and figure 6.16 shows the device used in the extraction of these results.
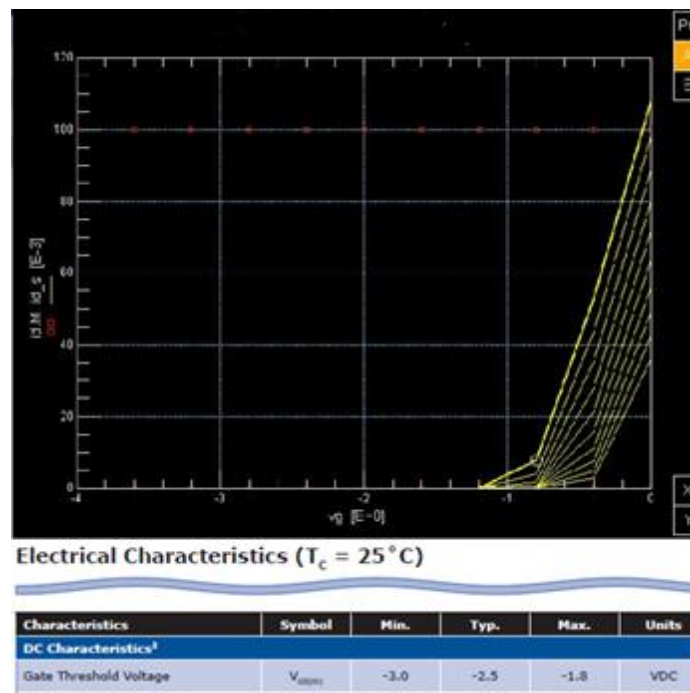
Figure 6.15 – Probe station results demonstrating a shift in threshold voltage

Figure 6.16 – HEMT used to obtain threshold data from the previous figure. Corrosion is obvious in this picture taken at around 8 months after experiment.

To explain why this happens the interface polarization formula, net neutrality equation, and the charge-control model for threshold voltage must be revisited. They are reposted here for convenience in equations 5.2, 5.3, and 5.4 respectively.

$$P_{(x)} = \left(Q_{\pi,}AlGaN\right) + \left(-Q_{\pi,}GaN\right) = \sigma_{pol} \tag{5.2}$$

$$\sigma_{Surface} + \sigma_{AlGaN} + \sigma_{pol} + \sigma_{buffer} - qn_s = 0 \tag{5.3}$$

$$V_{th} = \phi_B - \Delta E_C - \frac{qN_s d_{AlGaN}^2}{2\varepsilon_{AlGaN}} - \sigma_{pol} \frac{d_{AlGaN}}{\varepsilon_{AlGaN}} \tag{5.4}$$

As referenced before, in a truly undoped HEMT the net contribution by σ_{AlGaN}, σ_{pol}, and σ_{buffer} should be zero [60-61]. It is safe to assume this because even if there exists some doping and the σ_{AlGaN} and σ_{buffer} polarizations are not negligible, they contribute no additional effect upon chemical modification because these polarizations are a function of the crystal lattice structure of the material and their interactions in the epitaxy. For this reason, they are independent of any modulation caused by any chemical modifications. However, the modulation of surface states due to modification of the work function via chemical reactions at the gate surface, and the polarizations present at the AlGaN/GaN interface are not safe from these assumptions [60-61]. By holding polarizations due to AlGaN, and the buffer constant, we see by equation 5.2 that as the 2DEG increases, the net polarization at the interface, σ_{pol}, (normally net positive) decreases in magnitude resulting in a smaller value for σ_{pol}. This satisfies equation 5.3 in which any change in the polarizations must be compensated by the 2DEG (n_s). Furthermore, we see that as the value for σ_{pol} becomes less positive, the resulting factor equation 5.4 becomes smaller resulting in a smaller absolute value being subtracted in the equation. This leads to a more positive result in threshold voltage. To validate this theory, a clean device is tested and threshold characteristics are extracted. Then, the SAM layer is chemically prepared and the threshold is re-

measured 2 weeks, 4 weeks, and 7 weeks after initial preparation. The threshold is seen to exhibit a slight positive shifting that is attributed to the modulation of the work function of the gate by way of chemical reaction at the gate. The collected data of Drain Current vs Gate Voltage can be seen in Figure 6.17.
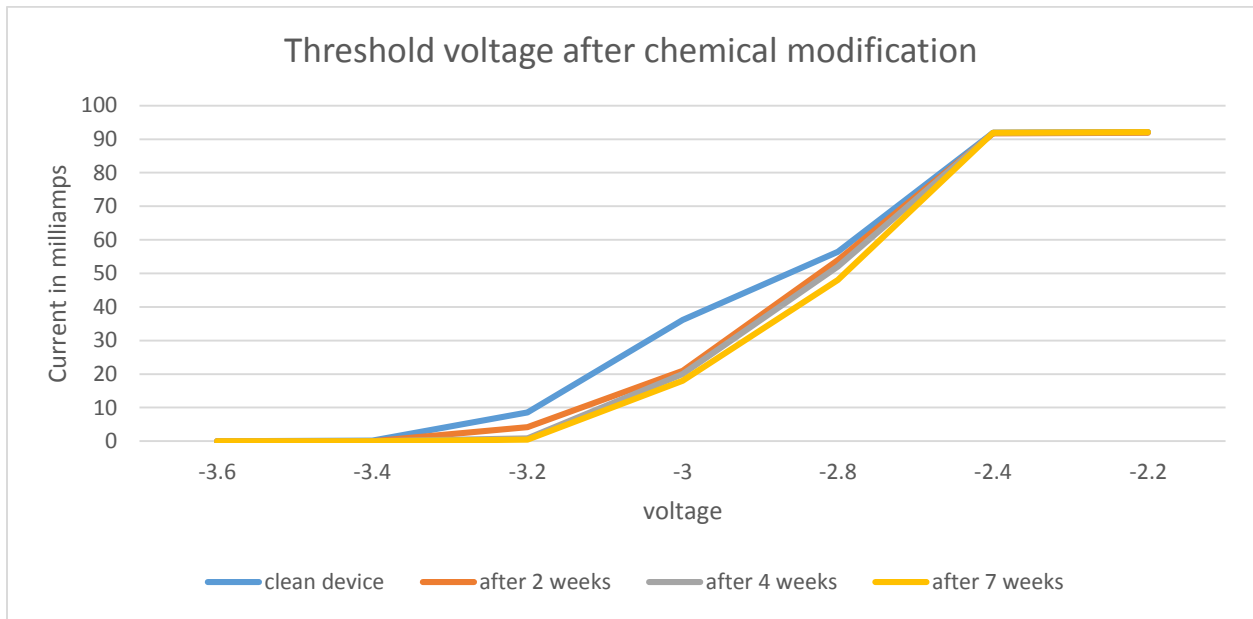
Figure 6.17 – Threshold voltage taken several weeks after experiment

As can be seen by figure 6.17, there exists a slight shift in threshold voltage when measured in two week intervals. While the results may not be as profound as the initial observation (quite possibly due to larger electrode surface and/or obvious reaction with the copper tape of the first device), they are definite and bear an impact on the output characteristics of the device.

CHAPTER VII

CONCLUSIONS AND FUTURE WORK

In conclusion, a biosensor for amperometric detection of Human CXCL9 is realized experimentally using packaged AlGaN/GaN HEMT devices. Analytical and numerical modeling of the device is derived and shown to be in good agreement/exhibit consistent behavior with that seen in experimentation. Device characteristics are studied at each step of sensor performance using two-dimensional physics based modeling and are used in conjunction with literature to conclude the mechanism of action on the proposed sensor. Deviations in current magnitude between experiment and simulation are attributed the assumption of ideal conditions, and negligence of real-life parasitic effects, surface chemistry, and trapping effects not considered by the theoretical two-dimensional software. This allows the model derived in this thesis to be refined to accommodate for such effects seen in real-life applications. Furthermore, threshold shifting is shown to be a consequence of chemical modification of the device and is explained using widely accepted HEMT mathematical models.

7.1 Executive Summary

By using SILVACO's virtual wafer tools: DECKBUILD, ATLAS, and TONYPLOT a numerical model is constructed to validate the claims made throughout this thesis regarding mode of action by modulation of drain current through immobilized charge distribution. The theory is derived through simulation and literature of multiple subjects covering various electrical engineering, chemistry, electrochemistry, and biological engineering topics. A device

model is derived by molding device characteristics to match those seen in experiment. This allows a reference device with characteristics in which any changes can be observed. By using this reference, an analytical model derives a bias voltage to be applied to the gate electrode through chemistry techniques performed using known biological parameters.

The role of the substrate is theoretically explored and the hypothetical conclusion is drawn that SiC and diamond provide optimal substrates for sensor performance compared to sapphire. This claim requires further experimental justification. Furthermore, threshold shifting after chemical modification is explored and explained using the charge-control model, net interface polarization model and the concept of net-neutrality.

7.2 Challenges Provided by this Research

The research presented in this thesis was met with many challenges. For example, an understanding in appropriate chemistry and biology topics was a required pre-requisite. Furthermore, the sensitivity of these biological elements and chemicals to specific ambient conditions made the whole process require a large amount of organization. For example, DSP must be stored at 4 degrees Celsius and is moisture sensitive. Human MIG must be stored in -80 degrees Celsius for prolonged storage and about -20 degrees Celsius for temporary storage, any failure to accommodate for these proteins and chemicals can results in losses in activity.

The very small nature of these biological elements made estimations of charge distribution and charge concentration theoretical. This places the simulation results somewhere in between theory and experiment. Also, the lack of sophisticated equipment to measure certain key aspects of these elements made theoretical analysis a necessity.

Many of the claims made in this thesis had to be heavily researched and applied very selectively to this thesis. The research presented includes works that go beyond the scope of

electrical engineering and into other areas of science and physics. Also, by using commercially available devices, the knowledge of epitaxial layers become unattainable due to manufacturer restrictions and intellectual property. A lot of work was needed to understand the physics of the device, and how each parameter affects device performance in order to rule out certain inclusions of certain layers. Limitations in tool availability were present, and prevented any growing of HEMT transistors on campus.

7.3 Future Work

Future work needs to be conducted on several aspects of the research conducted in this thesis. For example, work needs to be conducted on experimental sensor performance on different substrates to determine which is the most suitable. This could help justify or discredit the claim made in this thesis that sapphire may not be optimal for such an application.

Future testing also needs to be done on the concerns introduced in Chapter 6 regarding repeatability. A variety of key concerns are available in the development of an analytical model using purely theoretical derivations. For example, charge distribution and element concentration in the electrolyte must be explored. Sensitivity of the sensor to various concentrations is also something that needs to be made a priority. This can be done by using a controlled SAM layer with a variable concentration of MIG to determine the range of concentration that the sensor is able to detect without any anomalies or unclear results. Also, the double-layer capacitance and the bias voltage derived in chapter 4 may be measured and justified through experimental techniques. Results may be compared to those derived in chapters 4 and 5.

Finally, the cleavability of DSP and its ability to be re-used is something that must be further investigated. By determining the biological activity of the DSP at different temperatures before and after cleavability, the feasibility of repeatability can be determined as well as other

105

key concerns such as proper handling, device longevity, and proper storage of the sensor devices. Since all work was done in a room temperature environment, the application of temperature to sensor performance may be explored and provide a greater spectrum of use for these type of chemically prepared devices.

REFERENCES

[1]   "GaN-based Power Devices Offer Game-changing Potential in Power-conversion Electronics." *EETimes*. N.p., n.d. Web. 14 Sept. 2013. <http://www.eetimes.com/document.asp?doc_id=1272514>.

[2]   "Wide Band Gap Devices: Powering the next Generation of Electric Traction Drive Systems."*Oak Ridge National Laboratory*. UT-Battelle for the Dept of Energy, n.d. Web. 22 Jan. 2014. <http://web.ornl.gov/sci/ees/transportation/pdfs/WBGBroch.pdf>.

[3]   Ruterana, Pierre, Martin Albrecht, and Jörg Neugebauer. *Nitride Semiconductors: Handbook on Materials and Devices*. Weinheim: Wiley-VCH, 2003. Print.

[4]   Davis, Gregg, Leo Casey, Mark Prestero, Brett Jordan, Jim Scofield, Kirby Keller, Jim Sheahan, Jeffrey Roach, Michael Scherrer, and Rambir Singh. "Predictive & Prognostic Controller for Wide Band Gap (Silicon Carbide) Power Conversion."*IEEE Aerospace Conference*. Big Sky, Montana. N.p.: n.p., n.d. 1-17. Print.

[5]   Choi, Sukwon, Eric Heller, Don Dorsey, and Samuel Graham. "The Analysis of Wide Band Gap Semiconductors Using Raman Spectroscopy." *Materials and Reliability Handbook for Semiconductor Optical and Electron Devices* (2013): 545-82. Web. 14 Sept. 2013. <http://link.springer.com/chapter/10.1007/978-1-4614-4337-7_17?no-access=true#Fig9>.

[6]   Sheng Yun Wu (2010). Low Temperature Phase Separation in Nanowires, Nanowires, Paola Prete (Ed.), ISBN: 978-953-7619-79-4, InTech, DOI: 10.5772/39513. Available from: http://www.intechopen.com/books/nanowires/low-temperature-phase-separation-in-nanowires

[7]   "NSM Archive - Gallium Nitride (GaN) - Basic Electrical Parameters." *NSM Archive - Gallium Nitride (GaN) - Basic Electrical Parameters*. N.p., n.d. Web. 14 Sept. 2013. <http://www.ioffe.rssi.ru/SVA/NSM/Semicond/GaN/ebasic.html>.

[8]   Mishra, Umesh K., Primit Parikh, and Yi-Feng Wu. "AlGaN/GaN HEMTs-An Overview of Device Operation and Applications." *Proceedings of the IEEE* 90.6 (2002): 1022-031. *IEEE XPLORE*. Web. 16 Sept. 2013.

[9]   Takahashi, Kiyoshi, A. Yoshikawa, and Adarsh Sandhu. *Wide Bandgap Semiconductors Fundamental Properties and Modern Photonic and Electronic Devices*. Berlin: Springer, 2007. Print.

[10]   Ren, Fan, and J. C. Zolper. "3 Ga-N Based High Electron Mobility Transistors." *Wide Energy Bandgap Electronic Devices*. River Edge, NJ: World Scientific, 2003. N. pag. Print.

[11]   "History of HEMT Transistors." N.p.: n.p., n.d. N. pag. Fujitsu Laboratories. Web. 15 Sept. 2013. <http://www.docstoc.com/docs/2185695/History-of-HEMT-Transistors>.

[12]   J. C. Bean, "Materials and Technologies," in High-Speed Semiconductor Devices, S. M. Sze, Editor, John Wiley & Sons, New York, 1990.

[13]   Quay, Rüdiger. "III-N Materials, and the State-of-the-Art of Devices and Circuits." *Gallium Nitride Electronics*. Berlin: Springer, 2008. N. pag. Print.

[14]   Tulip, Fahmida S., Edward Eteshola, Syed K. Islam, Salwa Mostafa, and Hasina F. Huq. "Label Free Detection of Human MIG Using AlGaN/GaN High Electron Mobility Transistor." *ISDRS 2011, December 7-9 2011, College Park, MD, USA*

[15]   Kang, B. S., F. Ren, L. Wang, C. Lofton, Weihong W. Tan, S. J. Pearton, A. Dabiran, A. Osinsky, and P. P. Chow. "Electrical Detection of Immobilized Proteins with Ungated AlGaN/GaN High-electron-mobility Transistors." American Institute of Physics, 8 July 2005. Web.

[16]   Eliza, Sazia A., Syed K. Islam, Salwa Mostafa, and Fahmida S. Tulip. "Modeling of AlGaN/GaN HEMT Based Stress Sensors." *6th International Conference on Electrical and Computer Engineering (ICECE)* (2010): n. pag. IEEE, 2010. Web.

[17]   Tulip, Fahmida S., Salwa Mostafa, Syed K. Islam, Edward Eteshola, Sazia A. Eliza, Ida Lee, Elias Greenbaum, and Barbara R. Evans. "GaN-AlGaN High Electron Mobility Transistors for Multiple Biomolecule Detection Such as Photosystem I and Human MIG." *6th International Conference on Electrical and Computer Engineering (ICECE)* (2010): n. pag. IEEE. Web.

[18]   Wang, Yu-Lin, Chih-Cheng Huang, You-Ren Hsu, and Yen-Wen Kang. "Identification of Ligand-receptor Binding Affinity Using AlGaN/GaN High Electron Mobility Transistors and Binding-site Models." *NEMS2013* (2013): n. pag. IEEE. Web.

[19]   Podolska, A., R. M. Seeber, U. K. Mishra, K. D. G Pfleger, G. Parish, and B. D. Nener. "Detection of Biological Reactions by AlGaN/GaN Biosensor." *2012 IEEE* (2012): n. pag. IEEE. Web.

[20]   Salaman, J. R. "Monitoring of Rejection in Renal Transplantation." *NCBI*. U.S. National Library of Medicine, n.d. Web. 17 Nov. 2013.

[21]   Andersen, C. B. "Acute Kidney Graft Rejection Morphology and Immunology." *NCBI*. U.S. National Library of Medicine, n.d. Web. 17 Nov. 2013.

[22]   Lenka, T. R., and A. K. Panda. "Characteristics Study of 2DEG Transport Properties of AlGaN/GaN and AlGaAs/GaAs-based HEMT." (2011): n. pag. *National Institute of Science and Technology*. Web. 16 Sept. 2013. <http://journals.ioffe.ru/ftp/2011/05/p660-665.pdf>.

[23]   Alur, Siddharth, Tony Gnanaprakasa, Hui Xu, Yaqi Wang, Aleksandr L. Simonian, Omar A. Oyarzabal, and Minseo Park. "A Biosensor Based on GaN Field Effect Transistor." CS MANTECH Conference, May 2009.

[24]   Mishra, Umesh K., Likun Shen, and Thomas E. Kazior. "GaN-Based RF Power Devices and Amplifiers." *IEEE Xplore*. IEEE, Feb. 2008. Web. 02 Nov. 2013. Chapter 4

[25]   Xing, H., S. Keller, Y. F. Wu, L. McCarthy, I. P. Smorchkova, D. Buttari, R. Coffie, D. S. Green, G. Parish, S. Heikman, L. Shen, N. Zhang, J. J. Xu, B. P. Keller, S. P. DenBaars, and U. K. Mishra. "Gallium Nitride Based Transistors." *Journal of Physics: Condensed Matter* (2001): 7139-157. Print.

[26]   Shrestha, Niraj M., Yuen Y. Wang, Yiming Li, and E. Y. Chang. "Effect of AlN Spacer Layer on AlGaN/GaN HEMTs." Proc. of 16th International Workshop on Computational Electronics, Japan, Nara. N.p.: n.p., n.d. N. pag. Print.

[27]   "Si Implant Enhances AlN Spacer HEMT Drain Current." *Semiconductor Today*. Semiconductor Today, n.d. Web. 21 Sept. 2013. <http://www.semiconductor-today.com/news_items/2011/JULY/MITSUBISHI_020711.html>.

[28]   Chandler, David L. "Explained: Bandgap." *MIT's News Office*. N.p., n.d. Web. 17 Sept. 2013. <http://web.mit.edu/newsoffice/2010/explained-bandgap-0723.html>.

[29]   Burdge, Julia R. "23.3 Band Theory of Conductivity." *Chemistry*. New York: McGraw-Hill, 2011. N. pag. Print.

[30]   "Introduction to Energy Bands." - *TLP Library Introduction to Semiconductors*. University of Cambridge, n.d. Web. 21 Sept. 2013. <http://www.doitpoms.ac.uk/tlplib/semiconductors/energy_band_intro.php>.

[31]   Casey, H. Craig. *Devices for Integrated Circuits: Silicon and III-V Compound Semiconductors*. New York: John Wiley, 1999. Print.

[32]   Brennan, K.F., Brown, April S., Theory of Modern Electronic Semiconductor Devices. 2002: John Wiley & Sons.

[33]   Simin, Grigory. *Polarization in Heterostructures*. University of South Carolina Electrical Engineering, n.d. Web. 22 Sept. 2013. <http://www.ee.sc.edu/personal/faculty/simin/ELCT871/02%20GaN%20Properties.pdf>.

[34]   Longobardi, Giorgia, Florin Udrea, Stephen Sque, Jeroen Croon, Fred Hurkx, Ettore
         Napoli, and Jan Sonsky. "Modelling 2DEG Charges in AlGaN/GaN
         Heterostructures."*Semiconductor Conference (CAS)* 2 (2012): 363-66. *IEEE Xplore*.
         Web. 24 Sept. 2013.

[35]   BioLegend. "Recombinant Human CXCL9 (MIG) (carrier-free) Technical Data Sheet."
         BioLegend, n.d. Web. 9 Sept. 2013. <http://www.biolegend.com/recombinant-human-
         cxcl9-mig-carrier-free-7464.html>.

[36]   Ebioscience. "Anti-Mouse CXCL9 (MIG) PE Technical Datasheet." *Mouse CXCL9
         (MIG) Antibody PE MIG-2F5.5 RUO*. Affymetrix Ebioscience, n.d. Web. 09 Sept. 2013.
         http://www.ebioscience.com/mouse-cxcl9-antibody-pe-mig-2f55.htm>.

[37]   AlphaLISA Research Reagents. "Human C-X-C Motif Chemokine 9 / Monokine Induced
         by Gamma Interferon (CXCL9 / MIG) Kit Tehnical Data Sheet." PerkinElmer, n.d. Web.
         9 Sept. 2013. <http://www.perkinelmer.com/Content/TDLotSheet/TDS-AL280-
         06%20CXCL9_MIG.pdf>.

[38]   Trotta, Tiziana, Susan Costantini, and Giovanni Colonna. "Modelling of the Membrane
         Receptor CXCR3 and Its Complexes with CXCL9, CXCL10, and CXCL11 Chemokines:
         Putative Target for New Drug Design." *National Center for Biotechnology Information*.
         U.S. National Library of Medicine, n.d. Web. 12 Sept. 2013.
         <http://www.ncbi.nlm.nih.gov/pubmed/19800124>.

[39]   Berridge, Michael J. "Cell Signaling Biology." *University of Cambridge* (2012): n. pag.
         Print

[40]   Groom, Jonathon R., and Andrew D. Luster. "CXCR3 in T Cell Function." (2011): 620-
         31. U.S. National Library of Medicine National Institutes of Health. Web. 14 Sept. 2013.
         <http://www.ncbi.nlm.nih.gov/pmc/articles/PMC3065205/>.

[41]   "Chemokine Receptors." *Chemokine Receptors*. News Medical, n.d. Web. 14 Sept. 2013.
         <http://www.news-medical.net/health/Chemokine-Receptors.aspx>.

[42]   "What Are Chemokines." *What Are Chemokines*. SIno Biological Inc., n.d. Web. 14 Sept.
         2013. <http://www.sinobiological.com/What-is-Chemokine-a-5879.html>.

[43]   "Chemotaxis." Boundless, n.d. Web. 14 Sept. 2013.
         <https://www.boundless.com/microbiology/microbial-genetics/sensing-and-signal-
         transduction/chemotaxis/>.

[44]   Hu, H. Z., T. Kanmaz, P. Feng, J. Torrealba, J. Kwun, J. H. Fechner, J. M. Schultz, Y. C.
         Dong, H. T. Kim, W. Dar, M. M. Hamawy, and S. J. Knechtle. "Surveillance Of Acute
         Rejection In Baboon Renal Transplantation By Elevation Of Ip-10 And Mig In Urine."
         Transplantation 78.Supplement 1 (2004): 613-14. Print.

[45]   Whiting, David, George Hsieh, James J. Yun, Amamika Banerji, William Yao, Michael C. Fishbein, John Belperio, Robert M. Strieter, Benjamin Bonavida, and Abbas Ardehali. "Chemokine Monokine Induced by IFN-γ/CXC Chemokine Ligand 9 Stimulates T Lymphocyte Proliferation and Effector Cytokine Production1." *The Journal Of Immunology* 172.12 (2004): 7417-424. *Chemokine Monokine Induced by IFN-γ/CXC Chemokine Ligand 9 Stimulates T Lymphocyte Proliferation and Effector Cytokine Production*. Web. 08 Sept. 2013. <http://www.jimmunol.org/content/172/12/7417.full>.

[46]   Yun, James J., Michael P. Fischbein, David Whiting, Yoshihito Irie, Michael C. Fishbein, Marie D. Burdick, John Belperio, Robert M. Strieter, Hillel Laks, Judith A. Berliner, and Abbas Ardehali. "The Role of MIG/CXCL9 in Cardiac Allograft Vasculopathy." The American Journal of Pathology, Oct. 2002. Web. 9 Sept. 2013. <http://www.ncbi.nlm.nih.gov/pmc/articles/PMC1867280/>.

[47]   Tulip, Fahmida S., Edward Eteshola, Suchita Desai, Salwa Mostafa, Subramanian Roopa, and Syed K. Islam. "Detection of Transplant Rejection Chemokine Protein Biomarker in Physiological Salt Concentration." *IEEE Sensors Journal* 13 (2013): n. pag.

[48]   "Protein Engineering to Solve Problems at Nanoscale" Lee,S.C Dept of Biomedical Engineering, Department of Chemical and Biomolecular Engineering Ohio State University, Dorothy M. Davis Heart and Lung Research Center Ohio State University

[49]   "CXCL9 Antibody Used to Evaluate Immunofet Feasibility in Physiological Salt Environments." (2012): n. pag. *AVIVA Systems Biology*.

[50]   Mohanty, Saraju P., and Elias Kougianos. "Biosensors: A Tutorial Review." *IEEE Potentials* 25.2 (2006): 35-40. *IEEE Xplore*. IEEE. Web. 13 Nov. 2013.

[51]   "Chemistry of Crosslinking." *Chemistry of Crosslinking*. Thermo-Scientific, n.d. Web. 07 Dec. 2013.

[52]   "DSP (Dithiobis[succinimidyl Propionate])." *DSP (Lomants Reagent)*. Thermo-Scientific, n.d. Web. 07 Dec. 2013.

[53]   "Attach a Protein onto a Gold Surface." *Tech Tip #2 : Attach a Protein onto a Gold Surface.* Thermo Scientific,2008 Web.14 Nov. 2012. http://piercenet.com/files/TR0002-Attach-to-gold.pdf

[54]   Huang, Hsin Shun, Chao Wei Lin, and Hsien Chin Chiu. "High Sensitivity pH Sensor Using AlGaN/GaN HEMT Heterostructure Design." IEEE, 2008.

[55]   Vetury, Ramakrishna. *Polarization Induced 2DEG in AlGaN/GaN HEMTs: On the Origin, DC and Transient Characterization*. Diss. University of California at Santa Barbera, 2000. N.p.: n.p., n.d. Print.

[56] Eliza, Sazia A., Syed K. Islam, Ida Lee, Elias Greenbaum, and Fahmida S. Tulip. "Modeling of a Floating Gate AlGaN/GaN Heterostructure-Transistor Based Sensor." *ISDRS 2009* (2009): n. pag. IEEE

[57] Xu, Dong, Kanin Chu, Jose Diaz, Wenhua Zhu, Richard Roy, Louis Mt Pleasant, Kirby Nichols, Pane Chane Chao, Min Xu, and Peide D. Ye. "0.2- mu{rm M} AlGaN/GaN High Electron-Mobility Transistors With Atomic Layer Deposition {rm Al}_{2}{rm O}_{3} Passivation." IEEE, n.d.

[58] Zhihong, Feng, Xie Shengyin, Zhou Rui, Yin Jiayun, Zhou Wei, and Cai Shujun. "A High-performance Enhancement-mode AlGaN/GaN HEMT." *Journal of Semiconductors - Institute of Physics* 31.8 (2010):

[59] Tanuma, N., M. Tacano, S. Yagi, and J. Sikula. "Low-Frequency-noise Monitoring of Current Collapse in AlGaN/GaN High-electron Mobility Transistors on Sapphire Subtrate." Journal of Statistical Mechanics: Theory and Experiment / Institute of Physics, 2009. Web.

[60] Thapa, Resham, Siddharth Alur, Kyusang Kim, Fei Tong, Yogesh Sharma, Moonil Kim, Claude Ahyi, Jing Dai, Jong Wook Hong, Michael Bozack, John Williams, Ahjeong Son, Amir Dabiran, and Minseo Park. "Biofunctionalized AlGaN/GaN High Electron Mobility Transistor for DNA Hybridization Detection." *Applied Physics Letters*100.23 (2012): 232109. Print

[61] J.P. Ibbetson, P.T. Fini, K.D. Ness, S.PDenBars, J.S.Speck, U.K.Mishra, "Polarization effects, surface states and the source of electrons in AlGaN/GaN heterostructure field effect transistors", Appl Phys. Letters. 77(2) July 2000 p.250-252

[62] Yu, Chen-Hui, Qing-Zhou Luo, Xiang-Dong Luo, and Pei-Sheng Liu. "Donor-Like Surface Traps on Two-Dimensional Electron Gas and Current Collapse of AlGaN/GaN HEMTs." *The Scientific World Journal* 2013 (2013): 1-6. Print.

[63] Spicer, W. E., Liliental-Weber Z, E. Weber, N. Newman, T. Kendelewicz, R. Cao, C. McCants, P. Mahowald, K. Miyano, and I. Lindau. "The Advanced Unified Defect Model for Schottky Barrier Formation." *Journal of Vacuum Science & Technology B: Microelectronics and Nanometer Structures* 6.4 (1988): 1245. Print.

[64] Kurtin, S., T. Mcgill, and C. Mead. "Fundamental Transition In The Electronic Nature Of Solids." *Physical Review Letters* 22.26 (1969): 1433-436. Print.

[65] Alam, A., B. Schineller, M. Heuken, H. Juergensen, H. Hardtdegen, M. Marso, N. Nastase, H. Bay, P. Kordos, and H. Luth. "The Role of AlN and GaN Nucleation Layers on the Performance of Doped and Undoped Nitride HEMT Structures Grown by

MOCVD." *WOCSDICE* (2001): n. pag. Web. 20 Feb. 2014.
<http://www.lehighton.com/AppNotes/AIXTRONPaper1.pdf>.

[66]   W. Schottky, Zeitschrift fur Physik 118, 539 (1942).

[67]   Freeouf, J. L., and J. M. Woodall. "Schottkey Barriers: An Effective Work Function
        Model." *Applied Physics Letters* 39 (1981): n. pag. Web. 21 Feb. 2014.

[68]   Goyal, Nitin. *Design and Modeling of High- Power Semiconductor Devices with
        Emphasis on AlGaN/GaN HEMTs*. Diss. Norwegian University of Science and
        Technology, 2013. N.p.: n.p., n.d. Print.

[69]   Goyal, Nitin, and Tor A. Fjeldly. "Impact of Gate Metal on Surface States Distribution
        and Effective Surface Barrier Height in AlGaN/GaN Heterostructures." *MRS
        Proceedings*1538 (2013): 335-40. Print.

[70]   Bardeen, J. (1947). "Surface States and Rectification at a Metal Semi-Conductor
        Contact". *Physical Review* **71**(10)

[71]   H. Luth, *Solid Surfaces, Interfaces, and Films,* Springer-Verlag Berlin Heidelberg, New
        York, NY, 2001.

[72]   A. M. Cowley and S. M. Sze, "Surface States and Barrier Height of Metal-Semiconductor
        Systems", J. Appl. Phys. 95, 7940 (2004)

[73]   "MSE 5317 - Electronic Properties of Materials." N.p., n.d. Web. 26 Feb. 2014.
        <http://electrons.wikidot.com/>.

[74]   R. Ramprasad, Paul von Allmen and L. R. C. Fonseca,"Contributions to the work
        function: a density functional study of adsorbates at graphene ribbon edges", Phys. Rev.
        B, 60, pp. 6023, 1999.

[75]   Myland, Jan. "What Is Electrochemistry?" Trent University, 04 Apr. 1998. Web.

[76]   Delahay, Paul. *Double Layer and Electrode Kinetics*. New York: Interscience, 1965.
        Print.

[77]   Bard, Allen J., and Larry R. Faulkner. *Electrochemical Methods: Fundamentals and
        Applications*. New York: Wiley, 1980. Print.

[78]   Noble, Peter A. "Hypothetical Model for Monitoring Microbial Growth by Using
        Capacitance Measurements – a Minireview." *Journal of Microbiological Methods* 37.1
        (1999): 45-49. Print.

[79]   Noble, Peter A., Michael Dziuba, D.jed Harrison, and William L. Albritton. "Factors Influencing Capacitance-based Monitoring of Microbial Growth." *Journal of Microbiological Methods* 37.1 (1999): 51-64. Print.

[80]   S. Srinivasan, Fuel Cells, From Fundamentals to Applications, Springer eBooks, 2006, ISBN 978-0-387-35402-6, Chapter 2, Electrode/Electrolyte Interfaces: Structure and Kinetics of charge transfer.

[81]   Charfeddine, Manel, Hafedh Belmabrouk, Mohamed Ali Zaidi, and Hassen Maaref. "2-D Theoretical Model for Current-Voltage Characteristics in AlGaN/GaN HEMT's."*Journal of Modern Physics* 3.8 (2012):

[82]   Rashmi, A. Kranti, S. Haldar, M. Gupta and R. S. Gupta, "An Accurate Charge Control Model for Spontaneous and Piezoelectric Polarization Dependent Two-Dimensional Electron Gas Sheet Charge Density of Lattice

[83]   Farahmand, Maziar, Carlo Garetto, Enrico Bellotti, Kevin F. Brennan, Michele Goano, Enrico Ghillino, Gio0vanni Ghione, John D. Albrecht, and P. Paul Rudden. "Monte Carlo Simulation of Electron Transport in the III-Nitride Wurtzite Phase Materials System: Binaries and Ternaries." *IEEE Transactions on Electron Devices* 48.3 (2001): n. pag. Print.

[84]   Albrecht, J.D. et al, "Electron transport characteristics of GaN for high temperature device modeling", *J. Appl. Phys.* Vol. 83 (1998): 4777-4781.

[85]   "CXCL9 Recombinant Human Protein." - *Proteins, Enzymes, & Peptides*. N.p., n.d. Web. 19 Nov. 2013.

[86]   "Recombinant Human CXCL9 MIG Carrier-free - BioLegend." *Recombinant Human CXCL9 MIG Carrier-free - BioLegend*. N.p., n.d. Web. 19 Nov. 2013.

[87]   "Recombinant Mouse CXCL9/MIG." *Recombinant Mouse CXCL9/MIG*. N.p., n.d. Web. 19 Nov. 2013.

[88]   F. M. Abou El-Ela and A. Z. Mohamed, "Electron Transport Characteristics of Wurtzite GaN," ISRN Condensed Matter Physics, vol. 2013, Article ID 654752, 6 pages, 2013. doi:10.1155/2013/654752

[89]   Albrecht, J. D., R. P. Wang, P. P. Ruden, M. Farahmand, and K. F. Brennan. "Electron Transport Characteristics of GaN for High Temperature Device Modeling." *Journal of Applied Physics* 83.9 (1998): 4777. Print.

[90]   *SILVACO Atlas User's Manual*. 17 Oct. 2013. Device simulation software. Santa Clara, CA.

[91]   Dridi, Z., B. Bouhafs, and P. Ruterana. "First-principles Investigation of Lattice Constants and Bowing Parameters in Wurtzite AlGaN, InGaN and InAlN Alloys." *Semiconductor Science and Technology* 18.9 (2003): 850-56. Print.

[92]   "Sapphire." *Janis Research Libraries*. N.p., n.d. Web. 3 Mar. 2014. <http://www.janis.com/Libraries/Window_Transmissions/Sapphire_Al2O3_TransmissionCurveDataSheet.sflb.ashx>.

[93]   "Sapphire (Al2O3)." *Sapphire (Al2O3)*. N.p., n.d. Web. 03 Mar. 2014. <http://www.mt-berlin.com/frames_cryst/descriptions/sapphire.htm>.

[94]   "Basic Parameters of Silicon Carbide (SiC)." *Basic Parameters of Silicon Carbide (SiC)*. N.p., n.d. Web. 03 Mar. 2014. <http://www.ioffe.ru/SVA/NSM/Semicond/SiC/basic.html>.

[95]   Nowak, Stanishaw. "Crystal Lattice Dynamics of Various Silicon-Carbide Polytypes."*International Conference on Solid State Crystals*. Technical University , Poland, 2000. Web.

[96]   "Crystal Structures and Lattice Constants of Semiconductors and Other Materials." *Crystal Structures and Lattice Constants of Semiconductors and Other Materials*. N.p., n.d. Web. 03 Mar. 2014. <http://www.siliconfareast.com/lattice_constants.htm>.

[97]   "NSM Archive - Aluminium Nitride (AlN) -Basic Parameters." *NSM Archive - Aluminium Nitride (AlN) -Basic Parameters*. N.p., n.d. Web. 03 Mar. 2014. <http://www.ioffe.ru/SVA/NSM/Semicond/AlN/basic.html>.

[98]   "Basic Parameters of Indium Nitride (InN)." *Basic Parameters of Indium Nitride (InN)*. N.p., n.d. Web. 03 Mar. 2014. <http://www.ioffe.ru/SVA/NSM/Semicond/InN/basic.html>.

[99]   "NSM Archive - Indium Nitride (InN) - Band Structure." *NSM Archive - Indium Nitride (InN) - Band Structure*. N.p., n.d. Web. 03 Mar. 2014. <http://www.ioffe.ru/SVA/NSM/Semicond/InN/bandstr.html>.

[100]   McAuley, David, Pharm D. "Common Laboratory (LAB) Values - ABGs - Arterial Blood Gases." *Common Laboratory (LAB) Values - ABGs - Arterial Blood Gases*. N.p., n.d. Web. 17 Mar. 2014. <http://www.globalrph.com/abg_analysis.htm>.

[101] Pavier, Mark, Arthur Woodworth, Andrew Sawle, Hurst Green, Ralph Monteiro, Carl Blake, and Jason Chiu. "Understanding the Effect of Power MOSFET Package Parasitics on VRM Circuit Efficiency at Frequencies above 1MHz." International Rectifier, 2003. Web. <http://www.irf.com/technical-info/whitepaper/pcimeur03packageparasitics.pdf>.

[102] Reusch, David. "Impact of Parasitics on Performance." Efficient Power Converstion Corporation, n.d. Web. <http://epc-co.com/epc/documents/papers/Impact%20of%20Parasitcs%20on%20Performance.pdf>.

[103] "Delivering Efficient Power Converstion With Package-Free HEMTs." Compound Semiconductor, 24 June 2013. Web. <http://www.compoundsemiconductor.net/csc/features-details/19736511/Delivering-efficient-power-conversion-with-package-free-HEMT.html>.

[104] David R. Lide, ed., CRC Handbook of Chemistry and Physics, Internet Version 2005, <http://www.hbcpnetbase.com>, CRC Press, Boca Raton, FL, 2005. p 12-124.

[105] "DTSSP/DSP." *Instructions*. Thermo Scientific, n.d. Web. 19 Mar. 2014. <https://www.piercenet.com/instructions/2160544.pdf>.

[106] "Acute vs. Chronic Conditions: MedlinePlus Medical Encyclopedia Image." *U.S National Library of Medicine*. U.S. National Library of Medicine, n.d. Web. 09 Sept. 2013. <http://www.nlm.nih.gov/medlineplus/ency/imagepages/18126.htm>.

[107] "Definition of Agonist." *Definition of Agonist*. Chemicool, n.d. Web. 12 Sept. 2013. <http://www.chemicool.com/definition/agonist.html>.

[108] "Allograft Definition." *Medical-dictionary*. N.p., n.d. Web. 9 Sept. 2013. <http://medical-dictionary.thefreedictionary.com/allograft>.

[109] "Chemoattractant Definition." *Medical-dictionary*. N.p., n.d. Web. 9 Sept. 2013. <http://medical-dictionary.thefreedictionary.com/chemoattractant>.

[110] "Chemokines - What Are Chemokines?" *Chemokines - What Are Chemokines?*News-Medical, n.d. Web. 09 Sept. 2013. <http://www.news-medical.net/health/Chemokines-What-are-Chemokines.aspx>.

[111] "Chemokines: Receptors and Ligands." Clinical Immunology Society, n.d. Web. 9 Sept. 2013. <http://www.clinimmsoc.org/teaching/downloads/chemokines.pdf>.

[112] Murphy PM (2002). "International Union of Pharmacology. XXX. Update on chemokine receptor nomenclature". *Pharmacol. Rev. 54 (2): 227-9.*

[113]   "Chemotaxis Definition." *The Free Dictionary*. The Free Dictionary, n.d. Web.
         <http://www.thefreedictionary.com/chemotaxis>.

[114]   "Genes and Mapped Phenotypes." *National Center for Biotechnology Information*. U.S.
         National Library of Medicine, n.d. Web. 09 Sept. 2013.
         <http://www.ncbi.nlm.nih.gov/gene/2833>.

[115]   "What Are Cytokines?" *What Are Cytokines?* News-Medical, n.d. Web. 09 Sept. 2013.
         <http://www.news-medical.net/health/What-are-Cytokines.aspx>.

[116]   "Differentiation." *Definition from Biology-Online.org*. Biology-Online, n.d. Web. 09
         Sept. 2013. <http://www.biology-online.org/dictionary/Differentiation>.

[117]   de Weerd NA, Samarajiwa SA, Hertzog PJ (2007). "Type I interferon receptors:
         biochemistry and biological functions". *J Biol Chem 282 (28):* 20053-20057.

[118]   "Genes and Mapped Phenotypes." *National Center for Biotechnology Information*. U.S.
         National Library of Medicine, n.d. Web. 09 Sept. 2013.
         <http://www.ncbi.nlm.nih.gov/gene/3458>.

[119]   Berridge, Michael J. "Cell Signaling Biology." *University of Cambridge* (2012): n. pag.
         Print

[120]   "Leukocyte Definition." The Free Dictionary, n.d. Web. 9 Sept. 2013.
         <http://www.thefreedictionary.com/leukocyte>.

[121]   "Ligands." UC Davis ChemWiki, n.d. Web. 12 Sept. 2013.
         <http://chemwiki.ucdavis.edu/Inorganic_Chemistry/Coordination_Chemistry/Ligands>.

[122]   "Lymphocyte (blood Cell)." *Encyclopedia Britannica Online*. Encyclopedia Britannica,
         n.d. Web. 09 Sept. 2013.
         <http://www.britannica.com/EBchecked/topic/352799/lymphocyte>.

[123]   "Macrophage Function." *Macrophage Function*. News-Medical, n.d. Web. 09 Sept. 2013.
         <http://www.news-medical.net/health/Macrophage-Function.aspx>.

[124]   "MonocyteAbout Our Definitions: All Forms of a Word (noun, Verb, Etc.) Are Now
         Displayed on One Page." *Merriam-Webster*. Merriam-Webster, n.d. Web. 09 Sept. 2013.
         <http://www.merriam-webster.com/dictionary/monocyte>.

[125]   "Monokine Definition." Medical-dictionary, n.d. Web. 9 Sept. 2013. <http://medical-
         dictionary.thefreedictionary.com/monokine>.

[126] "T-cells." *About.com Leukemia & Lymphoma*. N.p., n.d. Web. 09 Sept. 2013. <http://lymphoma.about.com/od/glossary/g/tcells.htm>.

APPENDIX

APPENDIX A

CHEMICAL LEXICON

Acute rejection – rejection that is severe and sudden [106].

Agonist – A chemical that can interact with the receptor of a cell and initiate a response by the receptor (secretion, contraction, etc.) [107].

Allogeneic skin graft – Skin Graft involving a tissue/organ that is genetically different from another skin graft coming from a member of the same species [108].

Allograft – Tissue or organ taken from another individual of the same species (but different genotype) and incorporated into another individual [108].

Chemoattractant – An agent of the chemotactic type that attracts and influences cell migration [109].

Chemokine – A family of small cytokines with a mass between 8-10 kDa. Their name comes from the ability to induce direct chemotaxis [110]. There are over 50 known chemokines, and are grouped into one of four distinct families (CXC, CC, CX3C, and XC) based on order of conserved cysteine (C) residues within the protein sequence. The arrangement of these residues is the key to their shape [38].

Chemokine Receptor – Receptors that interact with chemokines. They trigger cell responses, including chemotaxis. There are 19 chemokine receptors found in mammals. They are divided into different families (CC, CXC, CX3C, and XC) [111] [112].

Chemotaxis – Phenomenon where a single cell or multicellular organism is directed (through movement) to a destination via chemicals in their environment [113].

Chronic rejection – rejection that occurs over an extended period of time [108].

Crosslinking – The process in which two or more molecules are joined together through covalent bonding. When referring to the joining of proteins, it is sometimes called bioconjugation.

CXCR3 Chemokine Receptor – Involved in leukocyte trafficking. Interacts with CXC family of chemokines including CXCL9/MIG (monokine induced by interferon gamma), CXCL10/P10 (Interferon-gamma-inducible 10 kDa protein), and CXCL11/I-TAC (Interferon-inducible T cell a-chemoattractant) [114].

Cytokine – small molecules used in cell signaling and intracellular communication. They can be classified as proteins, peptides, or glycoproteins [115].

Dalton- 1 dalton = 1 atomic mass unit = $1.66x10^{-24}$ grams.

Differentiation – The process in which a cell matures and develops into a specialized cell with a more specific function [116].

Interferon – proteins released by host cells with the intent to interfere with foreign entities such as pathogens, tumor cells, bacteria, and viruses [117].

Interferon gamma – a soluble cytokine that encodes a member of the type II family of interferons. It consists of two peptide chains (143 amino acids) that have two N-linked glycosylations. It is produced by T-helper cells, neutrophils, and natural killer cells that are

activated by interleukin-2 (IL2) and interleukin-12 (IL12) This interferon is a significant macrophage activator [118][119].

Leukocyte – A white blood cell. Actively involved in the immunology and defense of the human body [120].

Ligand – A ligand is a neutral molecule or ion that can be viewed a Lewis base (electron donor) that binds to a central metal atom to form a complex. One or more of the Ligand's electron pairs can be donated to the central metal atom [121].

Lymphocyte – A type of leukocyte that originate from stem cells in bone marrow whose main purpose is to serve in immune system response of foreign particles [122].

Macrophage – Phagocyte cells produced by the differentiation of monocytes in tissues. They protect the body by phagocytosing (ingesting) harmful particles, bacteria, and dead or dying cells. Macrophages can function is either specific defense, or non-specific defense mechanisms in vertebrates. Their role as a phagocyte is to engulf and digest foreign/harmful pathogens as a stationary or mobile cell [123].

Monocytes – a Phagocyte with a single nucleus that eventually differentiates into a macrophage upon entering the blood and migration to connective tissues [124].

Monokine – A cytokine produced by macrophages and monocytes that influence the behavior of other cells [125].

Phagocyte – cells that protect the body by phagocytosing harmful particles, pathogens, bacteria, and dead or dying cells [122].

Phagocytosis – The process in which a Phagocyte engulfs and digests a harmful particle, pathogen, bacteria, or dead/dying cell [122].

T-Lymphocyte – T-cells. A type of white blood cell whose main job is to fight infection by attacking foreign entities [126].

APPENDIX B

SILVACO CODE FOR NUMERICAL SIMULATIONS

go atlas


```
################setting variables##########
set devthk=4.0
set SG_space=2
go atlas
################setting variables##########
set devthk=4.0
set SG_space=2
set GD_space=2
set gate_L=2
set devwidth=1+$SG_space+$gate_L+$GD_space
set xmax1=0.5+$SG_space
set xmax2=0.5+$SG_space+$gate_L
set xmax3=0.5+$SG_space+$gate_L+$GD_space
set vstart = 0
set vstop = 4
set vinc = .5

##
######### SPECIFY MESH ########
MESH width=100
#MESH
x.m l=0.0 s=0.50
x.m l=0.5 s=0.50
x.m l=$xmax1 s=0.50
x.m l=$xmax2 s=0.50
x.m l=$xmax3 s=0.50
x.m l=$devwidth s=0.50
#
y.m l=0.000 s=1.000
y.m l=0.400 s=0.500
y.m l=0.500 s=0.050
y.m l=0.518 s=0.010
y.m l=0.530 s=0.010
y.m l=1.000 s=0.050
y.m l=1.250 s=0.100
y.m l=2.025 s=0.500
y.m l=2.040 s=1.000
y.m l=2.065 s=1.000
y.m l=$devthk s=2.000
##

#### Define the regions for materials and electrodes
REGION num=1 mat=air x.min=0.5 x.max=$xmax3 y.min=0 y.max=0.5
REGION num=2 mat=AlGaN x.min=0.5 x.max=$xmax3 y.min=0.5 y.max=0.518 x.comp=0.18
```

124

REGION num=3 mat=GaN x.min=0.5 x.max=$xmax3 y.min=0.518 y.max=1
REGION num=4 mat=GaN x.min=0 x.max=$devwidth y.min=1 y.max=2.025
REGION num=5 mat=AlN x.min=0 x.max=$devwidth y.min=2.025 y.max=2.04
REGION num=6 mat=AlGaN x.min=0 x.max=$devwidth y.min=2.04 y.max=2.065
x.comp=0.18
REGION num=7 mat=SiC x.min=0 x.max=$devwidth y.min=2.065 y.max=$devthk substrate
elec num=1 name=source x.min=0 x.max=0.5 y.min=0 y.max=1
elec num=2 name=gate x.min=$xmax1 x.max=$xmax2 y.min=0 y.max=0.5
elec num=3 name=drain x.min=$xmax3 x.max=$devwidth y.min=0 y.max=1
elec num=4 substrate

#contact name=gate work=5.0

########## Models specification ##########
MODELS k.p albrct fldmob srh print temp=300

####### These are the parameters in Abrecht's low field mobility equations ##########
MOBILITY albrct.n an.albrct=0.1e-4 bn.albrct=0.1e-4 cn.albrct=0.25e-4

INTERFACE charge=1.05e13 y.min=0.518 y.max=0.523 s.s
model polarization calc.strain polar.scale=0.8
THERMCONTACT num=1 y.min=3 y.max=$devthk ext.temp=300 ^boundary alpha=1.7

method newton trap maxtrap=20
output con.band val.band band.param e.mobility h.mobility charge polar.charge

#########Intrinsic device ####################
solve init
save outf=ganfetex03_0.str
tonyplot ganfetex03_0.str
##

solve vdrain=10.0
solve name=gate vfinal=-10 vstep=-0.5
log outf=ganfetex03_0.log
solve name=gate vfinal=1.0 vstep=0.5
log off
tonyplot ganfetex03_0.log -setganfetex03_1.set

################# ID vs VG ##############################
solve init
solve vgate=-3
log outf=ganfetex03_1.log
solve name=drain vdrain=$vstart vfinal=$vstop vstep=$vinc
log off
#

```
solve init
solve vgate=-2
log outf=ganfetex03_2.log
solve name=drain vdrain=$vstart vfinal=$vstop vstep=$vinc
log off
#
solve init
solve vgate=-1
log outf=ganfetex03_3.log
solve name=drain vdrain=$vstart vfinal=$vstop vstep=$vinc
log off
#
solve init
solve vgate=0
log outf=ganfetex03_4.log
solve name=drain vdrain=$vstart vfinal=$vstop vstep=$vinc
log off

solve init
solve vgate=1
log outf=ganfet03_5.log
solve name=drain vdrain=$vstart vfinal=$vstop vstep=$vinc
log off
#
tonyplot -overlay ganfetex03_1.log ganfetex03_2.log ganfetex03_3.log ganfetex03_4.log
ganfet03_5.log -set ganfetex03_2.set
tonyplot ganfetex03_1.log -set ganfetex03_2.set

######## this is for modeling threshold area ############
solve vdrain=0 vgate=-4.2
log outf=vgn42.log
solve name=drain vdrain=0 vfinal=5 vstep=1
log off

solve vdrain=0 vgate=-3.9
log outf=vgn39.log
solve name=drain vdrain=0 vfinal=5 vstep=1
log off

solve vdrain=0 vgate=-3.8
log outf=vgn38.log
solve name=drain vdrain=0 vfinal=5 vstep=1
log off

solve vdrain=0 vgate=-3.6
log outf=vgn36.log
```

```
solve name=drain vdrain=0 vfinal=5 vstep=1
log off

solve vdrain=0 vgate=-3.5
log outf=vgn35.log
solve name=drain vdrain=0 vfinal=5 vstep=1
log off

solve vdrain=0 vgate=-3.4
log outf=vgn34.log
solve name=drain vdrain=0 vfinal=5 vstep=1
log off

solve vdrain=0 vgate=-3.2
log outf=vgn32.log
solve name=drain vdrain=0 vfinal=5 vstep=1
log off

solve vdrain=0 vgate=-3.1
log outf=vgn31.log
solve name=drain vdrain=0 vfinal=5 vstep=1
log off

solve vdrain=0 vgate=-2.9
log outf=vgn3.log
solve name=drain vdrain=0 vfinal=2 vstep=1
log off

solve vdrain=0 vgate=-2.7
log outf=vgn27.log
solve name=drain vdrain=0 vfinal=5 vstep=1
log off
tonyplot vgn42.log -overlay vgn39.log -overlay vgn32.log -overlay vgn36.log -overlay vgn3.log
-overlay vgn31.log -set ganfetex03_2.set
tonyplot vgn3.log -set ganfetex03_2.set
##### Floating gate #######################
solve vdrain=0 vgate=0
log outf=vgnfloating.log
solve name=drain vdrain=0 vfinal=10 vstep=1
save outf=cleandevice.str
tonyplot cleandevice.str

##### DC bias for chem_mod ###############
solve vdrain=0 vgate=-0.12
log outf=vgnchemical.log
solve name=drain vdrain=0 vfinal=10 vstep=1
```

```
save outf=dirtydevice.str
tonyplot dirtydevice.str

### DC bias for MIG ######################
solve vdrain=0 vgate=.105
log outf=vgnafter.log
solve name=drain vdrain=0 vfinal=10 vstep=1
save outf=vgnafterr.str
tonyplot vgnafterr.str


#tonyplot vgnfloating.log -overlay vgnchemical.log  -set ganfetex03_2.set
tonyplot vgnfloating.log -overlay vgnchemical.log  -overlay vgnafter.log -set ganfetex03_2.set

tonyplot cleandevice.str
tonyplot dirtydevice.str
tonyplot vgnafterr.str

quit
```
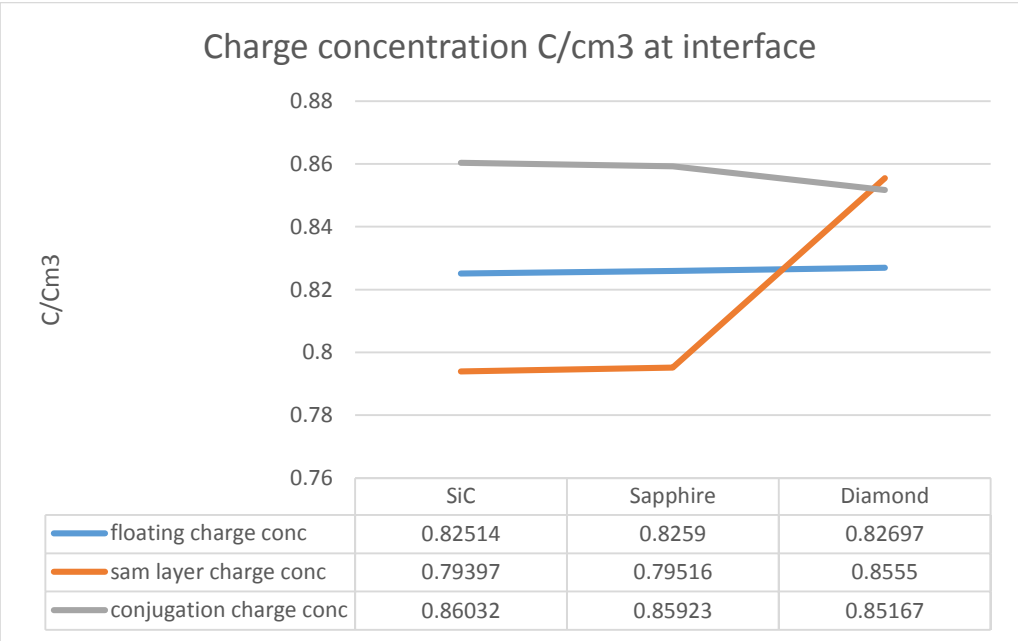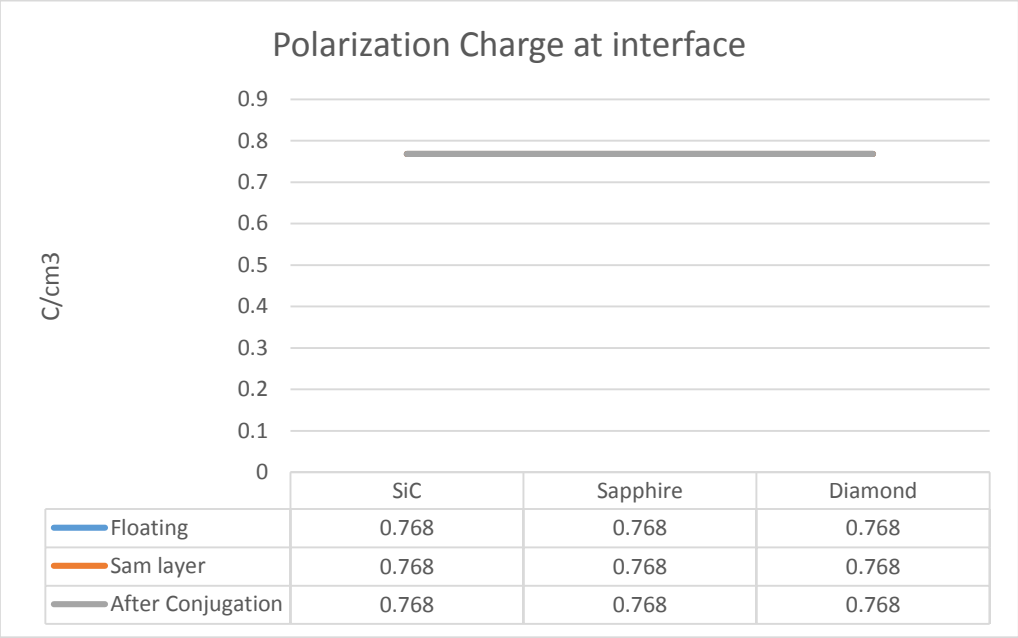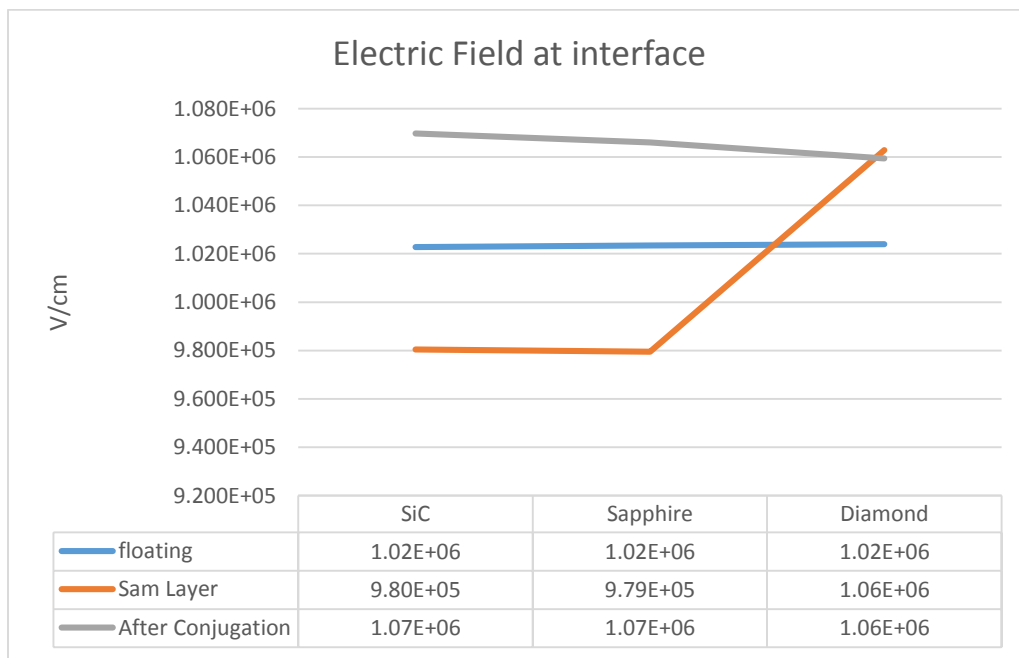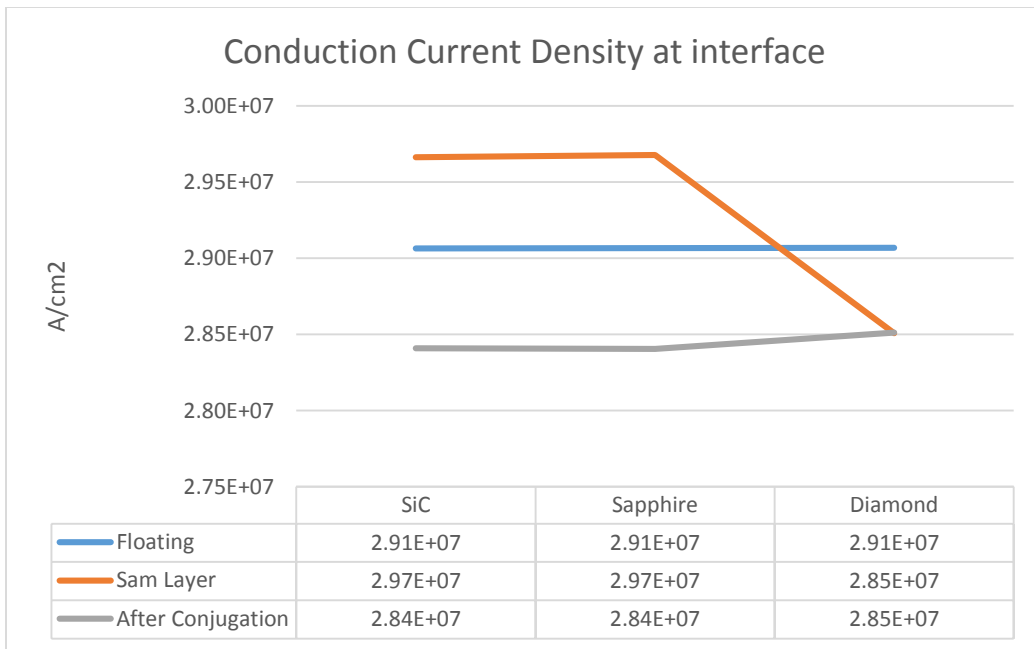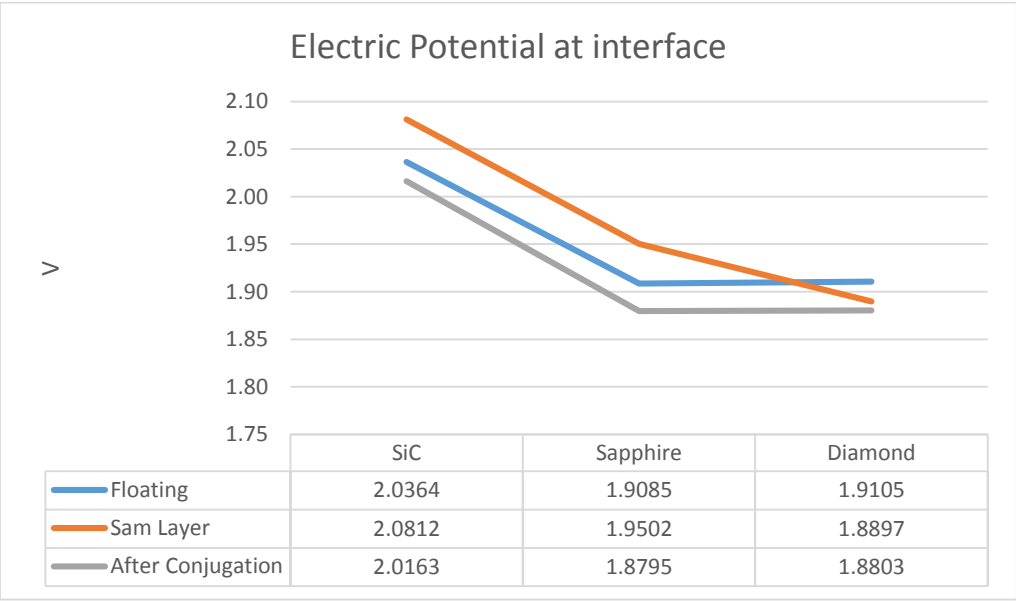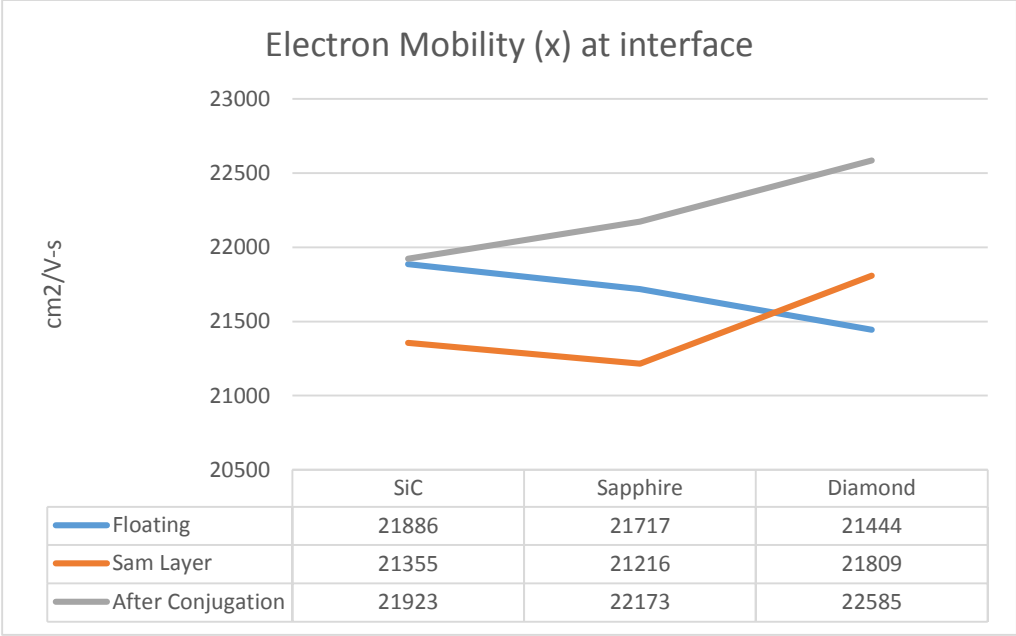
APPENDIX C

GRAPHS CORRESPONDING TO TABLE 5.5

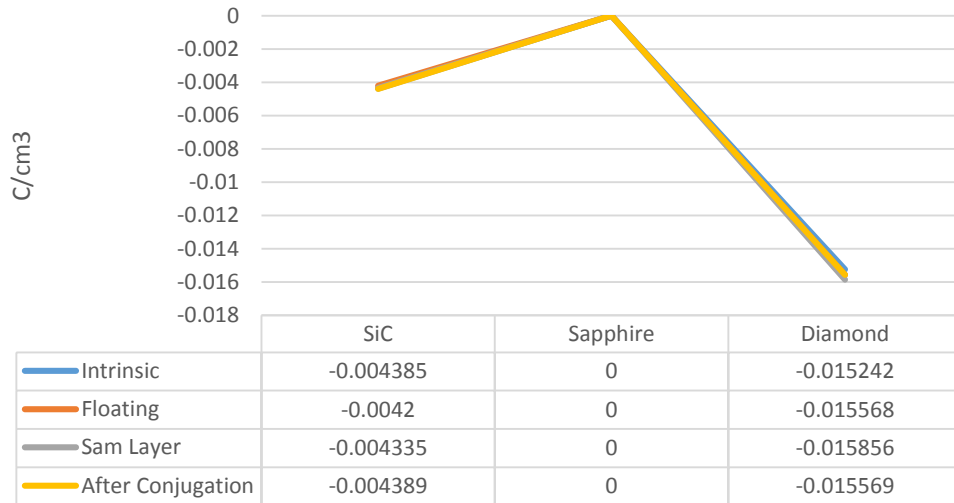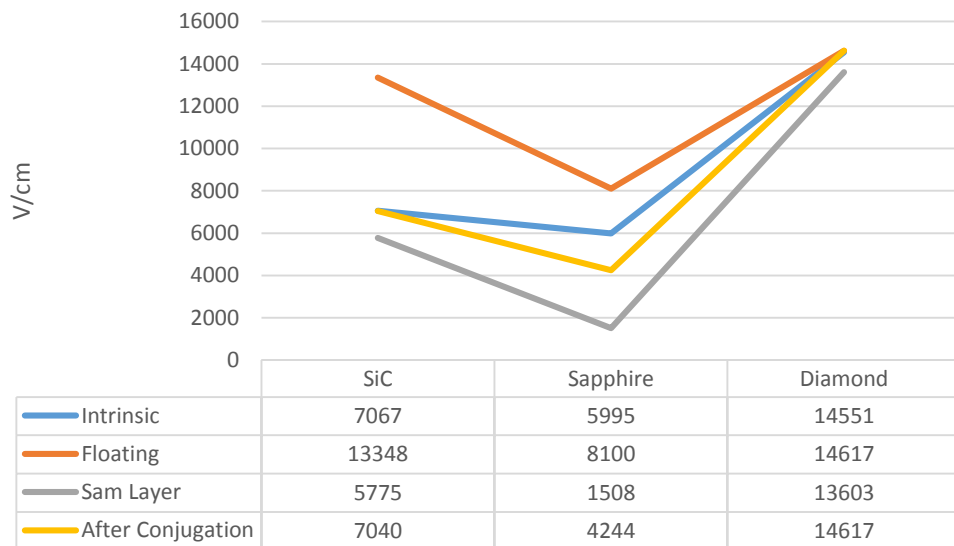## Polarization Charge at interface

	SiC	Sapphire	Diamond
Floating	0.768	0.768	0.768
Sam layer	0.768	0.768	0.768
After Conjugation	0.768	0.768	0.768

Charge concentration C/cm3 at interface

	SiC	Sapphire	Diamond
floating charge conc	0.82514	0.8259	0.82697
sam layer charge conc	0.79397	0.79516	0.8555
conjugation charge conc	0.86032	0.85923	0.85167

Conduction Current Density at interface

	SiC	Sapphire	Diamond
Floating	2.91E+07	2.91E+07	2.91E+07
Sam Layer	2.97E+07	2.97E+07	2.85E+07
After Conjugation	2.84E+07	2.84E+07	2.85E+07

Electric Field at interface

	SiC	Sapphire	Diamond
floating	1.02E+06	1.02E+06	1.02E+06
Sam Layer	9.80E+05	9.79E+05	1.06E+06
After Conjugation	1.07E+06	1.07E+06	1.06E+06

Electron Mobility (x) at interface

	SiC	Sapphire	Diamond
Floating	21886	21717	21444
Sam Layer	21355	21216	21809
After Conjugation	21923	22173	22585

Electric Potential at interface

	SiC	Sapphire	Diamond
Floating	2.0364	1.9085	1.9105
Sam Layer	2.0812	1.9502	1.8897
After Conjugation	2.0163	1.8795	1.8803

APPENDIX D

GRAPHS CORRESPONDING TO TABLE 5.6

Charge concentration at bulk/substrate junction

	SiC	Sapphire	Diamond
Intrinsic	-0.004385	0	-0.015242
Floating	-0.0042	0	-0.015568
Sam Layer	-0.004335	0	-0.015856
After Conjugation	-0.004389	0	-0.015569

Electric Field at bulk/substrate junction

	SiC	Sapphire	Diamond
Intrinsic	7067	5995	14551
Floating	13348	8100	14617
Sam Layer	5775	1508	13603
After Conjugation	7040	4244	14617

Polarization Charge

	SiC	Sapphire	Diamond
Intrinsic	0.0355	0	0.03553
Floating	0.0355	0	0.03553
Sam Layer	0.0355	0	0.03553
After Conjugation	0.0355	0	0.03553
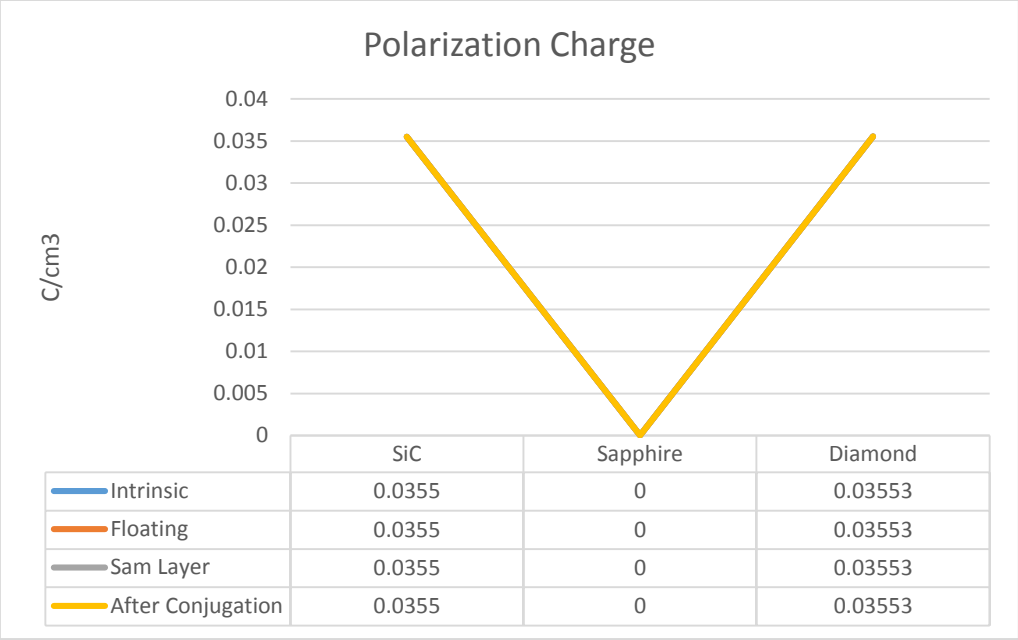
APPENDIX E

DATASHEET FOR HEMT DEVICE USED

CGH40006P
6 W, RF Power GaN HEMT

Cree's CGH40006P is an unmatched, gallium nitride (GaN) high electron mobility transistor (HEMT). The CGH40006P, operating from a 28 volt rail, offers a general purpose, broadband solution to a variety of RF and microwave applications. GaN HEMTs offer high efficiency, high gain and wide bandwidth capabilities making the CGH40006P ideal for linear and compressed amplifier circuits. The transistor is available in a solder-down, pill package.

Package Types: 440109
PN's: CGH40006P

FEATURES

- Up to 6 GHz Operation
- 13 dB Small Signal Gain at 2.0 GHz
- 11 dB Small Signal Gain at 6.0 GHz
- 8 W typical at P_{IN} = 32 dBm
- 65 % Efficiency at P_{IN} = 32 dBm
- 28 V Operation

APPLICATIONS

- 2-Way Private Radio
- Broadband Amplifiers
- Cellular Infrastructure
- Test Instrumentation
- Class A, AB, Linear amplifiers suitable for OFDM, W-CDMA, EDGE, CDMA waveforms

RoHS COMPLIANT

Large Signal Models Available for SiC & GaN

1

137

CREE

Absolute Maximum Ratings (not simultaneous) at 25°C Case Temperature

Parameter	Symbol	Rating	Units	Conditions
Drain-Source Voltage	V_{DSS}	84	Volts	25°C
Gate-to-Source Voltage	V_{GS}	-10, +2	Volts	25°C
Storage Temperature	T_{STG}	-65, +150	°C	
Operating Junction Temperature	T_j	225	°C	
Maximum Forward Gate Current	I_{GMAX}	2.1	mA	25°C
Maximum Drain Current[1]	I_{DMAX}	0.75	A	25°C
Soldering Temperature[2]	T_S	245	°C	
Thermal Resistance, Junction to Case[3]	$R_{\theta JC}$	9.5	°C/W	85°C
Case Operating Temperature[3]	T_C	-40, +150	°C	30 seconds

Note:
[1] Current limit for long term, reliable operation
[2] Refer to the Application Note on soldering at www.cree.com/products/wireless_appnotes.asp
[3] Measured for the CGH40006P at P_{DISS} = 8 W.

Electrical Characteristics (T_C = 25°C)

Characteristics	Symbol	Min.	Typ.	Max.	Units	Conditions
DC Characteristics[1]						
Gate Threshold Voltage	$V_{GS(th)}$	-3.8	-3.0	-2.3	V_{DC}	V_{DS} = 10 V, I_D = 2.1 mA
Gate Quiescent Voltage	$V_{GS(Q)}$	–	-2.7	–	V_{DC}	V_{DS} = 28 V, I_D = 100 mA
Saturated Drain Current	I_{DS}	1.7	2.1	–	A	V_{DS} = 6.0 V, V_{GS} = 2.0 V
Drain-Source Breakdown Voltage	V_{BR}	120	–	–	V_{DC}	V_{GS} = -8 V, I_D = 2.1 mA
RF Characteristics[2] (T_C = 25°C, F_o = 2.0 GHz unless otherwise noted)						
Small Signal Gain	G_{SS}	11.5	13	–	dB	V_{DD} = 28 V, I_{DQ} = 100 mA
Power Output at P_{IN} = 32 dBm	P_{OUT}	7.0	9	–	W	V_{DD} = 28 V, I_{DQ} = 100 mA
Drain Efficiency[3]	η	53	65	–	%	V_{DD} = 28 V, I_{DQ} = 100 mA, P_{IN} = 32 dBm
Output Mismatch Stress	VSWR	–	–	10 : 1	Ψ	No damage at all phase angles, V_{DD} = 28 V, I_{DQ} = 100 mA, P_{IN} = 32 dBm
Dynamic Characteristics						
Input Capacitance	C_{GS}	–	3.0	–	pF	V_{DS} = 28 V, V_{gs} = -8 V, f = 1 MHz
Output Capacitance	C_{DS}	–	1.1	–	pF	V_{DS} = 28 V, V_{gs} = -8 V, f = 1 MHz
Feedback Capacitance	C_{GD}	–	0.1	–	pF	V_{DS} = 28 V, V_{gs} = -8 V, f = 1 MHz

Notes:
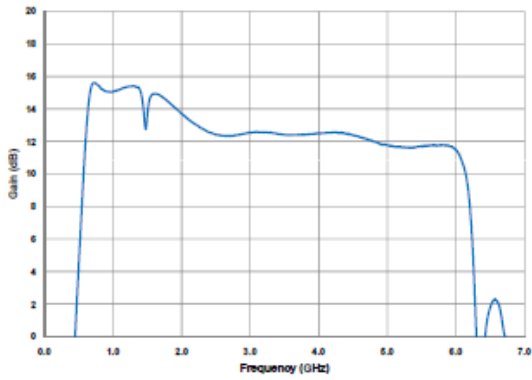[1] Measured on wafer prior to packaging.
[2] Measured in CGH40006P-TB.
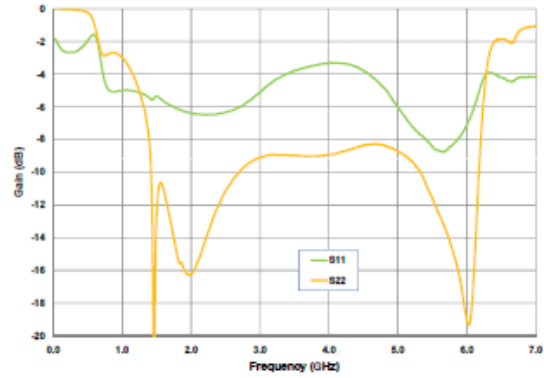[3] Drain Efficiency = P_{OUT} / P_{DC}
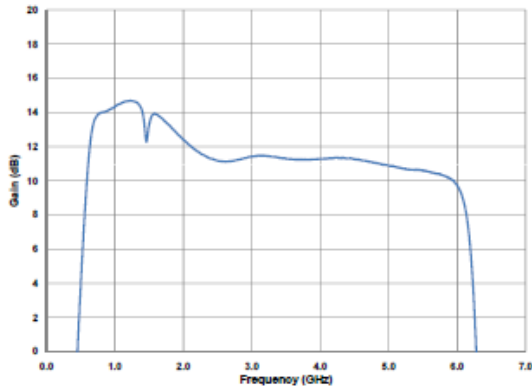
Typical Performance

Small Signal Gain vs Frequency at 28 V of the CGH40006P in the CGH40006P-TB
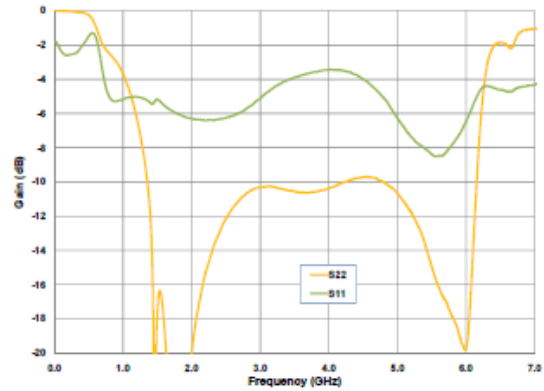

Input & Output Return Losses vs Frequency at 28 V of the CGH40006P in the CGH40006P-TB

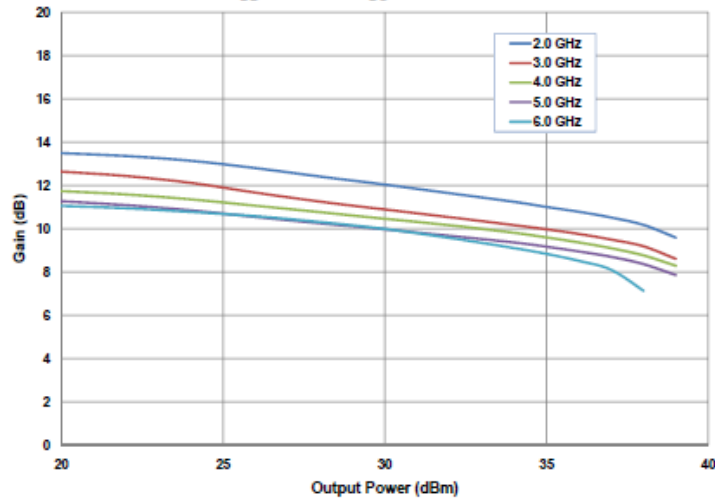### Small Signal Gain vs Frequency at 20 V of the CGH40006P in the CGH40006P-TB

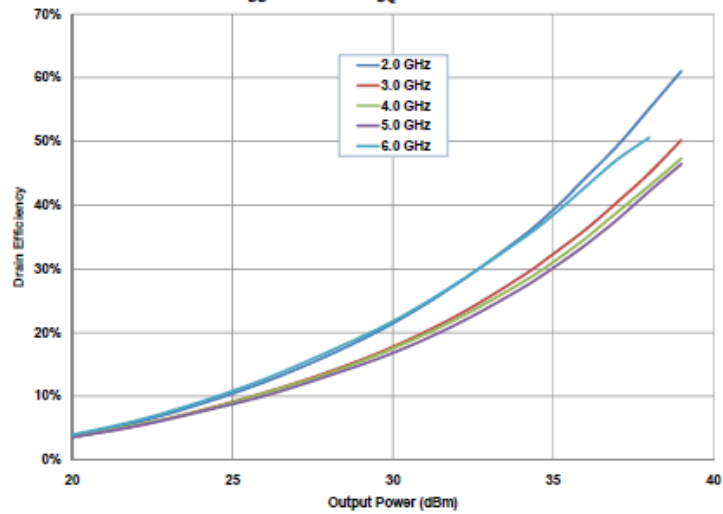### Input & Output Return Losses vs Frequency at 20 V of the CGH40006P in the CGH40006P-TB

3   CGH40006P Rev 2.1

Power Gain vs Output Power as a Function of Frequency of the CGH40006P in the CGH40006P-TB
V_{DD} = 28 V, I_{DO} = 100 mA

Drain Efficiency vs Output Power as a Function of Frequency of the CGH40006P in the CGH40006P-TB
V_{DD} = 28 V, I_{DQ} = 100 mA

Typical Performance

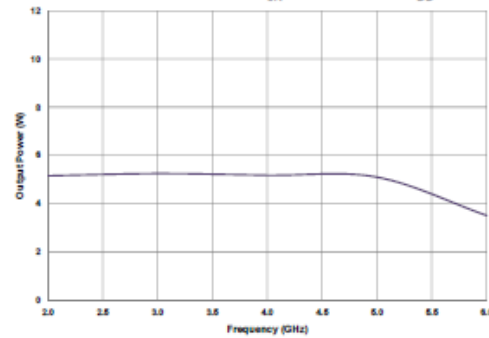**Power Gain vs Frequency of the CGH40006P in the CGH40006P-TB at P_{IN} = 32 dBm, V_{DD} = 28 V**
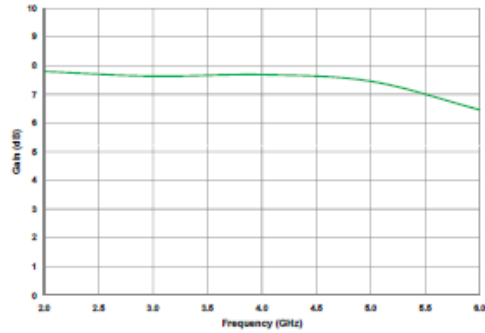
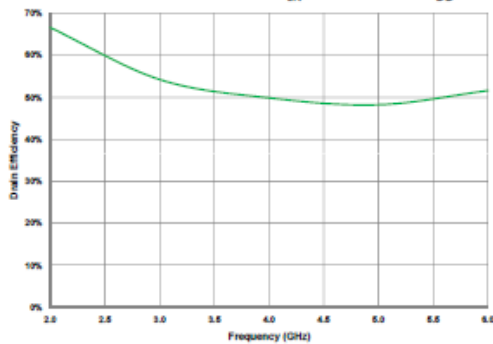**Power Gain vs Frequency of the CGH40006P in the CGH40006P-TB at P_{IN} = 30 dBm, V_{DD} = 20 V**
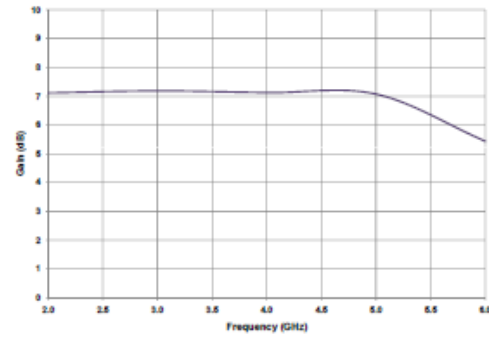
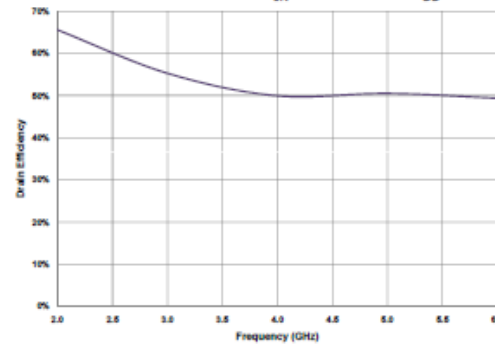**Output Power vs Frequency of the CGH40006P in the CGH40006P-TB at P_{IN} = 32 dBm, V_{DD} = 28 V**
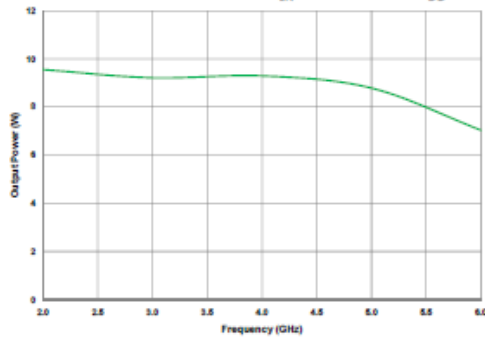
Output Power vs Frequency of the CGH40006P in the CGH40006P-TB at P_{IN} = 30 dBm, V_{DD} = 20 V

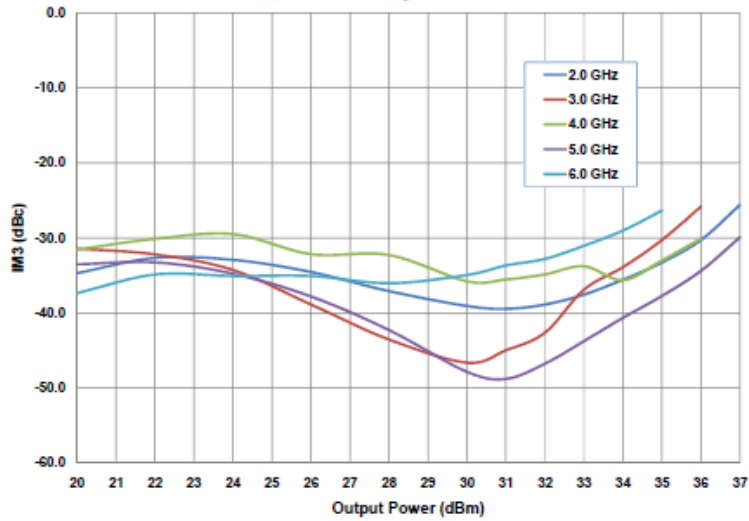**Drain Efficiency vs Frequency of the CGH40006P in the CGH40006P-TB at P_{IN} = 32 dBm, V_{DD} = 28 V**

Drain Efficiency vs Frequency of the CGH40006P in the CGH40006P-TB at P_{IN} = 30 dBm, V_{DD} = 20 V
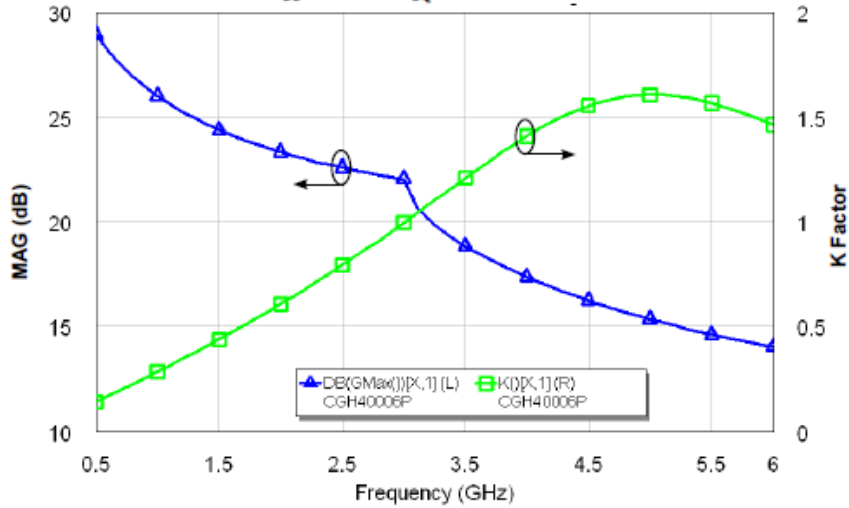
Third Order Intermodulation Distortion vs Average Output Power as a Function of Frequency of the CGH40006P in the CGH40006P-TB
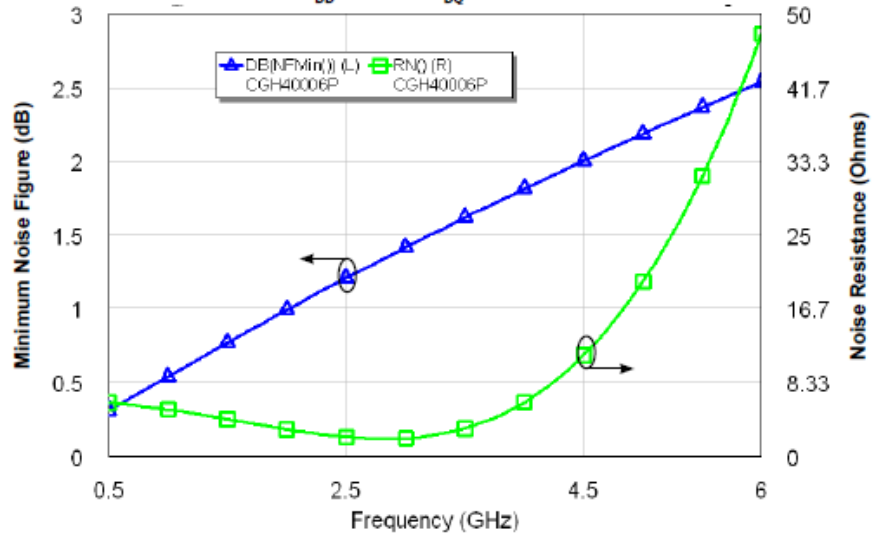$V_{DD} = 28$ V, $I_{DQ} = 60$ mA

Simulated Maximum Available Gain and K Factor of the CGH40006P
$V_{DD} = 28$ V, $I_{DQ} = 100$ mA

Typical Noise Performance

Simulated Minimum Noise Figure and Noise Resistance vs Frequency of the CGH40006P
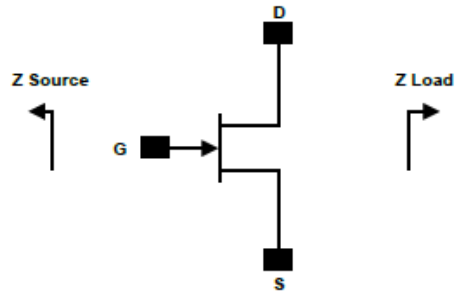V_{DD} = 28 V, I_{DQ} = 100 mA

Electrostatic Discharge (ESD) Classifications

| Parameter	Symbol	Class	Test Methodology
Human Body Model	HBM	1A > 250 V	JEDEC JESD22 A114-D
Charge Device Model	CDM	1 < 200 V	JEDEC JESD22 C101-C

Source and Load Impedances

Frequency (MHz)	Z Source	Z Load
1000	13.78 + j6.9	61.5 + j47.4
2000	4.78 + j1.78	19.4 + j39.9
3000	2.57 - j6.94	12.57 + j23.1
4000	3.54 - j14.86	9.44 + j11.68
5000	4.42 - j25.8	9.78 + j4.85
6000	7.1 - j42.7	9.96 - j4.38

Note 1. V_{DD} = 28V, I_{DQ} = 100mA in the 440109 package.
Note 2. Optimized for power gain, P_{SAT} and PAE.
Note 3. When using this device at low frequency, series resistors should be used to maintain amplifier stability.
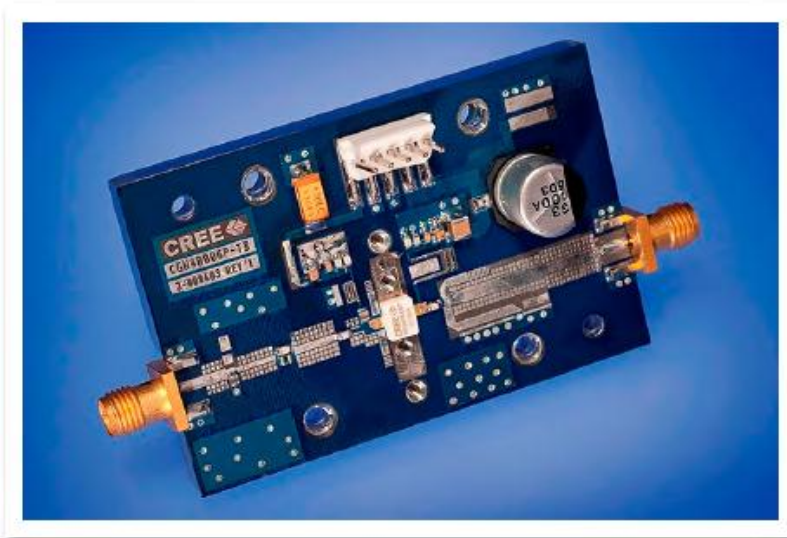
CGH40006P Power Dissipation De-rating Curve
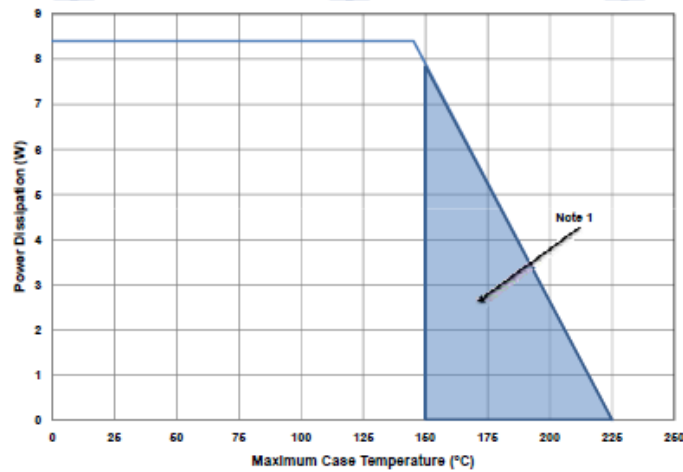
Note 1. Area exceeds Maximum Case Operating Temperature (See Page 2).

CGH40006P-TB Demonstration Amplifier Circuit Bill of Materials

Designator	Description	Qty
R1	RES, AIN, 0505, 470 Ohms (≤5% tolerance)	1
R2	RES, AIN, 0505, 10 Ohms (≤5% tolerance)	1
R3	RES, AIN, 0505, 150 Ohms (≤5% tolerance)	1
C1	CAP, 2.0 pF +/-0.1 pF, 0603, ATC 600S	1
C2	CAP, 4.7 pF +/-0.1 pF, 0603, ATC 600S	1
C10	CAP, 3.6 pF +/-0.1 pF, 0603, ATC 600S	1
C4,C11	CAP, 8.2 pF +/-0.25, 0603, ATC 600S	2
C6,C13	CAP, 470 pF +/-5%, 0603, 100 V	2
C7,C14	CAP, 33000 pF, CER, 100V, X7R, 0805	2
C8	CAP, 10 uf, 16V, SMT, TANTALUM	1
C15	CAP, 1.0 uF +/-10%, CER, 100V, X7R, 1210	1
C16	CAP, 33 uF, 100V, ELECT, FK, SMD	1
J3,J4	CONN, SMA, STR, PANEL, JACK, RECP	2
J1	HEADER RT>PLZ .1CEN LK 5POS	1
-	PCB, RO5880, 20 MIL	1
Q1	CGH40006P	1

CGH40006P-TB Demonstration Amplifier Circuit

CGH40006P-TB Demonstration Amplifier Circuit Schematic
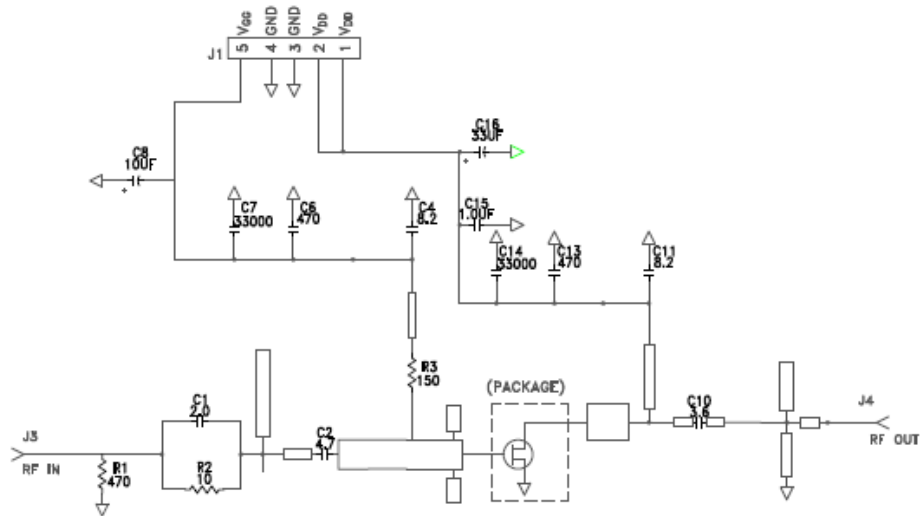
CGH40006P-TB Demonstration Amplifier Circuit Outline

146

Typical Package S-Parameters for CGH40006P
(Small Signal, V_{DS} = 28 V, I_{DQ} = 100 mA, angle in degrees)

Frequency	Mag S11	Ang S11	Mag S21	Ang S21	Mag S12	Ang S12	Mag S22	Ang S22
500 MHz	0.905	-96.56	18.30	120.62	0.023	35.87	0.456	-52.76
600 MHz	0.889	-107.98	16.39	113.31	0.025	29.63	0.429	-58.98
700 MHz	0.877	-117.55	14.76	106.99	0.026	24.39	0.408	-64.31
800 MHz	0.867	-125.66	13.37	101.43	0.027	19.92	0.393	-68.96
900 MHz	0.860	-132.61	12.19	96.46	0.028	16.05	0.381	-73.11
1.0 GHz	0.854	-138.66	11.18	91.94	0.028	12.66	0.374	-76.87
1.1 GHz	0.849	-143.98	10.31	87.79	0.028	9.64	0.368	-80.34
1.2 GHz	0.845	-148.73	9.56	83.92	0.028	6.92	0.366	-83.57
1.3 GHz	0.842	-153.01	8.90	80.29	0.028	4.46	0.365	-86.61
1.4 GHz	0.839	-156.90	8.33	76.84	0.028	2.22	0.365	-89.49
1.5 GHz	0.837	-160.49	7.82	73.56	0.028	0.15	0.367	-92.24
1.6 GHz	0.835	-163.81	7.37	70.40	0.028	-1.75	0.369	-94.88
1.7 GHz	0.833	-166.92	6.96	67.36	0.028	-3.51	0.373	-97.43
1.8 GHz	0.832	-169.85	6.60	64.41	0.028	-5.15	0.376	-99.88
1.9 GHz	0.830	-172.62	6.27	61.54	0.028	-6.67	0.381	-102.27
2.0 GHz	0.829	-175.27	5.98	58.74	0.028	-8.08	0.386	-104.58
2.1 GHz	0.828	-177.81	5.71	56.00	0.028	-9.40	0.391	-106.84
2.2 GHz	0.827	179.75	5.46	53.32	0.027	-10.61	0.396	-109.04
2.3 GHz	0.826	177.38	5.24	50.68	0.027	-11.73	0.401	-111.19
2.4 GHz	0.825	175.07	5.03	48.09	0.027	-12.77	0.407	-113.29
2.5 GHz	0.824	172.82	4.84	45.53	0.027	-13.71	0.412	-115.36
2.6 GHz	0.823	170.61	4.67	43.00	0.026	-14.57	0.418	-117.38
2.7 GHz	0.821	168.44	4.51	40.50	0.026	-15.34	0.423	-119.36
2.8 GHz	0.820	166.30	4.36	38.02	0.026	-16.02	0.428	-121.32
2.9 GHz	0.819	164.18	4.22	35.57	0.026	-16.62	0.434	-123.24
3.0 GHz	0.818	162.08	4.09	33.13	0.026	-17.13	0.439	-125.13
3.2 GHz	0.816	157.91	3.85	28.31	0.025	-17.89	0.449	-128.84
3.4 GHz	0.813	153.76	3.65	23.53	0.025	-18.30	0.458	-132.46
3.6 GHz	0.810	149.58	3.47	18.78	0.025	-18.38	0.467	-136.00
3.8 GHz	0.807	145.35	3.31	14.05	0.024	-18.13	0.474	-139.48
4.0 GHz	0.804	141.05	3.18	9.32	0.024	-17.60	0.481	-142.91
4.2 GHz	0.801	136.66	3.05	4.57	0.024	-16.82	0.488	-146.30
4.4 GHz	0.797	132.15	2.94	-0.20	0.025	-15.89	0.493	-149.67
4.6 GHz	0.793	127.50	2.85	-5.01	0.025	-14.87	0.497	-153.02
4.8 GHz	0.789	122.70	2.76	-9.86	0.026	-13.89	0.500	-156.37
5.0 GHz	0.785	117.72	2.68	-14.79	0.027	-13.04	0.503	-159.74
5.2 GHz	0.780	112.55	2.62	-19.78	0.029	-12.42	0.504	-163.14
5.4 GHz	0.776	107.17	2.55	-24.86	0.030	-12.13	0.505	-166.59
5.6 GHz	0.772	101.58	2.50	-30.03	0.032	-12.22	0.504	-170.10
5.8 GHz	0.768	95.76	2.44	-35.30	0.035	-12.75	0.503	-173.70
6.0 GHz	0.764	89.70	2.40	-40.69	0.037	-13.73	0.501	-177.41

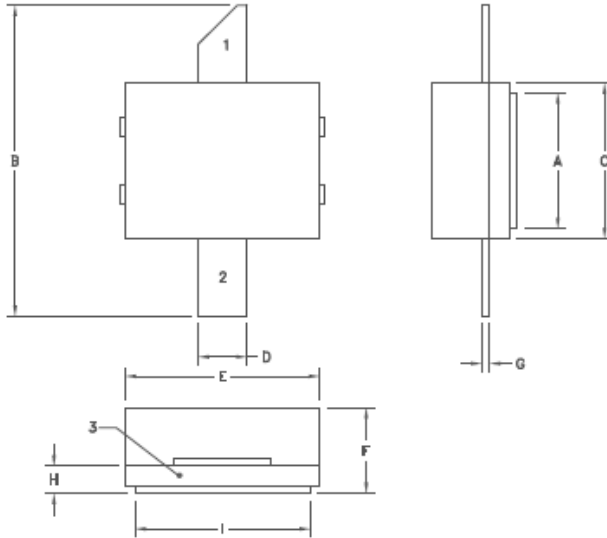Download this s-parameter file in ".s2p" format at http://www.cree.com/products/wireless_s-parameters.asp

Product Dimensions CGH40006P (Package Type — 440109)

NOTES: (UNLESS OTHERWISE SPECIFIED)

1. INTERPRET DRAWING IN ACCORDANCE WITH ANSI Y14.5M—1982 DIMENSIONING AND TOLERANCING.
2. CONTROLLING DIMENSION: INCH.

DIM	INCHES		MILLIMETERS	
	MIN	MAX	MIN	MAX
A	.135	.145	3.43	3.68
B	.315	.325	8.00	8.26
C	.155	.165	3.94	4.19
D	.045	.055	1.14	1.40
E	.195	.205	4.95	5.21
F	.090	.110	2.29	2.79
G	.007	.009	.178	0.23
H	.026	.030	.660	.762
I	.175	.185	4.45	4.70

PIN 1. GATE
PIN 2. DRAIN
PIN 3. SOURCE

CREE

Disclaimer

Specifications are subject to change without notice. Cree, Inc. believes the information contained within this data sheet to be accurate and reliable. However, no responsibility is assumed by Cree for any infringement of patents or other rights of third parties which may result from its use. No license is granted by implication or otherwise under any patent or patent rights of Cree. Cree makes no warranty, representation or guarantee regarding the suitability of its products for any particular purpose. "Typical" parameters are the average values expected by Cree in large quantities and are provided for information purposes only. These values can and do vary in different applications and actual performance can vary over time. All operating parameters should be validated by customer's technical experts for each application. Cree products are not designed, intended or authorized for use as components in applications intended for surgical implant into the body or to support or sustain life, in applications in which the failure of the Cree product could result in personal injury or death or in applications for planning, construction, maintenance or direct operation of a nuclear facility.

For more information, please contact:

Cree, Inc.
4600 Silicon Drive
Durham, North Carolina, USA 27703
www.cree.com/wireless

Sarah Miller
Marketing & Export
Cree, RF Components
1.919.407.5302

Ryan Baker
Marketing
Cree, Wireless Devices
1.919.287.7816

Tom Dekker
Sales Director
Cree, Wireless Devices
1.919.313.5639

BIOGRAPHICAL SKETCH

Hector Trevino II was born in San Diego, California in 1989. He is the son of Hector Trevino, a retired former U.S. marine and border patrol agent, and Ann Patricia Trevino, an educator with Brooks County independent school district. The majority of his life was spent growing up in south Texas with a big interest in technology in video games. Hector received his Bachelor's degree from the University of Texas-Pan American in 2012 and his Master's degree in 2014. He is a member of the Institute of Electrical and Electronics Engineers (IEEE), and has presented research in HESTEC, IEEE Region 5 Conferences, and the ISDRS symposium. His main research interests are solid state device physics with emphasis on theoretical studies in GaN based wide band-gap structures. He maintained a 4.0 average throughout his graduate career and his conducted research includes experimental studies of biosensors to detect Human MIG by using chemically modified AlGaN/GaN based high-electron-mobility-transistors, and two-dimensional modeling of the former to study changes in output characteristics. Upon graduation from the University of Texas – Pan American, Hector is to join Intel in Phoenix, Arizona as a process engineer taking part in the 1272 14nm process.

Permanent address: 7142 Shady Elms San Antonio, TX 78240

Permanent email address: hextop3333@gmail.com